UNIVERSITY *of* TASMANIA

School of Natural Sciences
Discipline of Physics

PROBING INTRACLUSTER GAS WITH FARADAY ROTATION FROM BLACK HOLE JETS

by

Payton E. Rodman, B.Sc.

November 2018

Submitted in partial fulfilment of the requirements for the Degree of

Bachelor of Science with Honours

Supervisor: Dr Stanislav S. Shabala & Dr Ross J. Turner

I declare that this thesis contains no material which has been accepted for a degree or diploma by the University or any other institution, except by way of background information and duly acknowledged in the thesis, and that, to the best of my knowledge and belief, this thesis contains no material previously published or written by another person, except where due acknowledgement is made in the text of the thesis.

Signed: _____
           Payton E. Rodman

Date: _____

This thesis may be made available for loan and limited copying in accordance with the *Copyright Act 1968*

Signed: _____
        Payton E. Rodman

Date: _____

ABSTRACT

This thesis presents an analysis of the effectiveness of Faraday Rotation and its associated measures in helping to constrain the properties of observed AGN radio lobes and their surrounding environment. A study of Faraday Rotation through the Rotation Measure (RM) distribution allows for a line-of-sight computation of both the thermal electron number density (n_e) and magnetic field ($\underline{\boldsymbol{B}}$) distributions in the intracluster medium (ICM), and so the RM, in conjunction with other common radio observables, may be used to infer such parameters as the cluster mass or source orientation with respect to the plane of the sky.

The role of environment on radio lobe properties is first investigated with a sample of 16 Fanaroff-Riley Type II (FR-II) sources, 6 FR-I sources, and one hybrid morphology radio source (HyMoRS) from the Radio Galazy Zoo (RGZ) citizen science project. These radio lobes have total linear sizes exceeding ~ 100 kpc and redshifts of $z < 0.3$. FR-I sources appear to be hosted by more massive galaxies, consistent with previous studies. For the FR-II sample, the degree of asymmetry in radio lobe properties of length and luminosity are compared to asymmetry in the surrounding environment, as quantified through optical galaxy clustering. Radio lobe length is found to be anti-correlated with both galaxy clustering and lobe luminosity for FR-IIs, which is in quantitative agreement with predictions from radio source dynamical models, and suggest that galaxy clustering provides a useful proxy for the ambient gas density distribution encountered by the radio lobes.

These findings are used to inform theoretical models which are constructed for both n_e and $\underline{\boldsymbol{B}}$ within clusters of varying mass and for radio sources of varying orientation, placed at $z < 0.05$ from which the RM distribution was calculated. It is found that an underlying power-law density distribution leads to significant asymmetry in the magnitude of the RM distribution, whilst $\underline{\boldsymbol{B}}$ controls the variance in RM along the projected jet axis. Together these two results show that, for a radio source pointing out at some angle to the plane of the sky, the far lobe will preferentially exhibit greater variance and magnitude in RM, and will consequently show greater depolarisation. This result is in broad agreement with those expected by the Laing-Garrington effect, in which linearly polarised light travelling through a greater path length to the observer is incident upon more of the intervening depolarising, magnetised medium.

These results are characterised further through the inclusion of the dynamical radio source model *Radio AGN in Semi-analytic Environments* (RAiSE), which provided more physically-realistic radio source parameters up to an age of 1 Gyr. These models are combined for those of the density and magnetic field distributions, and the resultant RM distribution is once again calculated alongside observables for the total source length D and total source luminosity L_ν for frequency ν. The possible signatures of the Laing-Garrington effect are characterised by two new observables: the standard deviation of the RM (σ_{RM}), and the change in the variance of the RM (the

heteroscedasticity, H).

A series of random test models are produced and are then matched to the nearest model within the known population based on a χ^2 parameter estimation on L_ν and D, which is then repeated for all of L_ν, D, σ_{RM}, and H. Test sources appear to match more precisely to the nearest known model when the additional RM metrics are included in the χ^2-test. The confidence on the fit around some small tolerance for the source orientation θ is increased by a factor of 1.38×10^4, whilst that of the cluster dark matter halo mass M_{200} is increased by a factor of 6.16 ± 0.07. The source age t_{age} and jet power Q see increases of factors of 1.48 ± 0.10 and 1.01 ± 0.06 respectively. In all cases, the increase in confidence on the match is accompanied by a greater difference between the test and model value of that parameter, although this is expected due to sparse sampling of the parameter spaces within 0.25 dex for Q and M_{200}, and 0.5 dex for t_{age}. Assuming that one of θ or M_{200} is known *a priori* tends to further improve the model's ability to match random test cases to those already known.

Overall, the inclusion of RM metrics improves constraints on radio source and galaxy cluster properties for the models investigated within this thesis, making the Faraday Rotation from black hole jets a promising method by which to measure intracluster gas.

ACKNOWLEDGEMENTS

Firstly, thanks must go to my supervisors, Ross and Stas. From six months stuck on a single equation, to publishing our RGZ paper, and finally to submitting this thesis, you have balanced that arduous contradiction of keeping me on track whilst also periodically allowing me to fail. The physics of black holes may be learnt from papers and textbooks, but the art of failing gracefully can only be learnt by practice. From now on, my only hope is that every mistake I make will be a different one, and I have you both to thank for teaching me the value of that.

Thank you to the more than 11,000 volunteers who took the time to help with the Radio Galaxy Zoo project. Without you, this work would have taken me many more years to complete; it would not have been possible.

Thank you to the many lecturers and teachers I have had over the years, both from St. Brendan-Shaw College and the University of Tasmania. In particular, enormous thanks must go to Mr Ian Cruickshank who first kindled my interest in physics and ultimately lead me to where I am today.

And last, but very certainly not least, a huge thanks to my family who have supported me and encouraged me to keep going at every step in this journey. You've taught me to be stubborn, which may ultimately be the greatest gift I'll ever receive.

The following people and institutions contributed to the publication of work undertaken as part of this thesis:

Payton E. Rodman	University of Tasmania
Ross J. Turner	University of Tasmania
	CSIRO Australia Telescope National Facility
Stanislav S. Shabala	University of Tasmania
Julie K. Banfield	Australian National University
O. Ivy Wong	The University of Western Australia
	ARC Centre of Excellence for All-sky Astrophysics (CAASTRO)
Heinz Andernach	Universidad de Guanajuato
Avery F. Garon	University of Minnesota
Anna D. Kapińska	National Radio Astronomy Observatory (NRAO)
Ray P. Norris	Western Sydney University
Lawrence Rudnick	University of Minnesota

Author details and their roles

Paper 1, Radio Galaxy Zoo: Observational evidence for environment as the cause of radio source asymmetry
Located in Chapter 2
Completed in part for the University of Tasmania's 2015 Dean's Summer Research Program, and supported by a Dean's Summer Research Studentship.

P.R was the primary author, contributed to the analysis and interpretation of the research data, and drafted significant parts of the paper.

R.T. and S.S contributed to the conception and design of the project, the analysis and interpretation of the research data, and drafted significant parts of the paper.

J.K., O.-I.W., and A.F.G. contributed to the conception of the project, to the interpretation of the research data, and to the interpretation of the work by critically revising the paper.

H.A., A.K., R.P., and L.F.R contributed to the interpretation of the work by critically revising the paper.

TABLE OF CONTENTS

LIST OF FIGURES

iv

Chapter 1

Introduction

1.1 Active Galactic Nuclei

At the centre of every galaxy more massive than the Milky Way, obscured behind a torus of hot gas and dust, resides a supermassive black hole (SMBH). The formation of this monolith is thought to be intrinsically tied to the formation of the host galaxy (King, 2003), and its continual presence guides the evolution of its host. Energy and radiation is generated by this central engine through the in-fall of matter from the co-rotating accretion disk, forming an Active Galactic Nuclei (AGN). This energy can exceed the binding energy of the galaxy by a factor of ~ 80, and as such the role of the SMBH in galaxy evolution may be profound if even a small fraction of this energy is distributed through the bulge and disk. The energy from giant radio sources, ranging up to a scale of a few Mpc, may even exceed the gas binding energy of groups and sub-clusters (Fabian, 2012). The release of such prodigious amounts of energy has been implemented into cosmological simulations to reduce formation rates of massive elliptical galaxies, but also to prevent over-cooling and keep star formation rates high in early galaxy halos (e.g. Harrison, 2017; Mathews & Brighenti, 2003; Wagner et al., 2016), and as such, AGN play a pivotal role in our understanding of the universe through cosmic time.

1.1.1 AGN jets

There are many processes, both radially efficient and inefficient, via which energy can be distributed by the active core, but the most visually striking are AGN jets. If material from the accretion disk enters the sphere of influence of the central engine, highly collimated bipolar jets may emerge from the region and extend to kpc and even Mpc scales. As the jets propagate they disrupt and entrain the surrounding medium, either heating or dispelling gas from within the galaxy core. Radio jets continue to expand until they reach regions of pressure/density discontinuity, at which point the jet may be stalled or re-collimated.

These jets may be categorised into two broad groups first described by Fanaroff & Riley (1974): Fanaroff-Riley Class I (FR-I) and Fanaroff-Riley Class II (FR-II) objects (Figure 1.2; Fig-
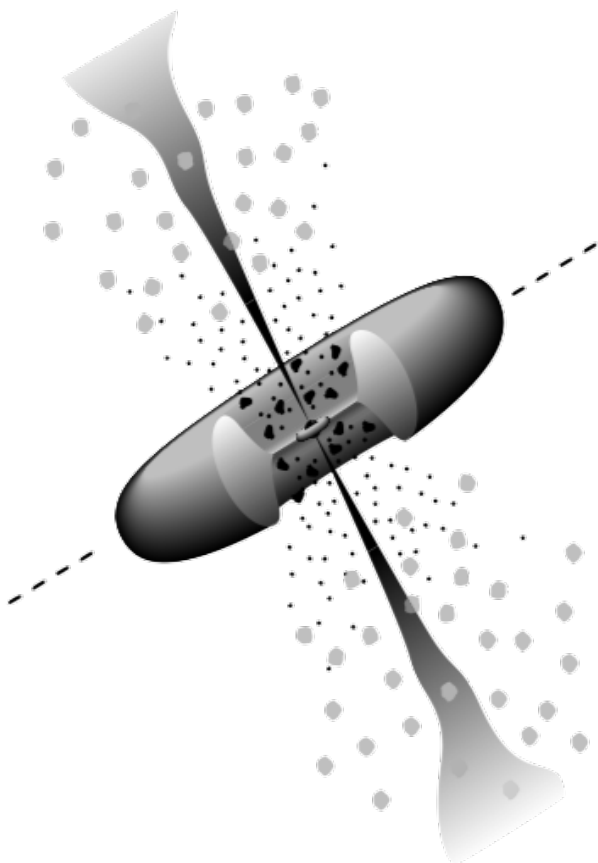
Figure 1.1: AGN showing jets of relativistic particles, along with the dusty torus and associated accretion disk. Figure is adapted from Urry & Padovani (1995), after Collmar (2002).

ure 1.3). There is a corresponding divide in the 178 MHz luminosity, with FR-I sources preferentially below 2×10^{25} W Hz^{-1} sr^{-1} and FR-II sources above (for $H_0 = 50$ km s^{-1} Mpc^{-1}), indicating that the two classes may be physically distinct. Further, the critical power defining the split between the two classes was also found to be correlated with the host galaxy optical magnitude (Krause et al., 2012), further supporting the notion that AGN jet morphology is affected by the properties of the host galaxy. The most apparent way to define the classes, however, is not by approximate divisions in luminosity or power, but rather by the position of the brightest point in the jet relative to the total jet length, e.g. by (Krause et al., 2012):

$$FR = \frac{2x_{\text{bright}}}{x_{\text{size}}} + \frac{1}{2},$$ (1.1)

where x_{size} is the total linear size of the jet (determined by the point at which the radio emission drops below 5% of its maximum value), and x_{bright} is the linear distance from the core to the brightest feature. Values of $0.5 < FR < 1.5$ indicate an FR-I source (edge-darkened), and $1.5 < FR < 2.5$ indicate FR-II (edge-brightened) (Krause et al., 2012).

FR-I jets are visually characterised by narrow jets which "flare" to a bright point before dimming, which may be modelled as a transition from laminar to turbulent flow (Wang et al., 2009). This flare point is shown to coincide with a sharp increase in the ambient temperature of the intracluster gas and with a flattening of the cluster density profile (Krause et al., 2012), strongly suggesting that the FR morphology is influenced by properties intrinsic to both the jets and the cluster environment. The length of a radio jet is a key parameter when determining its other properties; this poses a problem for FR-I jets as their length varies significantly depending on the frequency being observed and the sensitivity of the observations. FR-II jets do not suffer the same issue.

FR-II jets terminate in one or more hotspots up to $\sim$ 1Mpc away from the core; from this point, there is a back-flow of shocked plasma, forming radio lobes which extend back towards the AGN (Krause et al., 2012). As FR-II sources are more powerful and more readily analysed over a range of frequencies, much more is known about the dynamics of these jets.

Analytic and numerical models of jet propagation and evolution suggest that there may be two key length scales in determining FR morphology: an inner and outer length denoted by L_1 and L_2 respectively. These are inspired by *self-similarity* models of FR-II radio sources, "self-similarity" meaning that large FR-II sources can be considered as scaled-up versions of small FR-II sources, and hence the models produced will apply over a large range of physical scales (Falle, 1991; Kaiser & Alexander, 1997).

The outer length L_2 is given by (Komissarov & Falle, 1998; Krause et al., 2012):

$$L_2 = \left(\frac{Q_0}{\rho_x c_x^3}\right)^{1/2}$$ (1.2)

$$= 324 \text{ kpc} \left(\frac{Q_0}{10^{39} \text{ W}}\right)^{1/2} \left(\frac{\rho_x}{10^{-23} \text{ kg m}^{-3}}\right)^{-1/2} \left(\frac{c_x}{1000 \text{ km s}^{-1}}\right)^{-3/2},$$ (1.3)

for jet kinetic power Q_0, external density ρ_x, and external sound speed c_x. At this length the radio jet comes into pressure equilibrium with the ambient environment, being over-pressured for $L < L_2$ (Krause et al., 2012) and hence self-similar.
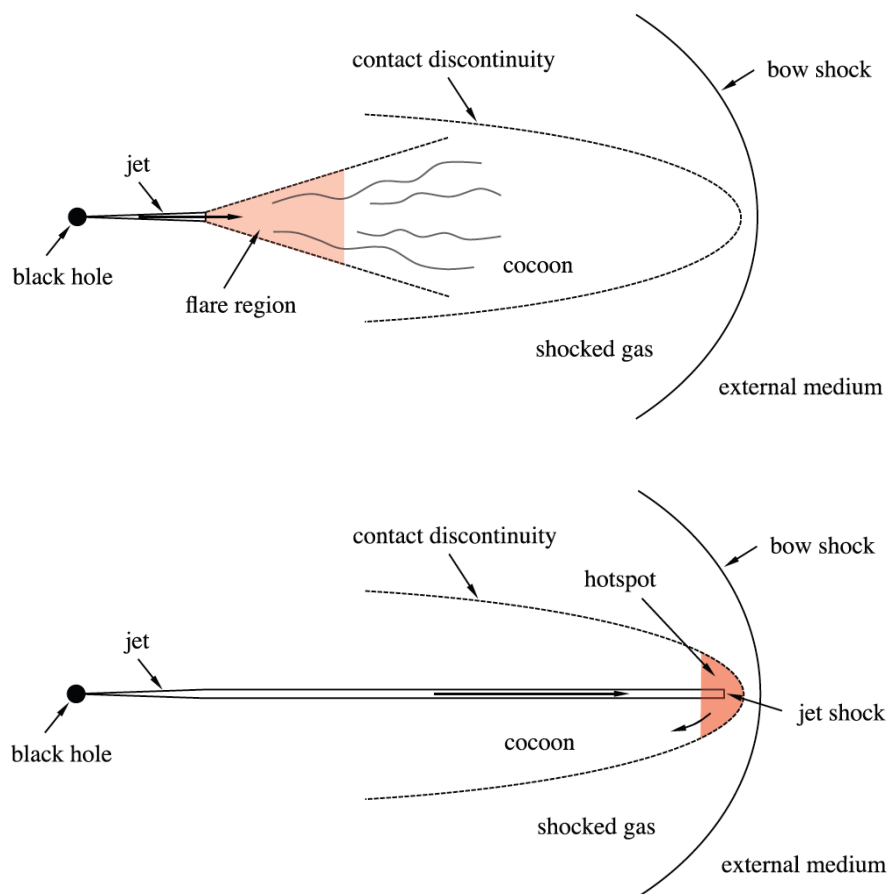
Figure 1.2: Single-sided schematics of Fanaroff-Riley type I (*top*) and type II (*bottom*) jets/cocoons. Adapted from Turner & Shabala (2015).
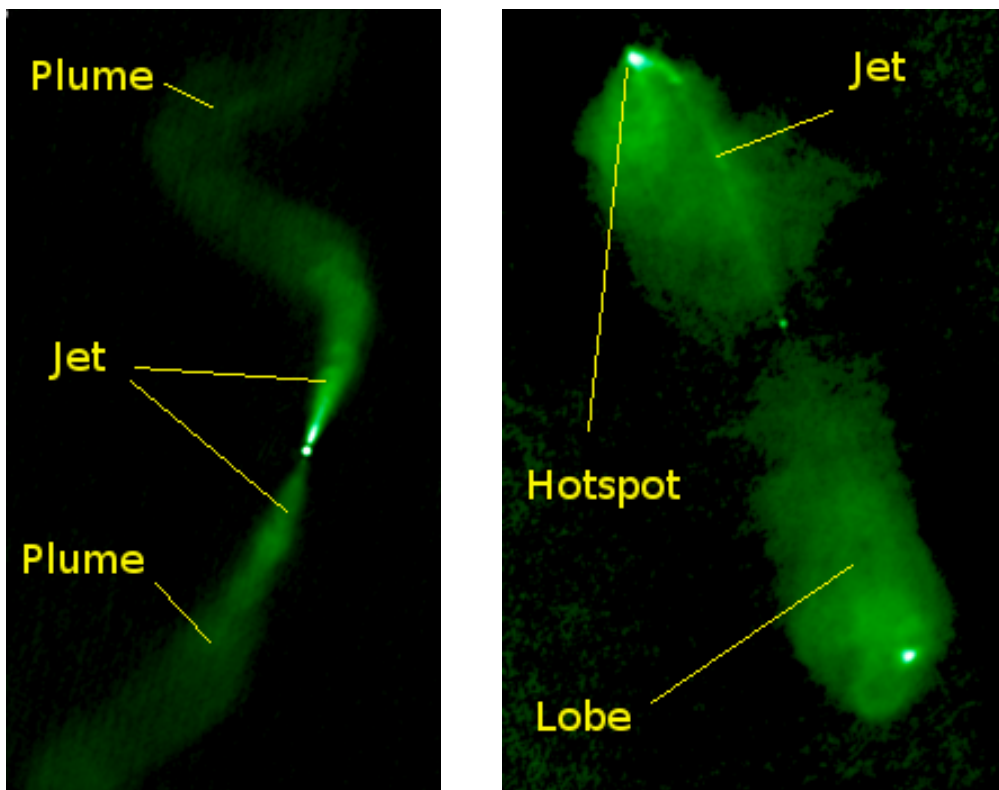
Figure 1.3: Example of Fanaroff-Riley type I (*left*; 3C31) and type II (*right*; 3C98) jets/cocoons, with features labelled. Images from M. Hardcastle.

The inner scale L_1 corresponds roughly to the point at which the jet density and environment density are comparable (Alexander, 2006):

$$L_1 = 2\sqrt{2} \left(\frac{Q_0}{\rho_x v_j^3} \right)^{1/2} \tag{1.4}$$

$$= 56 \text{ kpc } \left(\frac{Q_0}{10^{39} \text{ W}} \right)^{1/2} \left(\frac{\rho_x}{10^{-22} \text{ kg m}^{-3}} \right)^{-1/2} \left(\frac{v_j}{c} \right)^{-3/2}. \tag{1.5}$$

What happens at L_1 may determine the final morphology of the radio jet. If the jet is over-dense with respect to the surrounding environment and travelling supersonically at or before L_1, then a shock will be produced. Much of the jet energy is then deposited in this shock front, leading to minimal lobe production and the appearance of an FR-I. If, however, the jet proceeds to a length $L_1 \ll L \ll L_2$, then it is under-pressured with respect to the environment and becomes re-collimated slightly after L_1, subsequently entering a phase of self-similar expansion. This produces an FR-II jet and lobe (Alexander, 2006; Krause et al., 2012).

Beyond their initial production and throughout their evolution, AGN jets provide us with another clue to their evolution: they are often asymmetric. Differences can be seen in lobe lengths and luminosities for a given radio source, and in extreme cases, some sources display jets of opposing morphology (Gopal-Krishna & Wiita 2000; e.g. Kapińska et al. 2017). Given that the bipolar jets share a common engine, have the same age, and are of similar power, this is evidence that the difference may arise in the surrounding environment. The precise balance of nature (jet production) versus nurture (environment interaction) in this debate is not yet known.

1.1.2 Nature: Jet-host interactions

Direct observations of the central engine are not yet possible due to the obscuring torus which surrounds it, and hence the production mechanism responsible for the creation of AGN jets is not known with certainty. It is thought that magnetic field lines threading regions of a rotating black hole (Blandford & Znajek, 1977; Punsly & Coroniti, 1990) or thin accretion disk (Lovelace, 1976; Blandford & Payne, 1982) may act as an electric dynamo, leading to the acceleration of material perpendicular to the disk in the form of jets.

The precise composition of these jets is also uncertain. This question is significant as the nature of the material – "regular matter" (electrons and protons), pair plasma (electrons and positrons), or some mixture of the two – and the mechanism of production are related (e.g. Blandford & Levinson, 1995). The evidence obtained thus far has been inconsistent, and a consensus has not been reached. Whilst observations of some highly luminous sources suggest an electron-positron plasma (e.g. Hirotani et al., 2000), other sources would require the presence of protons in order to produce their spectral energy distribution (e.g. Mehta et al., 2009).

However, regardless of their precise composition or production, the jet nature is intrinsically linked to the properties of the host galaxy and central black hole. In lieu of direct observations of the accretion disc, large-scale properties of the central BH and host galaxy can be used to probe the nature of radio jets.

The mass of the central BH is itself related strongly to properties of the host galaxy through the $M_{\mathrm{BH}} - \sigma$ relation; σ is the velocity dispersion of stars within the galactic bulge, the densest region of the galaxy (Martín-Navarro & Mezcua 2018; see Kormendy & Ho 2013 for a review). This relation can be approximated by (Tremaine et al., 2002):

$$\frac{\log M_{\mathrm{BH}}}{M_{\odot}} = \alpha + \beta \log \left(\frac{\sigma}{200 \mathrm{\ km\ s}^{-1} \mathrm{\ Mpc}^{-1}} \right) \tag{1.6}$$

with $\alpha = 8.13 \pm 0.06$ and $\beta = 4.02 \pm 0.32$ (Allen et al., 2006).

It is not yet clear whether this relation is primarily caused by jet activity or whether the presence of radio jets is merely one part of the puzzle alongside merger activity and other processes in galaxy evolution (Fabian, 2012). However, even the initial discovery of the relation by Gebhardt et al. (2000) and Ferrarese & Merritt (2000) displayed a remarkably small scatter: 0.30 dex over nearly 3 orders of magnitude in M_{BH}, all of which could be reasonably attributed to instrument noise. Such a fundamental relationship between the SMBH and host galaxy suggests that BH growth and evolution of the bulge are closely tied (Kormendy & Ho, 2013). Growth of the BH will occur by merger activity and by accretion of bulge material.

As the youngest virialised structures in the Universe, galaxy clusters suffer ongoing mergers (Section 1.2). Around 50% of the local cluster population show evidence of recent or current mergers, and examples of "relaxed" clusters are notoriously difficult to find (Mathiesen & Evrard, 2001). Cluster mergers are the most energetic events in the current epoch, releasing $\sim 10^{64}$ erg s^{-1} of gravitational binding energy, and so are prime candidates for triggering gas accretion (Carilli & Taylor, 2002). However, evidence of these major mergers triggering AGN activity is weak for most redshifts, and the outcome of such merger events is likely to be dependent on the gas content of the merging galaxies, and whether the resultant galaxy core is scoured by the new central BH (Fabian, 2012). Modelling galaxy mergers is difficult as a result, and they are often left out of simulations of AGN feedback or otherwise greatly simplified, and so the true impact of major mergers is not yet clear.

Another mechanism for BH growth is the accretion of gas from the region around the BH. Surrounding the central engine, there is a core radius within which the gravitational potential of the BH dominates over the thermal energy of the gas and dust, and hence gas within this region will preferentially move towards and accrete onto the BH. This is the Bondi radius, defined for spherically symmetric accretion as (Bondi, 1952):

$$r_{\mathrm{B}} = \frac{2GM_{\mathrm{BH}}}{c_s^2}, \tag{1.7}$$

where $G = 6.67 \times 10^{-11}$ m^3 kg^{-1} s^{-2} is the gravitational constant, M_{BH} is the mass of the black hole, and $c_s = \sqrt{\gamma_1 \frac{k_{\mathrm{B}} T}{\mu m_{\mathrm{p}}}}$ is the adiabatic sound speed for gas temperature T, Boltzmann constant $k_{\mathrm{B}} = 1.381 \times 10^{-23}$ m^2 kg s^{-2} K^{-1}, mean atomic weight $\mu = 0.62$, proton mass m_{p}, and adiabatic index $\gamma_1 = 5/3$ (Allen et al., 2006). This may be expressed in physical units as (Russell et al., 2015):

$$\frac{r_{\mathrm{B}}}{\mathrm{kpc}} = 0.031 \left(\frac{k_{\mathrm{B}} T}{\mathrm{keV}} \right)^{-1} \left(\frac{M_{\mathrm{BH}}}{10^9 M_{\odot}} \right). \tag{1.8}$$

In the case of M87, with an upper estimate of the black hole mass of $M_{\mathrm{BH}} = (6.6\pm0.4)\times10^9\,\mathrm{M}_\odot$ and inner accretion disk temperature of $k_{\mathrm{B}}T = 0.91^{+0.08}_{-0.11}$ keV, this gives a Bondi radius of 0.22 kpc.

Within the Bondi radius, matter will accrete at a rate (Bondi, 1952):

$$\dot{M}_{\mathrm{Bondi}} = 4\pi\lambda(GM_{\mathrm{BH}})^2 c_s^{-3}\rho = \pi\lambda c_s\rho r_{\mathrm{Bondi}}^2, \tag{1.9}$$

where λ is a numerical constant which varies depending on γ_1. For $\gamma_1 = 5/3$ above, $\lambda = 0.25$ (Bondi, 1952; Allen et al., 2006).

Bondi accretion models work well within the $r < r_{\mathrm{Bondi}}$ regime, but for larger radii become less accurate. Inhomogeneities in the temperature, pressure, density, or any facet of the dynamical state of the accreting material would violate the "spherical symmetry" requirement of the Bondi equations, and there is evidence that such deviations do exist.

Accretion onto the BH can generate extreme amounts of energy, a small fraction of which could have significant effects on the host galaxy. This can be seen by comparing the energy released from accretion to the binding energy of the host.

The energy released by accretion and subsequent growth of the BH can be modelled simply as (Fabian, 2012):

$$E_{\mathrm{Bondi}} = \eta M_{\mathrm{BH}}c^2, \tag{1.10}$$

where $\eta \sim 0.1$ is the radiative efficiency of the accretion process, $M_{\mathrm{BH}} \approx 1.4 \times 10^{-3}M_{\mathrm{bulge}}$ for a bulge mass of $M_{\mathrm{bulge}} \sim 5 \times 10^{10}\,\mathrm{M}_\odot$ (Häring & Rix, 2004), and c is the speed of light.

The binding mass of the galaxy, on the other hand, may be expressed as (Fabian, 2012):

$$E_{\mathrm{gal}} = M_{\mathrm{gal}}\sigma^2, \tag{1.11}$$

for galaxy bulge mass M_{gal} and stellar velocity dispersion σ.

Comparing E_{Bondi} and E_{gal} for a typical upper limit of $\sigma = 400$ km s^{-1} (Fabian, 2012):

$$E_{\mathrm{Bondi}} > 80E_{\mathrm{gal}}. \tag{1.12}$$

This is a tremendous amount of energy, of which only a small part would be needed to significantly alter the galaxy's evolution. However, not all of this energy is converted into kinetic jet power, and much may be converted into relatively inefficient forms such as sound waves. That which is converted into polar jets will be ejected preferentially perpendicular to the galaxy disc, minimising its potential impact on the outer galaxy. There is good reason to expect some fraction of the accretion energy to be expelled as radio jets, namely that the observed luminosities of AGN within elliptical host galaxies are typically several orders of magnitude lower than would be predicted by Bondi accretion alone (Allen et al., 2006). This is likely due to the low efficiency with which energy is transferred to the surrounding gas as only ~ 1 photon out of 10^3 emitted is scattered by an electron within the galaxy, resulting in $\lesssim 0.1$ per cent of the luminous energy being absorbed (Cattaneo & Best, 2009). As a result, the effects of mechanical heating can far outweigh that of radiative heating even though the bulk of the jet energy may be deposited beyond the galaxy halo, and it is important to quantify the expected kinetic power of the radio jets and the way they interact with the host galaxy.

1.1.3   Nurture: Jet-environment interactions

The evolution of AGN is intrinsically tied to the nature of the surrounding material, both in terms of fuelling and energetic coupling. The generation and evolution of radio jets will directly affect the ambient medium they expand into, an effect which may then cascade through the bulge until it impedes jet production.

Lakhchaura et al. (2018) propose a cold gas cycle in the core of a galaxy which may explain the thermal structure of the X-ray atmosphere within elliptical galaxies. Starting from an initial high entropy state - perhaps the result of recent merger or AGN activity - the warm gas in the core of the galaxy begins to cool, leading to instabilities in the gas and the creation of cold gas filaments or clumps. This filamentary gas accretes onto the central engine at a higher rate, increasing the power of the jet and radiative wind produced by the AGN. As jets propagate through the galactic bulge, the surrounding gas is disturbed further, fuelling greater accretion. Eventually the jet power is such that the surroundings become heated, shocked, or turbulent (Fabian, 2012), preventing further filamentation and possibly destroying any pre-existing cold clumps. Radiative processes such as winds will also disrupt the state of nearby gas. This starves the AGN of its fuel source, ceasing the production of jets and returning the galaxy core to its initial high entropy state. Altogether these processes are termed *feedback*, which, given the tremendous amount of energy coupled to AGN, could influence the evolution of the host galaxy on large scales.

AGN feedback processes may reduce galactic star formation rates (SFR) on scales of the interstellar medium (ISM) as the surrounding gas becomes disrupted or removed, although compression of this gas is also possible and would produce bursts in the SFR and increased SFR efficiencies (Pellegrini et al., 2018; Cielo et al., 2018; Nyland et al., 2018). Cosmological simulations provide further evidence with their requirement of AGN feedback in order produce a recognisable galaxy population at $z = 0$ (Kaviraj et al., 2017; Harrison et al., 2018; Nyland et al., 2018; Kormendy & Ho, 2013; Heckman & Best, 2014). Without the inclusion of AGN feedback, cold gas filaments and cooling flows are generated too readily during an early stage in galaxy evolution (Fabian, 1994): at or before 1 Gyr (Bambic et al., 2018).

Cooling flows are seen as a sharp increase in the X-ray surface brightness distribution at the core, which indicates a shorter cooling time as (Fabian, 1994):

$$t_{\text{cool}} \propto \frac{T^{\alpha}}{n_{\text{e}}}, \tag{1.13}$$

for $-1/2 \lesssim \alpha \lesssim 1/2$ and where n_{e} is the thermal electron density. If the time required for the gas to cool is less than the age of the cluster (say, $t_a \sim 1/H_0$), then the gas will cool. If the cooling time is also greater than the gravitational free-fall time then the gas may be in a quasi-hydrostatic equilibrium. At the radius r_{cool} where $t_{\text{cool}} = t_a$, the gas pressure is a function of the overlying gas weight. For the overlying gas beyond t_a, cooling is not important. For $r < r_{\text{cool}}$, the gas cools, meaning that the density must rise in order to maintain the pressure equilibrium at r_{cool}. If there is no source of new material within r_{cool}, then a flow of material from outside of the region must be established. This is known as the *cooling flow* (Fabian, 1994), which may deposit tens, hundreds, or even thousands of solar masses of material per year into the core (Fabian, 2012). Direct observations of this flow are not expected to occur as the gas flows at

subsonic velocities throughout most of the volume. Clusters which contain cooling flows are more dynamically relaxed than their non-cooling flow counterparts, and show more evidence of recent mergers (Carilli & Taylor, 2002). Whether or not $t_a \sim 1/H_0$ is an appropriate choice or not is not clear; in general, this requirement is satisfied by $\sim 70 - 80\%$ of clusters, and reducing t_a by a factor of two is not shown to have a significant effect on the fraction of clusters which are predicted to contain cooling flows (Fabian, 1994).

Models of this cooling flow over-predict SFR and the number of bright, blue galaxies (e.g Mathews & Brighenti, 2003); in order to bring predictions in-line with current observations, some amount of heating is required to offset cooling flows and prevent overzealous accretion and growth of the central black hole. This heating can be neatly supplied by AGN feedback in simulations as it is highly efficient and self-regulatory (Nyland et al., 2018; McNamara & Nulsen, 2007), although jet processes in particular are known to be inefficient when compared to radiative winds as the former contains only a few percent of the total energy injected by the AGN (Bourne & Sijacki, 2017). AGN feedback must also act regularly throughout the lifetime of the cluster, otherwise the gas content of the galaxy bulge will be replenished with that of either the surrounding cluster or of local stellar mass loss (Fabian, 2012).

X-ray cavities permeating out into the intracluster medium (ICM) are observed in $\sim 95\%$ of deep Chandra X-ray images of cool core clusters (Figure 1.4) and often coincide with a FR-I type source (Fabian, 2012); these are observational evidence of this heating in action. As they overlap with radio sources, the X-ray cavities may be used as a sort of "calorimeter": calculating the energy required to inflate the cavities gives a robust estimate of the energy contained within the jet. Once the Bondi accretion rate and jet power is known, the efficiency of the conversion between E_{Bondi} and E_{jet} can additionally be estimated (Allen et al., 2006).

First, the energy required to inflate the X-ray cavities is taken to be the sum of the internal energy of that cavity plus the work done on that cavity (Allen et al., 2006):

$$E = \frac{1}{\gamma_2 - 1}PV + PV \tag{1.14}$$

$$= \frac{\gamma_2}{\gamma_2 - 1}PV, \tag{1.15}$$

for thermal pressure P of the surrounding X-ray gas (estimated from observed temperature and density profiles), cavity volume V, and mean adiabatic index $\gamma_2 = 4/3$ for relativistic plasma. This leads to the cavity energy $E = 4PV$ (Allen et al., 2006) which correlates well with the cooling and radiative losses of the cluster (Bambic et al., 2018).

These cavities are surprisingly stable and long-lived. Provided that either magnetic draping or viscosity dampens out perturbations, the X-ray bubbles will be resistant to both Rayleigh-Taylor and Kelvin-Helmholtz instabilities and can propagate outwards until they are too faint to be detected (Fabian, 2012). However, the inclusion of magnetic fields often complicates more than it explains due to the historically intractable nature of hot, magnetised plasmas. In order to probe jet-environments interactions on these scales, the strength and topology of magnetic fields within jets, galaxies, and larger groups/clusters must first be studied.

The precise details of how AGN jets in particular affect galaxy evolution are not well-understood at a fundamental level. Whilst the likely mechanisms are known (heat, shock fronts, and/or tur-
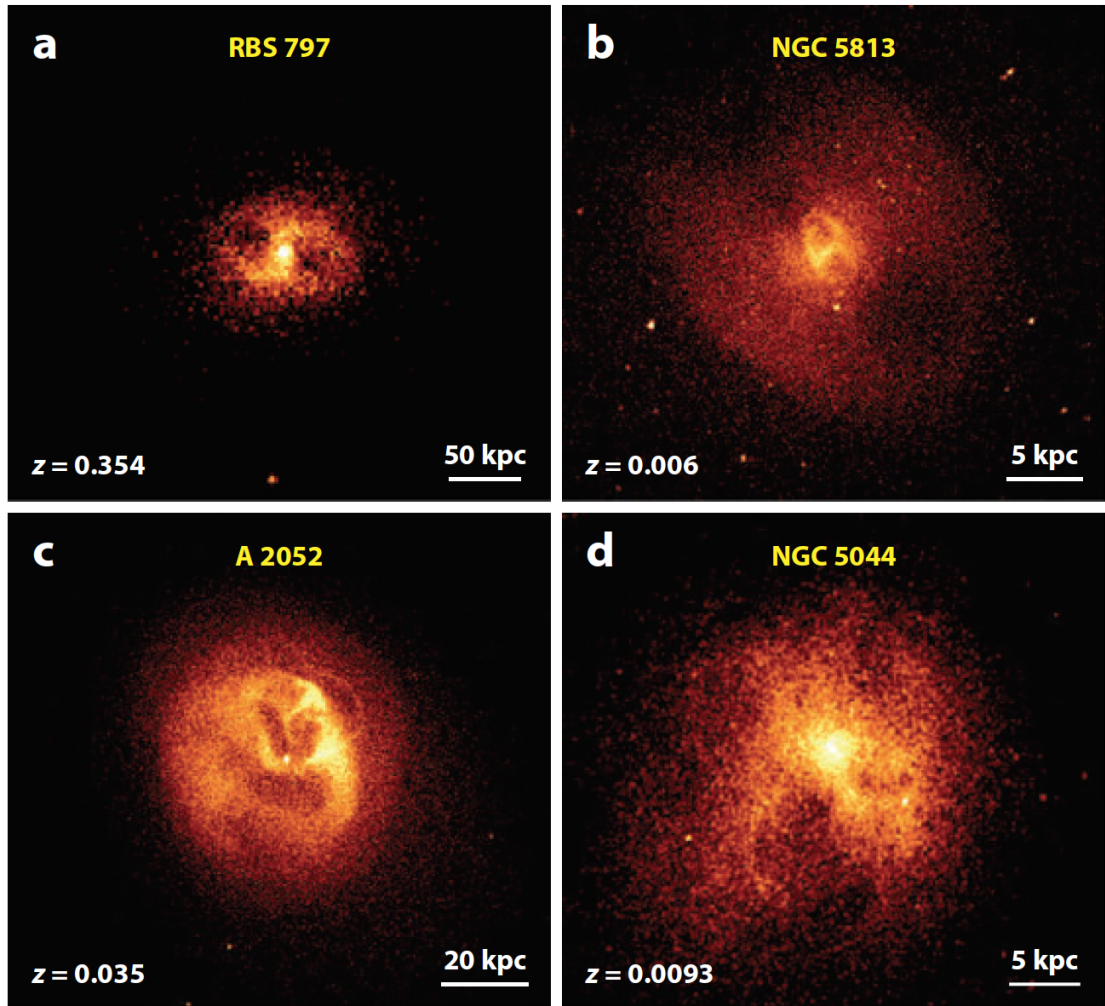
Figure 1.4: *Chandra* observations of X-ray cavities or "bubbles" in (*a*) RBS797 at $z = -.354$, (*b*) NGC 5813 at $z = 0.006$, (*c*) A 2052 at $z = 0.035$, and (*d*) NGC 5044 at $z = 0.0093$. From Fabian 2012 and references therein.

bulence), the conditions under which any particular mechanism will dominate and to what extent it will affect the host galaxy (positive vs negative feedback) are not known (Nyland et al., 2018). There are difficulties in reconciling the extreme scales over which AGN jets occur. Inflows (accretion) will occur at the Schwarzschild radius of the central engine, whilst outflows (jets) may reach as far as hundreds or thousands of kpc. This represents a physical scale of over 10 orders of magnitude, and given the complex nature of filamentary or clumpy gas, the computational requirements for accurate, high resolution 3D simulations are staggering (Fabian, 2012). This is exacerbated by a lack of precise measurements on the surrounding environment. In particular, there are observational difficulties concerning faint X-ray cavities; this inherently biases environmental data to those galaxy clusters which are nearer and/or more massive (Bourne & Sijacki, 2017).

Given that around 70% of the brightest galaxies in clusters (Brightest Cluster Galaxies; BCGs) are radio loud (Bambic et al., 2018), they are also expected to host radio jets, and so understanding the dynamics of jet interactions is not only instrumental to understanding galaxy evolution, but also to understanding galaxy cluster evolution.

1.2 Galaxy clusters

Galaxy clusters represent the youngest virialised structures in the universe and also hold claim to being the most massive baryonic structures, with masses ranging over $5 \times 10^{13-14} M_{\odot}$ contained in a radius of $1 - 2 \, \mathrm{Mpc}$ (Fabian, 1994). Of particular note is that 75% of the baryonic content of a cluster is present as a hot plasma atmosphere, however this represents only $\sim 12\%$ of the total mass content as approximately 84% is accounted for by dark matter (DM) (Bambic et al., 2018). Given the cluster's exceptional size on the order of a Mpc or more, there are no coherent processes strong enough to compete against gravity, and so rich clusters may comprise a fairly representative sample of the Universe's ingredients (Mathiesen & Evrard, 2001). Clusters also represent deviations from the homogeneous cosmic density profile, and their population statistics may be highly sensitive to a specific cosmological model, testing the Λ cold dark matter model (ΛCDM) and providing insight into the primordial Universe (Mathiesen & Evrard, 2001; Gerke et al., 2005; Robotham et al., 2011).

Clusters are highly luminous at X-ray wavelengths, but are also commonly surveyed in the microwave and radio regimes by the Sunyaev-Zel'dovich effect (Section 1.2.2) and Faraday Rotation (Section 1.3) respectively. Various cluster properties can be measured by each method to varying precision, and by comparing the results of each method, the uncertainties in these parameters can be reduced.

1.2.1 Defining a cluster

Before the cluster environment can be studied, groups and clusters must be identified. This means that individual galaxies must either be assigned to a cluster/group or identified as being lone, and there are many methods to do this over a wide range of wavelengths (Gerke et al., 2005, and references therein): (i) optical photometry, (ii) weak gravitational lensing, (iii) X-ray

emission from hot intracluster gas, (iv) the Sunyaev-Zel'dovich effect (SZ; Section 1.2.2), and (v) direct 3D reconstruction from galaxy redshifts.

These methods each have limitations at high redshift (Gerke et al., 2005):

(i) In photometric surveys, observations of objects at high z means a larger physical depth and increased density of objects within the field, increasing the risk of confusion and contamination.

(ii) Gravitational lensing is observable over an increasingly smaller cross-section for higher z, limiting studies to only the most massive of clusters.

(iii) X-ray surface brightness decreases as $(1 + z)^4$, and since nearer galaxies will intrinsically be brighter, this biases observations towards richer clusters at high redshift. In addition, red early-type galaxies become too faint to observe at a lower redshift than blue late-type galaxies. Thus we are probing only a small fraction of the entire galaxy population with an over-abundance of rare, highly luminous sources.

(iv) Whilst the SZ effect is independent of redshift, it has similar limitations to photometric surveys in terms of confusion. Given that the effect is weak, discerning SZ signals from more local interference is a difficult task.

(v) Using redshift to determine group or cluster membership requires very precise spectroscopic redshift measurements, however most objects at high redshift will only have relatively uncertain photometric redshifts, if they have any at all. Incomplete sampling in redshift-space will always lead to errors when identifying group/cluster members.

In addition to these method-specific challenges, we must also contend with the "finger-of-God" effect: an apparent distortion in redshift-space caused by Doppler shifting of the peculiar motions of galaxies along the line of sight.

The peculiar motion v_{pec} is the component of a galaxy's velocity caused by the gravitational force of the cluster and other galaxies around it. These random motions mean that Hubble's law, $v = H_0 d$, no longer holds within the cluster, and instead becomes:

$$v_r = H_0 d + v_{\text{pec}}, \tag{1.16}$$

where v_r is the total radial velocity of the galaxy, H_0 is the Hubble constant, and d is the distance to the galaxy.

Redshift calculations for galaxies within a cluster are uncertain as a result, which makes it more difficult to identify clearly delineated clusters and groups. Interloper galaxies may be incorrectly assigned to a host group, and multiple small groups may be incorrectly merged into larger structures. Algorithms which attempt to minimise this "over-grouping" may instead classify one large cluster as multiple smaller groups (Gerke et al., 2005), or mistakenly leave out more galaxies from their host cluster. These are unavoidable complications and this creates an optimisation problem which depends greatly on the precise algorithms used. Whilst there are many grouping algorithms currently in use, they can be split into two kinds based on the
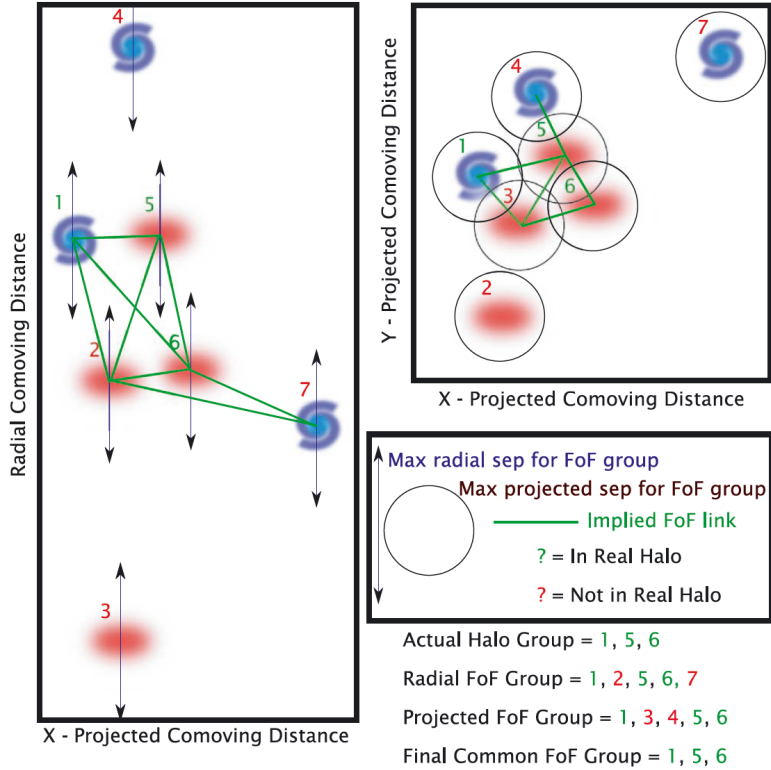
Figure 1.5: A schematic of the two components of the FoF algorithm: the radial frame (*left*) and projected frame (*right top*). Only by combining the results from both cases can a robust cluster or group be defined. Adapted from Robotham et al. (2011).

scale of associations they consider: galaxy-galaxy (e.g. friends-of-friends; FoF) or halo-galaxy (e.g. Voronoi-Delaunay method; VDM) (Robotham et al. 2011; Yang et al. 2007 and references therein).

Friends-of-friends (FoF) algorithm

The friends-of-friends (FoF) algorithm determines membership to a cluster or group based on the physical separation of the galaxies, which is determined for both the radial and projected separations. Links must be longer in the radial case because of the uncertainty introduced by peculiar motion, and galaxies may be grouped together without direct links but instead by the common links between them. As seen in Figure (1.5), neither the radial case nor the projected case are sufficient to determine galaxy grouping alone; the radial and projected groupings must be combined to generate a robust final group (Robotham et al., 2011). This leads to all galaxies being either alone or in groupings with at least one other galaxy.

Yang et al. (2007) use a slightly more complex FoF algorithm known as the *halo-based group finder*, which utilizes an adaptive filter based on assumed properties of dark matter halos. They begin with a a traditional FoF approach, but impose tight constraints on the lengths of galaxy links. These tentative groupings, along with all galaxies which remain ungrouped, are considered as possible group/cluster centres, or *seeds*. For each seed, the characteristic luminosity (corrected for completeness), mass, and velocity dispersion are then calculated from assumed relations. Using these halo parameters, additional galaxies can be associated to group centres, and the process repeats with updated halo parameters in each iteration. Iterations continue until the group/cluster memberships no longer change, which typically requires only three to four iterations. When this algorithm is run over a mock galaxy redshift survey (MGRS), it successfully identified the group centre in $> 90\%$ of cases. In the remaining $\sim 10\%$ of cases, the true central galaxy is either contained in the group but not assigned as the centre, or it was not contained within parent group at all (Yang et al., 2007).

Voronoi-Delaunay Method (VDM)

The Voronoi-Delaunay Method (VDM) is a combination of a Voronoi partition and Delaunay mesh.

The Voronoi partition (or Dirichlet tesselation) generates polyhedral tiles in 3D space containing a central galaxy and all points nearer to that galaxy than any other (Gerke et al. 2005, Figure 1.6). The volume of this polyhedra depends on the number of neighbours a galaxy has: a large Voronoi volume indicates that the galaxy is relatively isolated. Additionally, the Delaunay complex defines tetrahedra in 3D space whose vertices coincide with four galaxies and do not contain any other galaxy (Marinoni et al., 2002).

The first step in applying the VDM is to assign all galaxies their Voronoi cell. In order to quickly identify regions that are likely cluster centres and reduce computation times, the Voronoi cells are ranked in increasing volume; a smaller volume indicates a denser region of space and the corresponding galaxy is more likely to be a seed.

Taking the first seed in this list, we define a cylinder of radius R_I and length $2L_I$, its axis oriented along the line of sight. Any galaxies connected via the Delaunay mesh that also fall within this cylinder are permitted as *first-order Delaunay neighbours*. Searching first within this restricted space reduces the likelihood that interloper galaxies will be assigned to a cluster (Gerke et al., 2005).

The value for R_I used by Marinoni et al. 2002 is $1h^{-1}$ Mpc as this is the typical mean projected separation between galaxy pairs in clusters when grouped by a FoF algorithm, although the authors chose to use a sphere in the first stage instead of a cylinder (Figure 1.7). Gerke et al. 2005 instead found an optimal $R_I = 0.3h^{-1}$ Mpc and $L_I = 7.8h^{-1}$ Mpc. The lengths of the cylinders correspond to the maximum peculiar velocities expected for real systems, which may reach as high as ~ 2000 km s^{-1} (Marinoni et al., 2002).

If no galaxies on the Delaunay mesh fall within the cylinder then that seed is rejected as a lone galaxy. If all of the seed's first-order neighbours are already accounted for by another seed, then the two structures are merged into one.
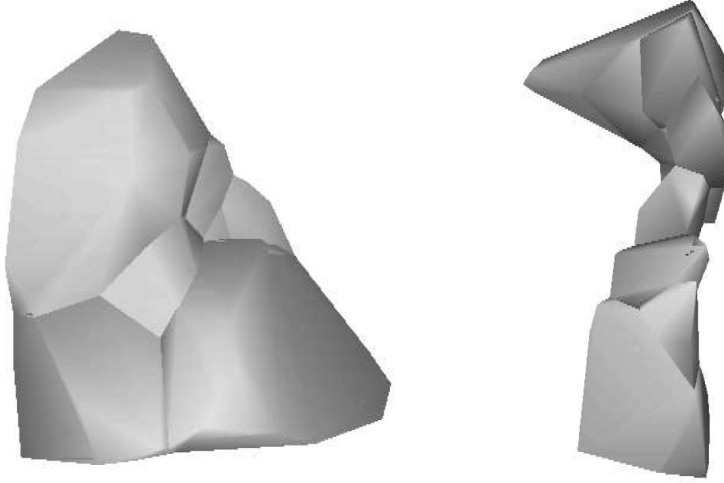
Figure 1.6: The 3D Voronoi cells for a cluster containing 10 galaxies (*left*) in physical-space and (*right*) in redshift-space. Adapted from Marinoni (2010).

Once we reach a seed for which one or more first-order Delaunay neighbours has been found, we then define another larger cylinder with $R_{II} \geq R_I$ and $L_{II} \geq L_I$. Any galaxy within this second cylinder which is also connected via its Delaunay mesh to either the seed or a first-order neighbour is then permitted as a *second-order Delaunay neighbour* (Marinoni et al., 2002; Gerke et al., 2005). The combination of the seed, first-order neighbours, and second-order neighbours (N_{II} galaxies in total) constitutes the core region of a cluster or group (Figure 1.7).

Finally, the total group membership is defined by a final third cylinder. This cylinder is centred on the centre-of-mass of the core region previously defined, and has radius and length defined by (Gerke et al., 2005):

$$R_{III} = r(N_{II}^{\mathrm{cor}})^{1/3} \tag{1.17}$$

$$L_{III} = l(N_{II}^{\mathrm{cor}})^{1/3}, \tag{1.18}$$

where r and l are free parameters which Gerke et al. 2005 found to be $r = 0.35$ and $l = 14$, whilst $N_{II}^{textcor}$ is a scaled version of N_{II} which accounts for the incompleteness of the data at varying redshift.

The combination of N_{II} and those other galaxies found within the third cylinder forms the cluster. The process then repeats with the next remaining seed from the initial list, and continues until all galaxies have either been assigned to a group or identified as being isolated (Gerke et al., 2005).
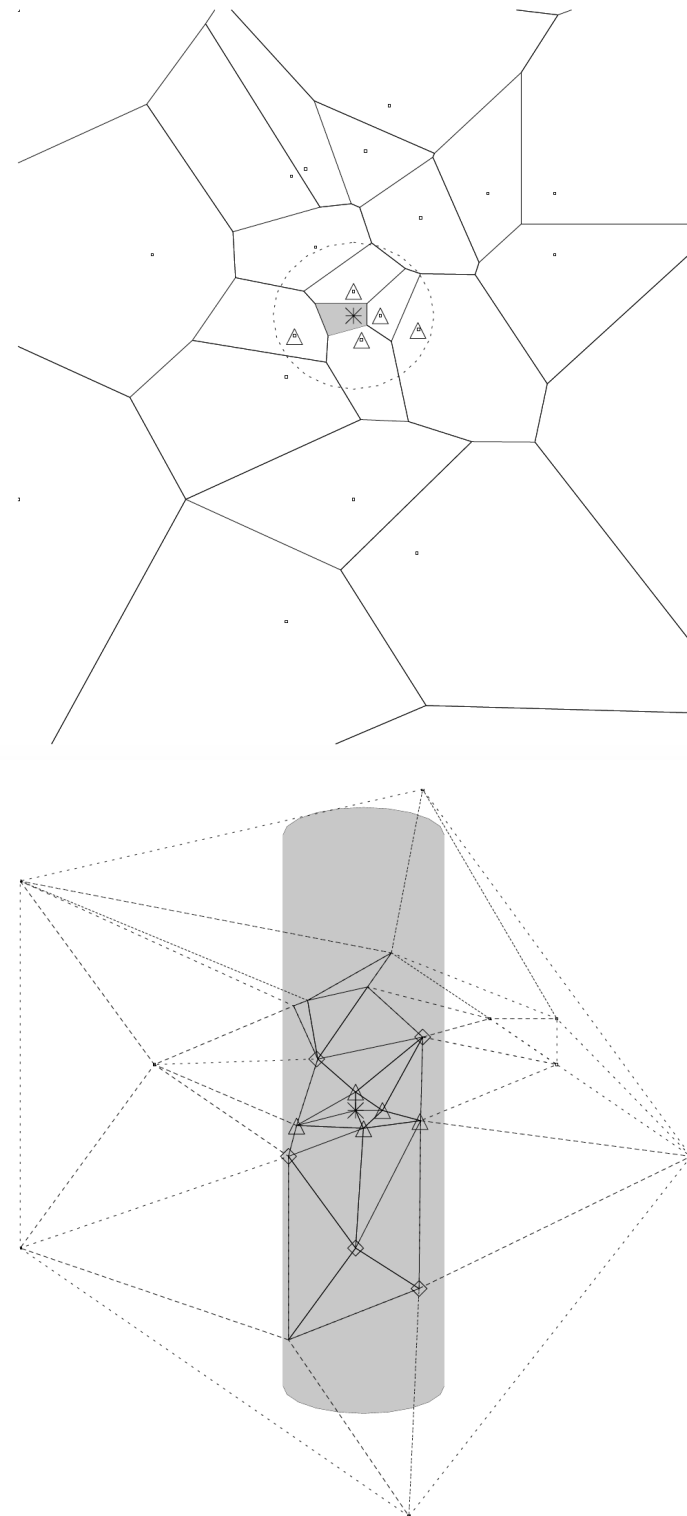
Figure 1.7: *Top:* The two-dimensional version of Phase I of the VDM method, with sky angular position on the x-axis and sky depth on the y-axis. Dots represent individual galaxies. The shaded cell with asterisk is the Voronoi cell identified as the cluster centre, with galaxies marked by triangles being the first-order Delaunay neighbours. *Bottom:* Phase II, including second-order neighbours as diamonds. The shaded region indicates the search area. Adapted from Marinoni (2010).

1.2.2 Determining cluster properties

X-ray observations

Galaxy clusters are the most widespread and luminous extragalactic sources of X-ray emission, with luminosities in the range of $\sim 10^{43-45}$ erg s^{-1} (Sarazin, 1988). As this emission is not time variable, does not exhibit absorption lines, and is highly extended over kpc or Mpc scales, it is not likely to be directly generated by compact sources but is instead truly diffuse. The source of this diffuse X-ray emission was initially hotly debated between (i) thermal bremsstrahlung from the hot intracluster gas, (ii) inverse Compton (IC) scattering of CMB photons, and (iii) stellar X-ray sources. Neither IC scattering nor individual stellar X-rays could explain the observed power-law X-ray spectra and emission lines, or the differing spatial extents of radio and X-ray emission (Sarazin, 1988).

The currently accepted source of the cluster X-ray emission is thermal bremsstrahlung (free-free) emission from the hot intracluster gas of temperature $T_{\mathrm{e}} \approx 10^{7-8}$ K and thermal electron number density $n_{\mathrm{e}} \approx 10^{-3}$ cm^{-3} (Sarazin, 1988). The emissivity of a hot gas at T_{e} composed of ions of charge Z is (Sarazin, 1988):

$$\epsilon_{\nu}^{ff} = \frac{2^5 \pi e^6}{3 m_{\mathrm{e}} c^3} \left(\frac{2\pi}{3 m_{\mathrm{e}} k_{\mathrm{B}}} \right)^{1/2} Z^2 n_{\mathrm{e}} n_{\mathrm{i}} g_{ff}(Z, T_{\mathrm{e}}, \nu) T_{\mathrm{e}}^{-1/2} \exp\left(-\frac{h\nu}{k_{\mathrm{B}} T_{\mathrm{e}}} \right), \qquad (1.19)$$

for electron mass and charge m_{e} and e, ion and electron numbers densities n_{i} and n_{e}, frequency ν, and Gaunt correction factor $g_{ff}(Z, T_{\mathrm{e}}, \nu)$.

If the cluster temperature T_{e} is taken to be approximately constant, then equation (1.19) suggests that the emissivity (and hence the X-ray spectrum) should be an almost exponential function of the frequency. It also predicts that high frequency emission should drop off rapidly. Both effects are observed in galaxy clusters (Sarazin, 1988). The appropriate temperature can be estimated as the intracluster gas must have a velocity dispersion and energy density comparable to that of the cluster galaxies, otherwise it would not be bound by the gravitational potential (Felten et al., 1966; Sarazin, 1988). Hence the velocity of a typical atomic species must be roughly equal to that of the cluster galaxies:

$$\frac{k_{\mathrm{B}} T_{\mathrm{e}}}{\mu m_{\mathrm{p}}} \sim \sigma_{\mathrm{gal}}^2, \qquad (1.20)$$

for intracluster gas temperature T_{e}, mean molecular weight μ, proton mass m_{p}, and galaxy velocity dispersion σ_{gal} along the line of sight. This leads to temperature estimates of:

$$T_{\mathrm{e}} \approx 7 \times 10^7 \text{ K} \left(\frac{\sigma_{\mathrm{gal}}}{1000 \text{ km s}^{-1}} \right), \qquad (1.21)$$

roughly matching that obtained through the X-ray spectrum.

Clusters temperatures are often assumed to be nearly constant, however clusters are known to contain gas at a range of temperatures held in pressure equilibrium (Fabian, 2012). The precise temperatures and their structures are related to the dynamical history of the cluster, and so accurate modelling of temperature is required to constrain cosmological parameters, cooling

flows, and cluster-cluster interactions over cosmic time. This often requires fitting a multi-phase plasma model to X-ray observations.

The X-ray surface brightness is often defined in terms of a so-called β-*model* (Frank, 2013):

$$I_x = I_0 \left[1 + \left(\frac{r}{r_c} \right)^2 \right]^{-3\beta+1/2}, \tag{1.22}$$

for core radius r_c and $\beta \approx 2/3$. This model describes a gas at constant temperature in hydrostatic equilibrium (HE). It matches observations well in the regime of $r_c \lesssim r \lesssim 3r_c$, but underestimates brightness for $r \lesssim r_c$ and overestimates at $r \gtrsim 3r_c$. Irregularities in the surface brightness due to cooling flows, X-ray cavities, shock fronts, mergers, or the presence of a radio source further complicate this distribution (Frank, 2013).

A similar β-model is used for the thermal electron density; the modified King model, based on the initial fit drawn by King in 1972 (King, 1972; Cavaliere & Fusco-Femiano, 1976; Carilli & Taylor, 2002):

$$n_{\mathrm{e}}(r) = n_0 \left[1 + \left(\frac{r}{r_c} \right)^2 \right]^{-3\beta/2}. \tag{1.23}$$

If the temperature profile can be determined, then the total mass of the cluster can also be constrained by simple pressure and gravitational arguments. If we assume that clusters are spherically symmetrical and in a form of HE, then (Frank, 2013)

$$\nabla P = -\rho_g \nabla \Phi \tag{1.24}$$

$$\Rightarrow \frac{1}{\rho_g} \frac{dP}{dr} = -\frac{d\Phi}{dr} = -\frac{GM_{\mathrm{HE}}(x)}{r^2} \tag{1.25}$$

for ICM pressure P, gas density ρ_g, and gravitational potential Φ, gravitational constant G, and mass $M_{\mathrm{HE}}(< x)$ enclosed within radius r_{vir} ($x \equiv r/r_{\mathrm{vir}}$). When combined with the ideal gas law, $P = \rho_g k_{\mathrm{B}} T_{\mathrm{e}}/\mu m_{\mathrm{p}}$, for mean molecular weight μm_{p} (Rasia et al., 2006; Frank, 2013):

$$M_{\mathrm{HE}}(x) = -\frac{k_{\mathrm{B}} T_{\mathrm{e}}(x) x r_{\mathrm{vir}}}{G \mu m_{\mathrm{p}}} \left(\frac{d \ln n_{\mathrm{e}}}{d \ln x} + \frac{d \ln T_{\mathrm{e}}}{d \ln x} \right). \tag{1.26}$$

Hence, if the density and temperature distributions n_{e} and T_{e} are known, the mass enclosed in the cluster $M_{\mathrm{HE}}(r)$ can be determined. The greatest difficulty is in estimating n_{e} and T_{e}, with current models often underestimating the total cluster mass by $\sim 20\%$ as they neglect to capture the true complexity of the ICM.

Another possible model based on HE also takes into account gas velocity v_g (Rasia et al., 2006):

$$M_{\mathrm{HE},v_g}(< x) = -\frac{k_{\mathrm{B}} T_{\mathrm{e}}(x) x r_{\mathrm{vir}}}{G \mu m_{\mathrm{p}}} \left[\frac{d \ln \rho_g}{d \ln x} + \frac{d \ln T_{\mathrm{e}}}{d \ln x} \right]$$
$$- \frac{\sigma_r^2 x r_{\mathrm{vir}}}{G} \left[\frac{d \ln \rho_g}{d \ln x} + \frac{d \ln \sigma_r^2}{d \ln x} + 2\beta_v(x) \right], \tag{1.27}$$

for gas velocity anisotropy parameter $\beta_v \equiv 1 - \sigma_t^2/2\sigma_r^2$, and gas velocity dispersions σ_r and σ_t, radial and tangential respectively.

These fits to the mass profile provide more robust estimates than those which assume a β-model density profile. However, it should be stressed that this does not indicate that a β-model is incorrect; more complex temperature and density profiles make averaging quite complicated (Mathiesen & Evrard, 2001), which greatly affects the apparent outcomes of simulations (Rasia et al., 2006; Stanek et al., 2006).

These models also often fail to account for the presence of cluster magnetic fields, and when studying low-luminosity FR-II radio sources, the added X-ray synchrotron emission makes determination of jet magnetic fields far more difficult (O'Sullivan et al., 2018). Within a homogeneous, isothermal, spherically symmetric cluster the effect would be negligible, however it will play a more significant role in the presence of a clumpy medium. X-ray observations can generally only provide a lower limit to this value of $B \geq 0.1\ \mu$G over scales of ~ 1 Mpc (Gonçalves & Friaça, 1999). Whilst X-ray observations have long played a key role in studying galaxies and galaxy clusters, the X-ray regime alone is not sufficient to constrain all of the necessary parameters for an AGN jet and feedback model.

Sunyaev-Zel'dovich effect

Cluster and intracluster gas properties can also be measured in the radio to microwave regimes.

Low-frequency photons which pass through the ICM may be scattered by free electrons, which move isotropically and are characterised by the optical depth (Sarazin, 1988)

$$\tau_T = \int \sigma_T n_{\mathrm{e}} dl, \tag{1.28}$$

for Thomson scattering cross section $\sigma_T = \frac{8\pi}{3}\left(\frac{e^2}{m_e c^2}\right)^2$. This scattering will change both the direction of propagation and the frequency (ν) of the incident photon (Sunyaev & Zel'dovich, 1972):

$$\frac{\Delta\nu}{\nu} = f\frac{v_e}{c}, \tag{1.29}$$

for electron thermal velocity v_{e}, and proportionality constant f which depends on the difference in velocity between the photon and electron before and after the collision. This is known as the Sunyaev-Zel'dovich effect after Rashid Sunyaev and Yakov B. Zel'dovich, who extensively studied Compton scattering of the cosmic microwave background (CMB) radiation within the ICM (Sunyaev & Zel'dovich, 1972).

One consistent source of photons is the CMB at $T_r \approx 2.7$ K, which is nearly isotropic over the sky with variations at the 10^{-5} level (Sarazin, 1988; Rephaeli, 1995). This isotropy in both the CMB photons and electron velocities means that CMB photons will be scattered to higher or lower frequencies with approximately equal rates, and so this scattering will not be visible in the broad spectrum at first order (Sunyaev & Zel'dovich, 1972). There is, however, a dependence on $\overline{(\Delta\nu)^2}$ which, for electrons, is proportional to $k_{\mathrm{B}}T_{\mathrm{e}}/m_{\mathrm{e}}c^2$; this is known as the *kinetic* Sunyaev-Zel'dovich effect (kSZ). Since the intracluster gas temperature T_{e} is significantly higher than that

of the incident photons T_r, these scattering events also heat the CMB photons, further changing the CMB spectrum (Sarazin, 1988), known as the *thermal* Sunyaev-Zel'dovich effect (tSZ).

The tSZ effect is independent of redshift and can be used to measure the thermal energy of gas in the cluster (Spacek et al., 2017). The change in brightness temperature of these photons under tSZ conditions is given by (in the limit $x \lesssim 10$) (Spacek et al., 2017):

$$\frac{\Delta T_r}{T_r} = y \left[x \coth(x/2) - 4 \right], \tag{1.30}$$

where $x \equiv \frac{h\nu}{k_{\mathrm{B}} T_r} = \frac{\nu}{56.81 \text{ GHz}}$ and y is the dimensionless Compton factor (Spacek et al., 2017):

$$y \equiv \int dl \sigma_T \frac{n_{\mathrm{e}} k_{\mathrm{B}} (T_{\mathrm{e}} - T_r)}{m_{\mathrm{e}} c^2}. \tag{1.31}$$

As photons are conserved in Compton scattering, the incident photons gain energy by their interactions with the hotter thermal electrons, shifting lower frequency photons to higher frequencies, and reducing the intensity in the microwave regime (Sarazin, 1988). This is known as the *microwave diminution*.

IC scattering may also affect the polarisation state of the radiation in clusters, of maximum polarisation degree:

$$P_m = \pm \frac{x e^x}{40(e^x - 1)} \frac{v_t}{c} \tau_T^2, \tag{1.32}$$

where v_t is the tangential component of the cluster velocity. However, this value is exceptionally low even for very fast moving ($v_t = 2000 \text{ km s}^{-1}$), very rich ($\tau_T = 0.03$) clusters, and is likely to be below the detectable threshold in most cases (Rephaeli, 1995).

The tSZ effect is a direct measure of the gas pressure, whilst the kSZ effect gives the column density of the ICM. These are typically measured by X-ray alone, however X-ray has a quadratic dependence on the ICM properties ($\propto n_{\mathrm{e}}^2$) whilst SZ measurements are linearly dependent, meaning it should, in theory, be easier to map the ICM characteristics out to large radii using SZ data (Rephaeli, 1995). In any case, combining the results from both SZ and X-ray analysis is a way to reduce the uncertainty in ICM properties.

Measures of the SZ effect in clusters, when combined with X-ray data, can also provide a route to determining the Hubble constant and the peculiar velocities of clusters, which are of particular interest when studying cosmological models such as ΛCDM (Rephaeli, 1995). The Hubble constant H_0 can be determined by comparing the theoretical expression for angular diameter distance (Rephaeli, 1995):

$$d_A = \frac{c \left\{ z q_0 + (q_0 - 1) \left[(1 + 2 z q_0)^{1/2} - 1 \right] \right\}}{H_0 q_0 (1 + z)^2}, \tag{1.33}$$

with that derived from X-ray and SZ measurements. In equation (1.33), q_0 is the Hubble deceleration parameter which measures the rate of change of H_0 (i.e. the rate of change of the Universe's expansion), and z is the redshift.

By contrast, the angular diameter distance from X-ray and SZ measurements is (Sarazin, 1988):

$$d_A \propto \left(\frac{\Delta T_r}{T_r} \right)^2 f_x^{-1} [T_e(0)]^{-3/2} \theta_c (1+z)^4, \qquad (1.34)$$

for a cluster core of angular radius θ_c and temperature $T_e(0)$, and X-ray flux f_x. This requires we make assumptions about the gas distribution, which will introduce inherent uncertainties. To avoid such assumptions, variations in both X-ray and SZ can be expressed as a function of angle θ away from the cluster core, e.g. (Rephaeli, 1995):

$$d_A = \frac{F[T_e(0)]}{\pi(1+z)^4} \frac{\left(\int_0^\infty [\Delta T_r(0) - \Delta T_r(\theta)] \frac{d\theta}{\theta^2} \right)^2}{\int_0^\infty [I_x(0) - I_x(\theta)] \frac{d\theta}{\theta^2}}, \qquad (1.35)$$

for X-ray surface brightness I_x, and with F being a known function of ICM gas temperature. This only requires that we assume spherical symmetry, which will be accurate for clusters not undergoing merging events.

However, the SZ effect cannot be observed if a radio source is present in the cluster as the increased radio brightness will overshadow the small microwave diminution (Sarazin, 1988). Clusters which contain strong radio sources must be avoided for this analysis, but there remains a risk that weaker radio sources will be present and not accounted for. It also means that cluster environments cannot be measured around individual radio jets, and so the models for ICM properties can only ever be statistical as a result.

Whilst the primary effect being measured is the diminution of intensity at microwave wavelengths, only a small section of the microwave regime can be observed here on Earth and shorter wavelengths must be observed from space (Sarazin, 1988). Without high resolution observations over a wide range of frequencies, the values determined for parameters such as H_0 are inconsistent. McHardy et al. (1990) found $H_0 = 24^{+13}_{-10}$ km s^{-1} Mpc^{-1}, Birkinshaw & Hughes (1994) found $H_0 = 65^{+25}_{-25}$ km s^{-1} Mpc^{-1}, and Jones (1995) found $H_0 = 38^{+18}_{-16}$ km s^{-1} Mpc^{-1}; these values carry large uncertainties and are often inconsistent with the current value of $H_0 = 73.52 \pm 1.62$ km s^{-1} Mpc^{-1} (Riess et al., 2018). This is almost certainly due to the difficulty in reconciling SZ and X-ray measurements.

1.3 Faraday Rotation

An alternative radio measure of cluster properties is through Faraday Rotation. This can provide an *upper* limit measurement of the cluster magnetic field, which may be dynamically important within the cluster (Fabian, 2012). Magnetic field draping has been invoked to suppress and disrupt cooling flows, and without this factor, individual density perturbations in the form of clumps are unstable due to buoyancy and experience convection motions. The presence of a cooling flow will act to amplify the magnetic field by compression, which is observed in cool-core clusters (Fabian, 1994). Neglecting magnetic fields has the potential to greatly impact the way we interpret both observations and simulations.

Faraday rotation is a consequence of the birefringent nature of a magnetised plasma. When a magnetic field $\underline{\boldsymbol{B}}$ is present, any radiation is influenced by the cyclotron frequency (Rybiki & Lightman, 1979):

$$\omega_B = \frac{eB_0}{m_e c}, \qquad (1.36)$$

for field strength $B = |\underline{\boldsymbol{B}}|$, electron charge e and mass m_e, and speed of light c. This is the frequency at which electrons will gyrate around the magnetic field lines.

A birefringent material affects the velocity of electromagnetic radiation differently depending on its circular polarisation because the dielectric constant varies (Rybiki & Lightman, 1979):

$$\epsilon_{R,L} = 1 - \frac{\omega_p^2}{\omega(\omega \pm \omega_B)}, \qquad (1.37)$$

with radiation frequency ω and plasma frequency ω_p, for right (R) and left (L) circular components corresponding to $+$ and $-$ respectively.

Extragalactic sources of circularly polarised emission are relatively rare, however there are many sources (such as radio galaxies and quasars) which produce somewhat linearly polarised emission via synchrotron radiation. Linearly polarised light can be thought of as the superposition of a left-circular and right-circular wave; when it propagates through the magnetised ICM, one polarisation component will travel faster than the other, which is observed as a rotation of the plane of polarisation χ (Figure 1.8) (Burn, 1966; Sarazin, 1988):

$$\chi = \chi_0 + \Delta\chi \qquad (1.38)$$
$$= \chi_0 + \phi\lambda^2, \qquad (1.39)$$

where ϕ is the Faraday depth, and is a function of the cluster density and magnetic field strength (Carilli & Taylor, 2002):

$$\phi = 812 \int_0^s \left[\frac{n_e}{\mathrm{cm}^{-3}}\right] \left[\frac{\boldsymbol{B}}{\mu\mathrm{G}}\right] \cdot \left[\frac{d\boldsymbol{s}}{\mathrm{kpc}}\right], \ \mathrm{rad\ m}^{-2}, \qquad (1.40)$$

for thermal electron number density n_e, and line-of-sight distance $d\underline{l}$. As the magnetic field changes direction and reverses sign along the path, the radiation is rotated through many different planes of polarisation, slowly leading to its depolarisation. Notably, the intrinsic angle of polarisation χ_0 cannot be known for any real source, and so only relative changes to the polarisation angle can be determined, i.e. $\Delta\chi$. It is then the wavelength dependence of $\Delta\chi$ that allows for the determination of the relative polarisation angle (Sarazin, 1988). A related, and often confused, concept is that of the *Rotation Measure* (Vacca et al., 2016):

$$RM \equiv \frac{\partial\chi}{\partial\lambda^2}. \qquad (1.41)$$

When rotation is caused by an a foreground screen, $\phi = RM$, and so the two terms are often used interchangeably. Unless otherwise specified, this work assumes the $\phi = RM$ case.
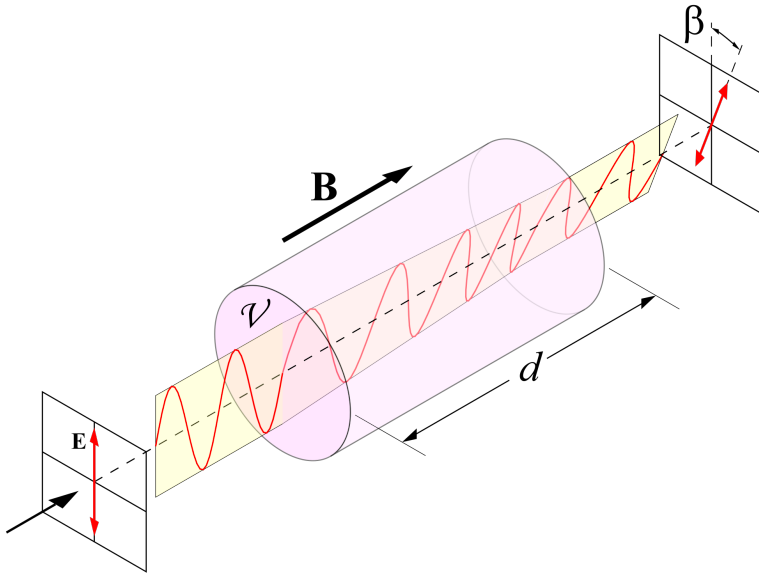
Figure 1.8: Faraday Rotation is the rotation of linearly polarised radiation when it propagates through magnetised media (pink). Here, the change in polarisation angle is given as β. Image from B. Mellish.

Multi-frequency polarimetric observations are able to measure the RM as a function of frequency, which allows the initial polarisation angle χ_0 to be accounted for and removed (Sarazin, 1988); by combining this with estimates of n_e, values for the magnetic field strength can be estimated (Carilli & Taylor, 2002). However, due to the dot-product between $\underline{\boldsymbol{B}}$ and $d\underline{\boldsymbol{l}}$, only the magnetic field component directed along the line-of-sight ($B_{\parallel}$) is measured, and the results will be highly dependent on the assumed topology of the magnetic field.

Faraday rotation provides an upper limit to cluster magnetic fields for $RM \leq 100$ rad m^{-2}, corresponding to $B_0 \sim 1$ μG over a coherence length (scale of reversal) of $l_B \leq 10$ kpc. This corresponds to a ratio of magnetic to thermal pressures of $\leq 10^{-3}$, suggesting that magnetic fields are not dynamically important on large scales (Gonçalves & Friaça, 1999). However, on smaller scales and in regions with cooling flows, RM values can reach as high as 4000 rad m^{-2}, corresponding to $B_0 \geq 10$ μG over $l_B \sim 1$ kpc (Gonçalves & Friaça, 1999).

Faraday rotation and depolarisation may have an external or internal origin. Internal depolarisation occurs when the emission and rotation are occurring in the same region; external polarisation occurs when they are spatially or temporally separate. The emission from radio jets may experience both, first when encountering an outer jet magnetic sheath, and second when encountering the magnetized ICM (Pasetto et al., 2018). Internal and external depolarisation can be differentiated as the former will deviate away from the λ^2 dependence in equation (1.38) when rotated by more than 90° (Burn, 1966). Further, Faraday rotation which arises from a helically-shaped magnetic sheath around the radio jet will produce transverse gradients in RM (Kravchenko et al., 2017). Determination of the magnetic field structure within radio jets is an important step to understanding the observed RM distributions and gradients, although a lack

of sufficiently high resolution observations also limit progress.

Internal depolarisation can be further classified into internal Faraday dispersion (IFD) and differential Faraday rotation (DFR), which differ by the presence of a turbulent magnetic field component. If the magnetic field contains no turbulent component, then the degree of polarisation P is described by DFR (Pasetto et al., 2018):

$$P = p_0 \frac{\sin \phi \lambda^2}{\phi \lambda^2} e^{2i(\chi_0 + \phi \lambda^2/2)}, \tag{1.42}$$

for Faraday depth ϕ. Alternatively, if a turbulent magnetic field component exists, P is described by (Pasetto et al., 2018):

$$P = p_0 e^{2i\chi_0} \left(\frac{1 - e^{-S}}{S} \right), \tag{1.43}$$

where $S = 2\sigma_{RM}^2 \lambda^4 - 2i\phi\lambda^2$ for Faraday dispersion σ_{RM} measuring the turbulence of $B_{\parallel}$. In each case, the radiation which is emitted from the farthest part of the region undergoes a different degree of Faraday rotation compared to that emitted in the nearest part.

Alternatively, Faraday depolarisation may arise from the presence of an intervening Faraday screen containing a turbulent magnetic field. This is external Faraday dispersion (or beam depolarisation), given by (Pasetto et al., 2018):

$$P = p_0 e^{-2\sigma_{RM}^2 \lambda^4} e^{2i(\chi_0 + RM\lambda^2)}. \tag{1.44}$$

Radio observations of Faraday rotation in clusters have shown inhomogeneous magnetic structures over both small and large scales, highlighting the need for magnetic field structures that vary over a range of spatial scales (Nakwacki et al., 2016). In particular, coherence lengths may vary from $5 - 10 \, \text{kpc}$ up to $30 \, \text{kpc}$ (Carilli & Taylor, 2002).

Simple models for the magnetic field have a constant field strength and constant cell size, but random field orientation. The average RM is thus $0 \, \text{rad m}^{-2}$, but the dispersion σ_{RM} will vary proportional to the number of cells travelled by the radiation (Carilli & Taylor, 2002):

$$\sigma_{RM} = \frac{K B n_0 r_c^{1/2} l^{1/2}}{(1 + r^2/r_c^2)^{(6\beta-1)/4}} \sqrt{\frac{\Gamma(3\beta - 0.5)}{\Gamma(3\beta)}}, \tag{1.45}$$

for cell size l in kpc (estimated from coherence lengths), distance r of radio source from cluster centre in kpc, Gamma function Γ, and factor K which depends on the location of the radio source. If the source is embedded at the centre of the cluster, $K = 441$; for a source beyond the cluster, $K = 624$.

More complicated cluster magnetic field structures involve power-law spectra which can implement magnetic flux freezing and follow the profiles of the ICM plasma density and pressure profiles (e.g. Huarte-Espinosa et al., 2011a).

Sufficiently complex models of the ICM magnetic field are necessary in order to interpret phenomena such as the Laing-Garrington (LG) effect (Figure 1.9). The LG effect is an observed
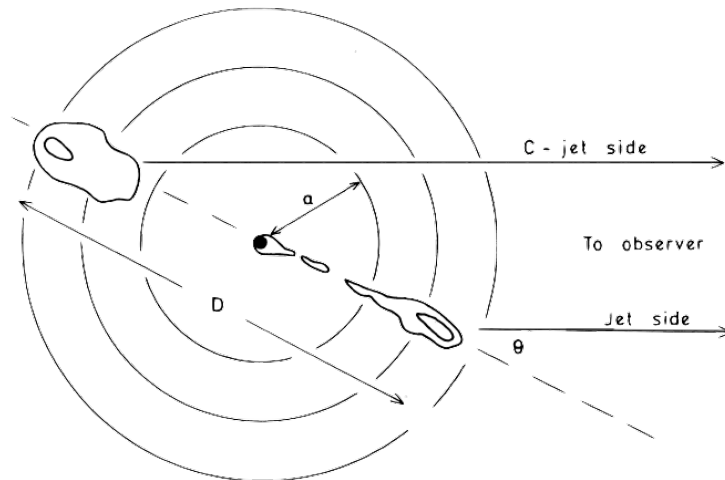
Figure 1.9: Schematic of the Laing-Garrington effect, where greater depolarisation is seen for the receding jet (the "counter-jet", or C-jet above). D is the linear extent of the radio jets, a is the core radius, and θ is the angle between the line of sight and the jet axis. From Garrington & Conway (1991).

asymmetry in the depolarisation of double radio lobes within galaxy clusters (Garrington et al., 1988; Laing, 1988) and is thought to arise when one lobe is pointed away from the observer and the other towards. This results in different path lengths to the two lobes as travelled by the observed radiation, and hence different levels of depolarisation (Garrington & Conway 1991; e.g. Huarte-Espinosa et al. 2011a). If the LG effect can be quantified for a general population, then observations of this effect could provide valuable information on the jets themselves, including the direction of internal magnetic fields and the presence of magnetic cocoons sheathing jets, and physical parameters such as velocity and orientation.

In order to interpret any extragalactic RMs, contaminating signals must be accounted for and removed. Beyond the magnetic fields which exist within the galaxy cluster and radio sources of interest, there are stronger magnetic fields within the ionosphere, interstellar medium (ISM), and intergalactic medium (IGM), along with any contribution from other intervening extragalactic sources/magnetised media (Vacca et al., 2016). Thus, the rotation angle is (O'Sullivan et al., 2018):

$$\chi = \chi_0 + (\phi_{\rm ion} + \phi_{\rm ISM} + \phi_{\rm IGM} + \phi_{\rm EGM})\lambda^2, \qquad (1.46)$$

with Faraday depths for the ionosphere ($\phi_{\rm ion}$), interstellar medium ($\phi_{\rm ISM}$), intergalactic medium ($\phi_{\rm IGM}$), and extragalactic medium ($\phi_{\rm EGM}$) including the extended radio sources. It is necessary to classify these contributions and their dependence on redshift so that they can be removed as the extragalactic component of interest is far weaker than the local Galactic components. Observations at low frequency are particularly impacted due to the λ^2 dependence of Faraday Rotation (Sotomayor-Beltran et al., 2013).

The greatest impact comes from the ionosphere, which leads to a change in polarisation angle of $\sim 228.9°$ for a Faraday depth of $1\ {\rm rad\ m^{-2}}$ observed at 150 MHz (Sotomayor-Beltran et al.,

2013). It also varies with hour, season, line of sight, and level of solar activity, imposing a limit on the lowest observable frequency at ~ 10 MHz. For sources located nearby to Earth or close to the Galactic plane, the Faraday depth of the ionosphere can even exceed that of the total line of sight (Sotomayor-Beltran et al., 2013). If this erroneous signal is not calibrated and removed, it can completely wash out any linear polarisation signals taken over multiple hours or days.

In addition to the ionosphere, the ISM and IGM generate spatial correlations in the observed RMs of extragalactic sources. Much of this coherent component aligns to the Galactic centre and Galactic plane, supporting the existence of a large-scale, regular Galactic magnetic field (GMF) (Pshirkov et al., 2017). Merely subtracting an estimate of the Galactic contribution is unwise as there are still large uncertainties in both observations and the foreground estimates (Akahori et al., 2014; Oppermann et al., 2015).

This difficulty in isolating the extragalactic magnetic field has likely contributed to the disagreements between RM-derived B-fields and that of X-ray observations. Faraday rotation tends to report much greater B field values of $\sim 5 - 30$ μG in comparison to the X-ray derived values of $\sim 0.1 - 1$ μG, however this may be a function of the analytical methods used. RM values are often calculated assuming a single-scale magnetic field, whilst the equipartition values of X-ray observations assume magnetic fields are spatially uniform (Murgia et al., 2004). Such inconsistencies in how magnetic field distributions are modelled makes it difficult to compare and contrast the different methods.

Since Faraday rotation relies on a source of radio emission within the galaxy cluster, rather than trying to avoid them as both X-ray and SZ studies must often do, it is an ideal metric to use in conjunction with studies of AGN jets. What remains is to model and observe this phenomena to sufficiently small scales. Recent computational advancements mean that the biggest limiting factor on Faraday Rotation studies is observational.

1.4 Advancements in observations

Measurements of cluster properties are limited by the uncertainties in our observations. As advancements are made in terms of resolution, our understanding of AGN jets and their host environments will greatly increase. In particular, new radio interferometers with larger bandwidths will provide a sufficiently high resolution in Faraday rotation measures to distinguish between near and far Faraday components (Vacca et al., 2016). This will allow us to more easily disentangle Galactic RM components and study the different magnetic field structures within jets and the surrounding environment, placing better constraints on jet-environment interactions, AGN feedback, and galaxy evolution. Observational uncertainties will be lower at lower frequencies, so the Low-Frequency Array (LOFAR) and Square Kilometre Array Low (SKA-Low) are of particular interest. However, there are far fewer sufficiently polarised sources for frequencies between $50 - 350$ MHz, so calibration of this data set could prove to be a complex task (Vacca et al., 2016). Once calibration is achieved, these surveys will provide us with very high precision RM measures (Sotomayor-Beltran et al., 2013). The higher frequency VLA Sky Survey (VLASS) is better suited to perform a deep field survey as wide and shallow sky surveys are already covered in its frequency range.

Spectroscopic redshifts are also a pivotal requirement for improving accuracies. Recent optical surveys such as the Two Micron All-Sky Survey (2MASS), the Wide-field Infra-red Survey Explorer (WISE), and the SuperCOSMOS Sky Survey (SSS) have measured the photometric redshifts of millions of galaxies at low redshift ($z \lesssim 0.5$) with newer surveys set to greatly increase this number (Vacca et al., 2016), however photometric redshifts are far less accurate than spectroscopic, and these low accuracies are passed on to calculations of other parameters. A highly complete sample of spectroscopic redshifts may be provided by the multi-wavelength Galaxy And Mass Assembly (GAMA) survey.

Beyond the science contributions of individual surveys or facilities, it is essential that multi-wavelength data is pooled and compared across the entire sky. With the advent of new technologies that have the potential to probe to ever-increasing resolutions and sensitivities, there will be significant challenges in storing, calibrating, identifying, classifying, and analysing this data (Norris et al., 2013). By considering a wide range of frequency-space, the physics of radio galaxies and their evolution over cosmic time can be understood to a far greater degree.

Here, a select number of next-generation surveys and facilities are briefly reviewed, along with some of their precursors.

1.4.1   The Low-Frequency Array

The Low-Frequency Array (LOFAR) is a next-generation radio interferometer completed in 2012, composed of an array of 48 dipole antennas located throughout Europe and the Netherlands. As these antennas are stationary, they are pointed electronically and the signals combined into a digital phased array to give a large field-of-view (FoV) across $10 - 240$ MHz. In addition to this large FoV, LOFAR can also achieve a sub-arcsecond angular resolution over much of this bandpass (van Haarlem et al., 2013). LOFAR has been an important pathfinder and technological precursor to the upcoming SKA as a result (Norris et al., 2013).

As discussed previously, calibration of low frequencies is a difficult task due to inference from the ionosphere, and so Faraday Rotation observations are typically limited to the high band antennas (HBA) from $120 - 160$ MHz (Vacca et al., 2016). LOFAR is generally not ideal for Faraday Rotation surveys: its linear feeds are more sensitive to circular polarisation than linear, meaning it is difficult to observe faint linearly polarised sources (Farnes et al., 2018). Additionally, if the expected number of $\sim 1\%$ polarised extragalactic sources is 1 per 1.7 deg^2, then LOFAR's detection threshold of 500 μJy/beam at a resolution of $20''$ would only supply a signal-to-noise of 5 (Vacca et al., 2016). There is an advantage to having < 1 source per square degree though, which is that confusion of sources is much less likely.

1.4.2   The Square Kilometre Array

The Square Kilometre Array (SKA) is an internationally supported radio telescope, spanning a consortium of 17 countries and with an expected completion of ~ 2030. Observations will be undertaken over centimetre to metre wavelengths using thousands of antennas spread over an effective area of 1 km^2 in both Australia and South Africa (Norris et al., 2013). Surveys under-

taken with the SKA will follow a "tiered" approach, increasing the sensitivity over increasingly smaller survey areas as sources of particular interest are highlighted. Phase I of SKA operations (SKA1) will commence with an all-sky survey of $31,000\,\mathrm{deg}^2$ over $1-2$ GHz, a resolution of $2''$, and a sensitivity of $2\,\mathrm{mJy}$. Once completed, the angular resolution for $0.5-10$ GHz will decrease to $\lesssim 40-2$ mas, with sensitivity increasing to $\lesssim 50\,\mathrm{nJy/beam}$ (brightness temperature $\lesssim 200$ K) for an 8-hour observation over a 500 MHz bandwidth (Godfrey et al., 2012): ~ 50 times more sensitive than any previous radio observatory (Johnston-Hollitt et al., 2014). At redshifts out to $z = 7$, the SKA will be able to discern between the earliest starburst galaxies and the earliest AGN jets, probing a large range of SMBH masses and accretion rates over cosmic time (Godfrey et al., 2012).

The sensitivity in polarisation is expected to reach $\approx 4\,\mu\mathrm{Jy/beam}$, leading to source densities 200-300 times greater than currently available. When coupled with the smaller angular resolution, this means that optical counterparts can be resolved more readily, allowing a greater number of sources to be assigned an initial photometric redshift (Vacca et al., 2016) which can then be followed up with spectroscopy. When extended radio sources are resolved, the spatial correlations between intrinsic and extrinsic Faraday Rotation can also be investigated (Vacca et al., 2016).

In addition to providing better information on radio sources of interest, the precise astrometry possible with the SKA will also assist in modelling the GMF. The SKA will obtain RMs for ~ 100 pulsars deg^{-2} ($\sim 2\times$ greater than the recent NRAO VLA Sky Survey (NVSS) RM catalogue; Norris et al. 2013), however these require accurate parallax measurements and precise electron density modelling to interpret correctly, and current pulsar distance uncertainties sit at $\sim 10\%$. The greatly improved parallax measurements which the SKA can offer may produce the best GMF model yet (Godfrey et al., 2012).

Given the trail-blazing nature of the SKA project, multiple specially-built "pathfinder" projects are underway to develop the new technologies required and refine existing techniques in preparation for the SKA-era.

The Australian SKA Pathfinder

The Australian SKA Pathfinder (ASKAP) is an SKA precursor and technology demonstrator completed in 2012, running over $700-1800$ MHz (Tingay et al., 2013) on a phased-array system. Its continuum mode can survey the Southern Sky approximately 50 times faster than achieved by the VLA for NVSS (Johnston et al., 2008). It will complete 10 projects in key SKA science areas: the Evolutionary Map of the Universe (EMU), the Widefield ASKAP L-Band Legacy All-Sky Blind Survey (WALLABY), Compact Objects with ASKAP: Surveys and Timing (COAST), the Commensal Real-time ASKAP Fast Transients survey (CRAFT), Deep Investigations of Neutral Gas Origins (DINGO), the First Large Absorption Survey in HI (FLASH), the Galactic ASKAP Spectral Line Survey (GASKAP), the Polarization Sky Survey of the Universe's Magnetism (POSSUM), the Variables and Slow Transients survey (VAST), and VLBI.

Of particular interest to this thesis are EMU and POSSUM.

EMU is a deep radio continuum survey spanning the entire Southern Sky and part of the lower

Northern Sky ($\lesssim +30°$). With a sensitivity and angular resolution far better than that of NVSS, EMU is expected to observe ~ 70 million radio galaxies; a 35-fold increase to current catalogue numbers and all within the public domain (Norris et al., 2013). When combined with the Northern field of the Westerbork Observations of the Deep APERTIF Northern-Sky (WODAN) surveys, it will produce an all-sky radio survey at 1.3 GHz, $\sim 10 - 15''$ resolution, and rms noise 10 μJy/beam. The overlap region between EMU and WODAN will allow for robust cross-checking and consistent calibration (Norris et al., 2013).

Complementary to EMU is POSSUM: the all-sky linear polarisation survey between $1130 - 1430$ MHz, with a sensitivity of < 10 μJy/beam and resolution of $10''$ (Vacca et al., 2016). It is expected that POSSUM will obtain RMs for ~ 3 million compact extragalactic sources along with upper polarisation limits to all EMU sources. Measurements of compact sources will then be used to study and constrain the GMF and ISM variability (Norris et al., 2013). External and internal depolarisation processes can produce similar behaviours in linear and circular polarisations when viewed over a narrow frequency range, and so the wide frequency range of EMU is well-suited for studying the line-of-sight GMF (Mao et al., 2014).

The Murchison Widefield Array

Another precursor to the SKA is the Murchison Widefield Array (MWA), co-located with ASKAP at the Murchison Radio-astronomy Observatory (MRO) in the Murchison Squire of Western Australia. It was the first precursor out of the SKA three (MWA, ASKAP, MeerKAT) to be completed. It consists of 128 aperture arrays ("tiles"; 2048 dipole antennas total) over a region of ~ 3 km diameter, operating at low frequencies of $80 - 300$ MHz in both linear polarisations. Located in the extremely low-interference site at the MRO, it lays claim to being the most capable low-frequency radio telescope in the Southern Hemisphere (Tingay et al., 2013).

The MWA is comparable to LOFAR in terms of its wide FoV ($25°$ FWHM at 150 MHz; Arora et al. 2016) and to the Giant Metrewave Radio Telescope (GMRT) in terms of sensitivity. This is an impressive feat given its novel approach and new astronomical techniques, particularly in terms of electronic steering. The placement of the MWA in the Murchison Squire provides us with exceptionally low radio interference, but this seclusion comes at the cost of site accessibility. Similar issues are expected with the final SKA product, and the lessons learned in operating the MWA (and companion precursor, ASKAP) will be invaluable (Tingay et al., 2013) in this regard.

As with LOFAR, the low frequencies of the MWA means trouble for detecting polarised sources. In a survey undertaken over $170 - 200$ MHz with spatial resolution $15.6'$, area 2400 deg^2, and total intensity sensitivity of 200 mJy/beam, only one polarised source was detected out of all sources with brightness > 4 Jy, suggesting that most sources have fractional polarisations $< 2\%$ at these frequencies (Bernardi et al., 2013). However, the low number density of observed polarised sources may be due to beam depolarisation of weak sources, and so any predictions about extragalactic magnetic fields from this data depend largely on the assumptions made to analyse it (Vacca et al., 2016). As low frequencies are particularly sensitive to ionospheric distortion ($\propto \nu^{-2}$), careful calibration of the sky sensitivity patterns is crucial (Hurley-Walker

et al., 2017).

The MWA's flagship survey is the GaLactic and Extragalactic All-sky MWA (GLEAM) survey, covering the entire Southern Sky below declination $+25°$ ($\sim 25,000 \ \mathrm{deg}^2$), excluding declinations near the Galactic place and the Magellanic Clouds, from $72 - 231$ MHz. Observations in GLEAM began in 2013 and ran for two years, observing 307 455 radio sources with a resolution of $\approx 2'$. The catalogue is estimated to be 90% complete at a flux density of 170 mJy and 50% complete for 55 mJy (Hurley-Walker et al., 2017).

1.4.3   The Jansky Very Large Array

The Jansky Very Large Array (JVLA; previously the VLA) is a component of the National Radio Astronomy Observatory (NRAO) and is located in central New Mexico. It consists of 27 radio telescopes, each with diameter 25m, arranged in a 'Y' formation that can provide up to 351 independent baselines. The JVLA has a historic record in sky surveys, and has been used previously to generate the NRAO VLA Sky Survey (NVSS) and the Faint Images of the Radio Sky at Twenty-Centimeters (FIRST) Survey. Starting in September of 2017, the new VLA Sky Survey (VLASS) was launched.

VLASS operates at a low frequency range of $1-1.75$ GHz for L-band and $2-4$ GHz for S-band, with an angular resolution of $13''$ and an expected sensitivity of $10 \ \mu\mathrm{Jy/beam}$ (for 300 MHz bandwidth over 12 hours; Vacca et al. 2016). With a large FoV of $8 \ \mathrm{deg}^{-2}$, VLASS is a valuable instrument in studying polarisation and cosmic magnetic fields. If used for a widefield survey, it is expected to observe > 4 million radio sources and $> 2.2 \times 10^5$ polarised sources (Mao et al., 2014) however all-sky surveys for this frequency range will be well-serviced by the Westerbork Synthesis Radio Telescope (WSRT) and ASKAP; VLASS may be better suited to a deep field of interesting sources (Hales, 2013). The VLA A-configuration provides the longest baselines and can achieve a resolution of $< 2''$, making it the optimal telescope for morphological studies of faint radio galaxies.

Observations in $2 - 4$ GHz can probe the Faraday depths of extended polarised structures to a scale ~ 4 times larger than that at $1 - 1.75$ GHz. Whilst the resolution of these observations by VLASS are worse ($\sim 200 \ \mathrm{radm}^{-2}$)than the equivalent observations in L-band, precision is greatly improved ($\sim 40 \ \mathrm{radm}^{-2}$) when supplemented by data from WODAN and POSSUM (Mao et al., 2014).

1.4.4   The Galaxy And Mass Assembly survey

The Galaxy And Mass Assembly (GAMA) survey combines the latest-generation survey facilities to form a comprehensive multi-wavelength spectroscopic catalogue of low redshift galaxies. GAMA observations ran on the 3.9m Anglo-Australian Telescope (AAT) over 210 nights between $2008 - 2014$, covering a sky area of $\sim 286 \ \mathrm{deg}^2$ and generating reliable spectroscopic redshifts for $238,000$ objects (Liske et al., 2015). These observations are largely augmented by the Sloan Digital Sky Survey (SDSS) and the 2dF Galaxy Redshift Survey (2dFGRS), and coordinated alongside many independent survey teams, including four space missions and eight

Survey	Facility	Wavelengths/Bands	
XLL	*XMM-Newton*[a]	$0.5 - 2$ keV	X-ray
GALEX-GAMA	*GALEX*[b]	$0.15, 0.22 \ \mu$m	ultraviolet
SDSS DR7	Sloan telescope	*u, g, r, i, z*	visible
VST-KIDS[c]	*VST*[d]	*u, g, r, i,*	visible
CFHTLenS[e]	*CFHT*[f]:	*u, g, r, i, z*	visible
UKIDSS LAS[g]	*UKIRT*[h]	*Y, J, H, K*	near-infrared
VIKING[i]	*VISTA*[j]	*Z, Y, J, H, K_s*	near-infrared
WISE All-Sky DR	WISE	$3.4, 4.6, 12, 22 \ \mu$m	mid-infrared
H-ATLAS[k]	Herschel	$100, 160, 250, 350, 500 \ \mu$m	far-infrared
DINGO	ASKAP	21 cm	radio
GMRT-GAMA	GMRT	92 cm	radio

Table 1.1: The independent surveys which GAMA samples, with their associated facilities and observing wavelengths/bands. From Liske et al. 2015 and references therein.

[a] X-ray Multi-Mirror Mission

[b] Galaxy Evolution Explorer

[c] VST-Kilo-Degree Survey

[d] VLT Sky Telescope

[e] CFHT Lensing Survey

[f] Canada-France-Hawaii Telescope

[g] UKIRT Infrared Deep Sky Survey Large Area Survey

[h] United Kingdom Infra-Red Telescope

[i] VISTA Kilo-Degree Infrared Galaxy Survey

[j] The Visible and Infrared Survey Telescope for Astronomy

[k] Herschel Astrophysical Terahertz Large Area Survey

ground-based facilities (Liske et al. 2015 and references therein, Baldry et al. 2010 and references therein; Table 1.1).

The primary objective of GAMA is to produce a catalogue of galaxies with exceptionally uniform spatial completeness; an objective GAMA has achieved with $\sim 98\%$ completeness within r-band (Robotham et al., 2011). This complete sample can then be used to analyse low-mass groups ($M_g \leq 10^{13}h^{-1}M_\odot$), which help to constrain the low mass regime of dark matter (DM) halos and the halo mass function (HMF). With this mass regime filled in, galaxy evolution can then be studied as a function of halo mass and tests can be performed on the cold dark matter (CDM) paradigm (Driver et al., 2011).

With precise galaxy redshifts and distances, combined with sky distributions, we can infer the clustering properties of galaxies including their velocity dispersion within clusters and groups (Baldry et al., 2010).

1.5 Conclusions and thesis structure

Relativistic plasma jets emanating outwards from supermassive black holes (SMBHs) have a far-reaching effect on the evolution of their host galaxy (Section 1.1). Their mass is strongly correlated to the velocity dispersion of stars within the host galactic bulge (the $M_{\mathrm{BH}} - \sigma$ relation; Martín-Navarro & Mezcua 2018), and the process through which material accretes onto the central engine may stop or start radio jets, impacting the kinematics of the reservoir of gas from which the BH feeds (Fabian, 2012).

The physics of the jet-environment interaction is well understood from a theoretical perspective (Subsection 1.1.3); however, the galaxy cluster environments surrounding real SMBHs are challenging to measure observationally in general. The X-ray observations which underpin our knowledge of cluster environments are biased towards dense, nearby objects (Gerke et al., 2005), leading to inadequate knowledge of the host environments for much of the population (Subsection 1.2.2). This makes it difficult to quantify the effect SMBH jets have on their host galaxy.

Faraday Rotation of AGN jets is a promising method to help constrain properties of both the galaxy cluster and the radio sources themselves (Section 1.3). It is the effect of depolarisation of radio emission as it travels through magnetised media in the form of the intervening intracluster, intergalactic, and interstellar media (ICM, IGM, and ISM respectively), and is a function of both the thermal electron number density n_{e} and the magnetic field distribution $\underline{\boldsymbol{B}}$ within those regimes. A closely related concept which may be applicable is that of the Laing-Garrington effect – an observed effect in which one lobe of a double radio source is preferentially depolarised, thought to arise due to the orientation of the radio lobes with respect to the line of sight. This effect is independent of Doppler beaming, and may be apparent even for sources at relatively large angles to the line of sight. For these reasons, Faraday Rotation may provide critical information both on the internal radio source dynamics and on the intervening magnetised medium, and augmentation of current X-ray data with additional Faraday Rotation measures may improve our knowledge of AGN jets, their surrounding environments, and their later evolution.

The use of Faraday Rotation in inferring AGN jet and galaxy cluster properties is currently

limited by the resolution of radio surveys; the next generation of radio arrays operating at low frequencies of $204 - 232$ MHz such as the Low-Frequency Array (LOFAR) and the Murchison Wide-field Array (MWA, precursor to the Square Kilometre Array) will provide much new data, although the former is not ideally suited to studies of Faraday Rotation as it is not highly sensitive to the linearly polarised sources such as those emitting synchrotron radiation, i.e. AGN radio lobes. Nonetheless, observations in this frequency range promise a wealth of new insights into Faraday Rotation of AGN jets, and will further complement data from existing Very Large Array (VLA) surveys such as the NRAO VLA Sky Survey (NVSS) and the Faint Images of the Radio Sky at Twenty-Centimeters (FIRST) survey, both at approximately 1.4 GHz.

This thesis is structured as follows. In Chapter 2, observational evidence for the surrounding environment as a cause of radio source asymmetry is presented, supporting the idea that greater understanding of the jet-environment interaction is warranted and necessary. A series of analytically-tractable theoretical models for galaxy clusters and embedded FRII double radio sources are formed in Chapter 3, and the effect of varying these models is investigated with respect to the Rotation Measure (RM) signature which would be observed. This model is improved upon in Chapter 4, in which the dynamical *Radio AGN in Semi-analytic Environments* model (RAiSE; Turner & Shabala, 2015) is used to determine more physically-realistic radio source properties over time when observed at both $204 - 232$ and 1400 MHz. Within the same chapter, the utility of Faraday Rotation in helping to constrain radio source and environment parameters is tested by χ^2 parameter estimation of a series of random test models. The conclusion is given in Chapter 5, alongside a discussion of the results of this work and its potential for application.

CHAPTER 2

Radio Galaxy Zoo: observational evidence for environment as the cause of radio source asymmetry

The following chapter is an excerpt of a manuscript submitted for publication in MNRAS in original form 2018 July 24, and accepted 2018 November 8 pending printing. Here, evidence for the effect of environment on asymmetrical radio sources is given, highlighting the need for observed metrics which may constrain such properties as cluster or group halo mass.

Once a jet is triggered, environment plays an important role in determining the final lobe morphology. At low redshift, edge-darkened, or Fanaroff-Riley (FR; Fanaroff & Riley, 1974) Type I, objects are mostly found in clusters, while edge-brightened, or FR-II, sources prefer poorer environments (Hill & Lilly, 1991). FR-IIs have higher radio luminosities than FR-Is, and the two FR classes show a difference in characteristic radio luminosity which increases with host galaxy optical luminosity (Owen & Ledlow, 1994); however, both FR classes show a large scatter and overlap in radio luminosity (Best, 2009; Miraghaei & Best, 2017). This morphological distinction is an important factor in the radio source–environment interaction: while FR-Is provide gentle, quasi-continuous heating to cluster cores (e.g. Churazov et al., 2001; Fabian, 2012), FR-IIs drive powerful shocks capable of affecting satellite galaxies on scales of hundreds of kiloparsecs (Rawlings & Jarvis, 2004; Shabala et al., 2011). There is a loose association between FR morphology and optical classification, in the sense that almost all FR-Is are LERGs, but FR-IIs can be hosted by both high and (less often) low-excitation galaxies. A growing consensus appears to be that the FR classification may be determined by jet-environment interaction on approximately kiloparsec scales: if the initially relativistic jet can be slowed down sufficiently via entrainment from the interstellar medium (Bicknell, 1995) or stellar winds (Komissarov, 1994; Perucho et al., 2014), it will eventually be disrupted and form a FR-I; on the other hand, if the jet is not entrained appreciably, it will form a characteristic FR-II structure with lobes inflated via backflow of overpressured plasma from jet termination shocks, seen in radio images as hotspots. Alternatives to jet entrainment are jet stalling in a rising pressure profile (Massaglia et al., 2016), or failed collimation of an initially conical jet by the environment (Alexander, 2006; Krause

et al., 2012); both are followed by eventual jet disruption and transition to an FR-I as a result of jet–environment interaction. A small fraction (less than 1 per cent; Gawroński et al., 2006) of extended radio sources show hybrid morphologies (Gopal-Krishna & Wiita, 2000; Kapińska et al., 2017), with FR-I morphology on one side of the central engine, and FR-II morphology of the other. These objects are ideal laboratories for studying the interaction of the small-scale jets with their environment: the two jets are intrinsically identical, and the difference in the final morphology can be attributed to different kinds of interaction with the environment.

On larger scales (tens and hundreds of kpc), environment is a key factor in lobe (rather than jet) evolution. Dynamical radio source models (e.g. Kaiser & Alexander, 1997; Blundell & Rawlings, 2000; Turner & Shabala, 2015; Hardcastle, 2018) and numerical simulations (Hardcastle & Krause, 2013, 2014) predict that the temporal evolution of lobe size and luminosity should be strongly environment dependent; these predictions are consistent with X-ray observations (Arnaud et al., 2010). Compact radio AGN are more prevalent in low-mass galaxies and poor environments (Shabala, 2018), consistent with models in which extended emission may be below the surface brightness detection threshold of existing instruments (Shabala et al., 2017; Turner et al., 2018b); recent increased sensitivity observations of giant lobes in the archetypal FR-I source 3C31 (Heesen et al., 2018) confirms this picture. Estimates of AGN lifetimes and jet kinetic powers from radio continuum data are therefore environment-dependent, and hence so too are estimates of the energy budget available for AGN feedback; this feedback process is responsible for shaping the bright end of the galaxy luminosity function (Silk & Rees, 1998; Bower et al., 2006; Croton et al., 2006). Environment quantification through galaxy clustering provides a natural connection between galaxy formation and lobe evolution models. Turner & Shabala (2015) used a semi-analytic galaxy formation model to quantify radio source environments, and showed that this approach can explain many properties of the observed radio galaxy populations. Shabala & Alexander (2009) and Raouf et al. (2017) modelled radio AGN and galaxy properties self-consistently within a semi-analytic galaxy formation model, and showed that the requirement to match radio AGN and galaxy properties simultaneously places powerful constraints on feedback models.

In this work, we present an analysis of a sample of Radio Galaxy Zoo (hereafter RGZ; Banfield et al., 2015) radio galaxies with large-scale environment information from galaxy clustering. The focus of the paper is on exploring the relationship between the asymmetry in radio lobe properties, and asymmetry in radio source environments quantified through galaxy clustering. We present our sample in Sections 2.1 and 2.2, and discuss the role of environment on lobe evolution in Section 2.3. We conclude in Section 2.4.

Throughout this chapter, we assume a flat Universe with $H_0 = 68 \, \mathrm{km \, s^{-1} \, Mpc^{-1}}$, $\Omega_\Lambda = 0.685$ and $\Omega_\mathrm{M} = 0.315$ (Planck Collaboration et al., 2014).

2.1   Sample selection

The starting point for our sample is the set of multi-component radio sources identified by citizen scientists through the Radio Galaxy Zoo project (Banfield et al., 2015). RGZ enlists citizen scientists to classify 1.4 GHz radio continuum images from the Faint Images of the Radio Sky at

Twenty Centimeters (FIRST; Becker et al., 1995) and the Australian Telescope Large Area Survey (ATLAS; Norris et al., 2006; Middelberg et al., 2008) projects. RGZ offers to its volunteers a superposition of these radio images with mid-infrared images at $3.4\,\mu$m from the Wide-field Infrared Survey Explorer (WISE; Wright et al., 2010) and at $3.6\,\mu$m from the Spitzer Wide-Area Infrared Extragalactic Survey (SWIRE; Lonsdale et al., 2003). Citizen scientists are asked to identify whether separate radio source components may belong to a single radio structure, and whether there is a corresponding infra-red host galaxy. Upon achieving a sufficient number of classifications for one image (20), the consensus level C is evaluated for the radio and infra-red classifications of each source. The consensus on the position of the host galaxy is then determined through application of a kernel-density estimator (KDE) on the positions clicked by the volunteers since these positions may differ by a few pixels and yet be identifying the same source. We refer the interested reader to Banfield et al. (2015) for further details.

The initial dataset contained 2679 candidate sources with double or triple radio components from the subset of the RGZ catalogue investigated by Banfield et al. (2015). The sample was reduced to those sources with a consensus level above 0.7 and redshift $z < 0.3$, reducing the sample to 169 sources. Radio lobes were required to be approximately straight to allow for accurate quantification of lobe length and environment (within ~ 10 degrees; see below), reducing the sample to 89. We required at least one of the radio lobes to be at least 100 kpc in length as measured along a straight line from the host to the emission region farthest from the host, to help ensure sufficient image resolution. Finally, an integrated flux density threshold of 20 mJy was imposed to ensure sufficiently high signal to noise ratio.

In this work we seek to probe the relationship between radio source morphology and environment; this is achieved using the Sloan Digital Sky Survey (SDSS) DR8 (Aihara et al., 2011) to quantify galaxy clustering near our radio sources. To ensure robust quantification of the environment, we required each source to have at least 20 galaxies within a projected distance of 1 Mpc of the host galaxy. Neighbouring galaxies were associated to the host using photometric redshifts; galaxies with photometric redshifts consistent with the host spectroscopic or photometric redshift (within 1σ uncertainties, provided these were less than 10 percent of the host redshift) were admitted as neighbours. These neighbours must number 20 or more for the source to be included in our sample. The threshold galaxy counts requirement biases the sample against sources in poor environments, but makes our analysis more robust to outliers.

Our final sample consists of 23 extended RGZ sources seen in the FIRST survey at $z < 0.3$ with environment information. Radio and optical images of these sources and their surrounding environment are presented in Appendices A and B, with one example of each class (FR-II, FR-I and hybrid) shown in the main text.

2.2 Results

The objective of this work is to investigate the relationship between asymmetries in radio source properties and those of its environment. Below, we briefly outline quantitative measures of asymmetry in radio source size, luminosity and morphology, as well as environment as described by galaxy clustering.

2.2.1   Radio source properties

Following the approach of Fanaroff & Riley (1974), radio lobes were separated into Fanaroff-Riley Type I (edge-darkened) or Type II (edge-brightened) morphological classes; radio sources with lobes of different morphology (i.e. FR-I on one side of the central engine, FR-II on the other) are classified as hybrids. Visual classifications were performed by three of the authors (PR, RJT, SSS), resulting in 16 FR-IIs, 6 FR-Is and one hybrid. The Northern lobe of one further source, RGZ J102733.6+481718, has a borderline FR-I/II morphology and could not be reliably classified; this source was excluded from further analysis. Figure 2.1 shows one of our FR-II sources and an example of an FR-I; and the hybrid source is shown in Figure 2.2. The remaining FR-II sources are presented in Appendix A, and FR-I sources in Appendix B. Relevant properties of all sources in our sample are given in Table 2.1.

We define the spatial extent of each source by the outermost 5σ contours ($\sigma \sim 0.15$ mJy/beam). Following Turner et al. (2018a), the source is divided into two radio lobes by finding the two most extreme points and associating the other pixels of emission to the extreme point on the same side of the active nucleus. A rectangular box is then fitted to each lobe so that it intersects the extreme point and has the active nucleus bisect the opposite edge; the box is rotated so that the two edges parallel to the lobe major axis are tangent to the 5σ contour (see Figure 2.3). The length of each lobe is then taken to be the length of this rectangular box outwards from the central engine, and the flux density as the integrated surface brightness. The uncertainty in these parameters is quantified by comparing these estimates to those fitted assuming a lower 3σ contour. For FR-II sources, the lobe length thus defined typically corresponds to the distance between the core and edge of the lobe. For FR-Is, lobe length defined in this way will necessarily be sensitivity limited (e.g. Turner et al., 2018a), however our analysis below is still valid as we are interested in the difference between two lobes of the same source.

We use the location of the brightest point in each lobe to calculate the Fanaroff-Riley index, $\text{FR} = 2x_{\text{bright}}/x_{\text{length}} + 1/2$; in this formulation FR-Is should have indices $0.5 < \text{FR} < 1.5$ and FR-IIs should have $1.5 < \text{FR} < 2.5$ (Krause et al., 2012). The numerical values thus obtained are in excellent agreement with visual classifications. As Table 2.1 shows, all visually-identified FR-II lobes have FR indices well in excess of 1.5, with the exception of the southern lobe of RGZ J093821.5+554333, where the small lobe size and source curvature are likely to render lobe length measurement unreliable. For FR-Is, only the eastern lobe of RGZ J094443.2+024754 has an FR index marginally in excess of 1.5; it also has an unusual double-knot structure in the jet. We note that our approach of measuring lobe lengths is an approximation, and cannot deal with curved sources. Below, we restrict our analysis to straight, FR-II sources for which our methodology is valid. There is one hybrid source, RGZ J082835.2+322825 (Figure 2.2), with a clear FR-I morphology in the eastern lobe, and FR-II morphology in the western lobe.

Finally, the lobe luminosities of some of the FR-IIs in our sample may be contaminated by hotspot emission (as seen in Figures A.1-A.15), which is unaccounted for in analytical radio source models. Hotspots are typically $\lesssim 1$ percent of source size (Hardcastle et al., 1998; Godfrey & Shabala, 2013), and hence sources with total length shorter than ~ 200 arcsec are likely to contain both lobe and hotspot emission at the peak brightness location. In Table 2.1, we quote the fraction of the total lobe flux density contained in hotspots. The integrated flux
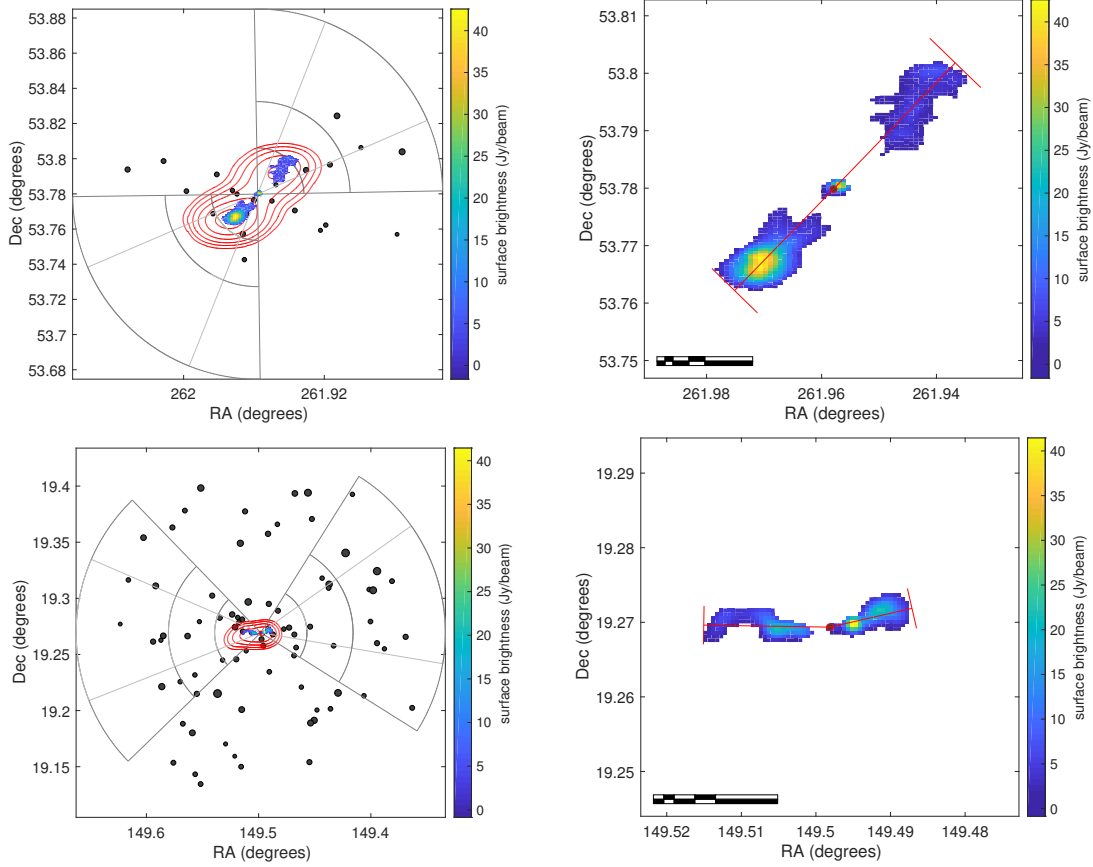
Figure 2.1: *Top left:* Radio-optical overlays for the FR-II source RGZ J172749.5+534647. Colour scale shows 1.4 GHz FIRST surface brightness, red contours are 1.4 GHz NVSS surface brightness. Black circles are optical galaxies with redshifts consistent with the radio source host; symbol size is proportional to *z*-band magnitude of each galaxy. Wedges of 45 and 90 degrees centered on the lobe axis are shown, with arcs drawn at 250, 500 and 1000 kpc from the AGN host. *Top right:* Zoom-in on the radio emission; the scale bar is one arcminute in length, and subdivided into units of 5, 10, 20 and 30 arcminutes. Red lines are indicative of axis lengths and jet directions; cross-bars at the end are the width of the fitted box. Green contours mark the 5σ level in 1.4 GHz FIRST surface brightness. Black-and-white scale bar marks 5, 10, and 30 kpc. *Bottom:* FR-I source RGZ J095759.3+191609; symbols are as above. Radio-optical overlays for the remaining FR-II and FR-I sources can be found in Appendix A and Appendix B respectively.

			Galaxy and cluster environment				Eastern lobe										Western lobe									
RGZ Name	z	d_L [Mpc]	M_r	$N_{1\,Mpc}$ ($m_z>20.5$)	d_5 [kpc]	d_{10} [kpc]	D [arcsec] 5σ	D [arcsec] 3σ	$S_{1.4}$ [mJy] 5σ	$S_{1.4}$ [mJy] 3σ	Hotspot fraction	FR	$N_{500\,kpc}$ $45°$	$N_{500\,kpc}$ $90°$	$N_{1\,Mpc}$ $45°$	$N_{1\,Mpc}$ $90°$	D [arcsec] 5σ	D [arcsec] 3σ	$S_{1.4}$ [mJy] 5σ	$S_{1.4}$ [mJy] 3σ	Hotspot fraction	FR	$N_{500\,kpc}$ $45°$	$N_{500\,kpc}$ $90°$	$N_{1\,Mpc}$ $45°$	$N_{1\,Mpc}$ $90°$
(1)	(2)	(3)	(4)	(5)	(6)	(7)	(8)	(9)	(10)	(11)	(12)	(13)	(14)	(15)	(16)	(17)	(18)	(19)	(20)	(21)	(22)	(23)	(24)	(25)	(26)	(27)
FR-IIs																										
RGZ J090542.6+465809	0.195†	960	-21.19	16	446	1023	61	62	112.0	121.9	0.23	2.17	0	2	1	6	81	81	88.4	99.2	0.30	2.31	1	3	1	5
RGZ J091445.5+413714	0.140	666	-23.86	14	154	240	54	55	269.7	274.0	0.13	1.98	0	3	4	8	42	42	219.7	224.0	0.16	2.09	6	8	10	14
RGZ J093821.5+554333	0.221	1105	-22.53	26	187	370	32	40	47.2	50.4	0.19	1.58	3	8	5	12	44	47	34.3	38.9	0.14	2.01	0	1	3	6
RGZ J100128.8+043437	0.222	1111	-23.29	37	351	484	53	54	27.7	30.1	0.19	2.11	1	9	2	12	40	41	34.9	37.8	0.22	2.15	3	8	6	15
RGZ J102040.8+315509	0.286	1482	-23.15	17	213	441	34	36	15.0	20.4	0.18	2.15	0	0	0	5	43	44	20.7	23.9	0.17	2.17	2	4	2	4
RGZ J110254.0+125904	0.140	666	-22.94	17	219	444	83	85	12.2	17.7	0.19	2.41	0	1	5	9	96	99	7.4	13.7	0.27	2.42	2	2	4	11
RGZ J120118.2+124500	0.278†	1435	-22.22	18	295	444	41	41	137.6	140.1	0.09	1.75	3	7	4	8	61	62	87.7	91.3	0.08	2.09	1	1	2	2
RGZ J125721.9+122820	0.208	1032	-22.43	13	196	431	40	41	86.0	92.2	0.11	2.13	0	1	0	8	44	46	174.2	180.7	0.31	2.17	0	1	2	5
RGZ J125724.2+063114	0.175	851	-21.91	12	480	586	35	36	20.1	26.0	0.18	1.80	1	3	7	10	50	52	9.1	16.6	0.29	2.02	2	4	2	6
RGZ J135110.8+072846	0.150	718	-22.67	9	270	380	51	51	105.4	115.5	0.23	1.98	3	6	3	6	44	45	90.5	98.3	0.24	2.15	5	6	5	9
RGZ J153008.0+231616	0.090	1482	-23.29	31	393	732	65	67	54.8	67.9	0.10	2.25	5	10	5	12	65	67	60.7	69.8	0.09	2.07	5	7	5	10
RGZ J154936.7+361417	0.236	1190	-23.01	14	334	597	44	48	6.5	10.5	0.29	2.25	2	4	2	4	42	43	11.7	18.0	0.21	2.27	1	4	3	4
RGZ J161037.5+060509	0.241	1219	-22.45	13	506	603	46	49	18.2	24.0	0.16	2.08	1	4	2	7	41	46	18.0	23.1	0.15	2.13	2	2	3	5
RGZ J172749.5+534647	0.244†	1236	-22.17	21	165	321	91	92	795.6	823.1	0.05	1.93	3	5	3	5	110	113	281.1	319.4	0.03	2.24	3	3	5	6
RGZ J172957.2+450623	0.255†	1230	-22.29	12	490	663	98	100	203.8	228.0	0.08	2.20	2	3	2	3	90	93	180.1	199.7	0.08	2.23	6	7	6	7
RGZ J210030.5+100529*	0.156†	750	-22.46	12	294	466	31	43	1.2	12.8	~1	2.32	0	1	0	1	39	42	11.0	19.0	0.44	2.16	1	2	5	7
Hybrids																										
RGZ J082835.2+322825	0.280	1447	-22.93	19	446	1023	32	35	9.1	15.1	0.48	1.25	1	3	2	4	35	37	9.0	11.9	0.40	2.24	2	7	2	7
FR-Is																										
RGZ J085549.1+420420	0.238	1202	-22.19	13	446	1023	68	70	30.6	48.4	0.05	1.56	1	1	3	4	61	67	40.2	50.9	0.05	1.55	3	4	3	4
RGZ J094443.2+024754	0.220	1099	-23.49	37	447	1024	77	80	72.7	79.9	0.16	1.66	4	6	7	11	64	67	98.8	104.7	0.24	1.50	2	5	3	6
RGZ J095759.3+032725	0.165	798	-23.57	32	448	1025	58	61	256.7	260.4	0.41	0.97	4	9	9	15	46	49	293.4	295.9	0.29	0.96	4	9	7	14
RGZ J095759.3+191609	0.088	405	-23.42	11	449	1026	62	62	130.0	133.4	0.17	1.36	6	13	6	23	41	41	158.5	162.2	0.26	0.96	6	9	16	22
RGZ J145001.5+144747	0.300	1566	-23.28	13	450	1027	34	35	29.1	31.0	0.28	1.48	0	3	0	3	31	33	33.1	35.3	0.34	1.17	2	2	2	2
RGZ J145039.8+441829	0.286	414	-23.04	1	451	1028	73	75	118.0	126.4	0.14	1.20	3	4	5	8	56	58	154.6	159.4	0.36	1.03	2	5	5	10

Table 2.1: The samples of FR-IIs, hybrids and FR-Is. Columns are: (1) source name; (2) redshift, where a dagger denotes only photometric available; (3) luminosity distance; (4) z-band absolute magnitude; (5) number of galaxies within 1 Mpc above $m_z = 20.5$ mag; (6) distance to fifth nearest neighbour; and (7) distance to tenth nearest neighbour. For the eastern / western radio lobes the columns are: (8/18, 9/19) lobe lengths for 5σ and 3σ flux density cuts, respectively; (10/20, 11/21) 1.4 GHz flux density from FIRST at the 5σ and 3σ cuts; (12/22) fraction of flux density in the hotspot; (13/23) Fanaroff-Riley morphology; (14/24, 15/25) number of galaxies within 500 kpc of the host and 45 or 90 degrees of the lobe axis; and (16/26, 17/27) same as the previous columns but for 1 Mpc. * Continuum emission in RGZ J210030.5+100529 is hotspot-dominated, and this source is excluded from analysis.

density in the eastern lobe of RGZ J210030.5+100529 (Figure A.15) arises almost entirely from unresolved (hotspot) emission, whilst 41% of the emission in the western lobe is attributed to the hotspot. We conclude that this source has substantial hotspot contamination, and exclude it from the analysis.

2.2.2 Galaxy clustering

In quantifying galaxy clustering associated with each lobe, we consider galaxies within a 1 Mpc radius and with redshifts consistent (to within 1σ, provided the fractional redshift error does not exceed 10%) with the AGN host. The rectangular boxes fitted to the lobes, as described in Section 2.2.1, are used to estimate the direction of jet propagation and shown in Figure 2.2 by the red line extending outwards from the host galaxy. We then define "wedges" around each lobe, mirrored about the expansion axis and subtending angles of 45 and 90 degrees; these are shown by dotted and solid grey lines in Figure 2.2. Neighbouring galaxies are assigned to a lobe if they are located within the appropriate wedge. By selecting in our sample only relatively straight pairs of lobes which are close to anti-parallel (to within approximately ten degrees), we ensure that all galaxies are associated with a maximum of only one lobe.

Our sample consists of both nearby and more distant ($z = 0.3$) AGN. SDSS is 95% complete at $m_z = 20.5$ mag, and we use this cut-off, converted to absolute magnitude, when calculating clustering associated with each lobe. This procedure allows us to compare environments of radio sources with different morphologies (Section 2.3). In Section 2.3.2, we consider the differences between two lobes of the same radio source. We quantify environment asymmetry by taking the ratio of total galaxy counts associated with each lobe, above the completeness limit (Figure 2.4). This is broadly equivalent to taking the ratio of the normalization in the stellar mass function of galaxies associated with each lobe: we repeated the analysis below using estimates of the total stellar mass (i.e. summed over all galaxies) associated with each wedge (calculated using z-band magnitudes), and found similar results.

2.2.3 Sample statistics

The aim of this paper is to investigate the relationship between asymmetries in radio lobe and environment properties. The left panel of Figure 2.5 shows the distribution of optical asymmetries, quantified as the logarithm of the ratio of galaxy counts above the limiting z-band magnitude of 20.5 within 1 Mpc in a 90-degree wedge associated with each lobe. Asymmetries in excess of 0.6 dex (i.e. a factor of 4) are observed for FR-II sources. The middle panel of Figure 2.5 shows a similar distribution for asymmetry in the radio continuum luminosity of each pair of lobes. Although FR-Is appear to show smaller asymmetries in both lobe continuum luminosity and galaxy counts, these differences are not statistically significant at the $p = 0.05$ level using the Wilcoxon-Mann-Whitney test. We note that although FR-Is are known to preferentially reside in more massive environments (Hill & Lilly, 1991; Sabater et al., 2013) than FR-IIs, our selection bias against highly curved and asymmetric sources such as wide-angle tailed or head-tail radio galaxies will be an important contributing factor – for example, overdense environments may preferentially produce bent sources. The right panel of Figure 2.5 shows the distribution
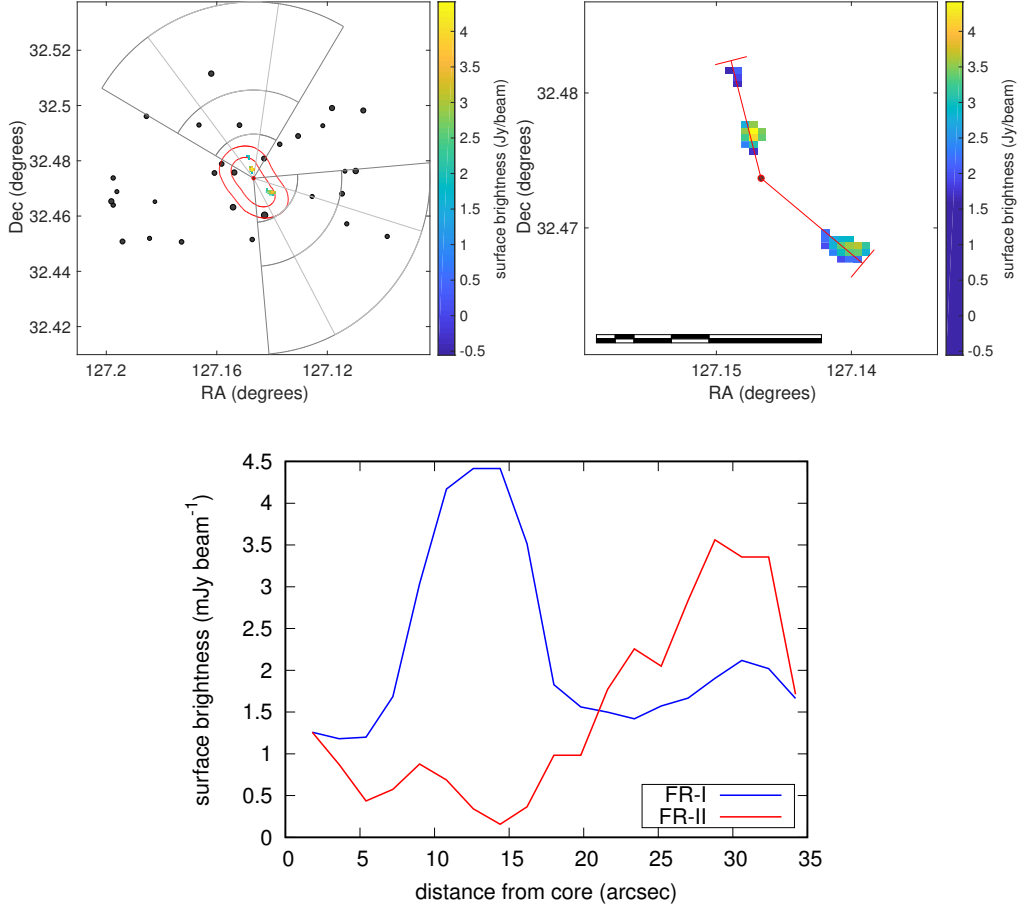
Figure 2.2: *Top:* Hybrid source RGZ J082835.2+322825; symbols are as in Figure 2.1. *Bottom:* The surface brightness profile along the lobe major axis of the hybrid source RGZ J082835.2+322825, measured from the active nucleus towards the extrema of each lobe. The profile of the eastern-most lobe (blue) is of characteristic FR-I type, whilst that of the western-most lobe (red) describes an FR-II.
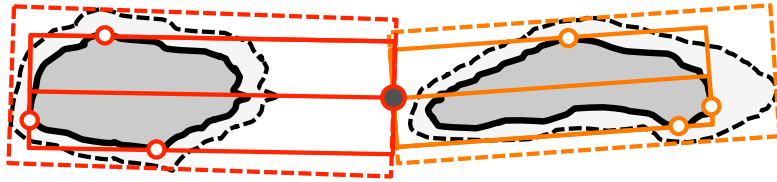
Figure 2.3: Defining the spatial extent of the radio lobes by the outermost 5σ (solid rectangles) for an FR-II type lobe (*left*) and an FR-I type lobe (*right*). Associated 3σ contours (dashed rectangles) are used to estimate the uncertainty of the spatial extent. Bounding rectangles are chosen such that (i) the active nucleus lies at the midpoint on the base of the rectangle (filled circle), and (ii) the remaining sides are tangent to the extrema of the lobe (open circles). Radio lobes with lobe axes differing by more than approximately ten degrees, or whose axes are not confined within the horizontal extent of the lobe (i.e. highly bent), are excluded from our analysis.
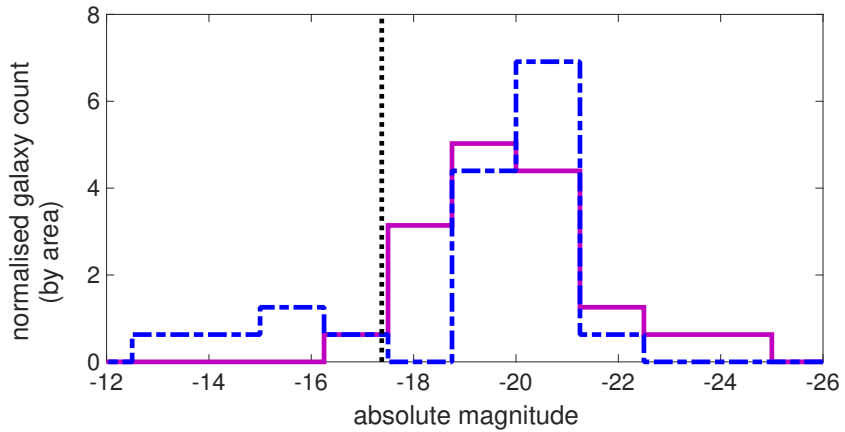
Figure 2.4: The distribution of absolute z-band magnitudes of galaxies surrounding FR-I source RGZ J095759.3+191609 (Figure B.3), normalised to the area of the containing 90 degree wedge. Purple corresponds to the western-most lobe, and the blue dot-dashed line to the eastern-most lobe. The black dotted line is the 95% completeness limit on the absolute z-band magnitude. Normalised galaxy counts are lower for galaxies less luminous than this limit, as expected.

of length asymmetries for the sources in our sample; again, we find no statistically significant difference at the $p = 0.05$ level between the FR-I and FR-II samples.

In Section 2.3.2 we investigate the relationship between radio and optical asymmetry diagnostics for the FR-II sources in our sample. We note again that length and luminosity measurements of FR-I sources are strongly affected by surface brightness sensitivity of observations (Shabala et al., 2017; Turner et al., 2018a) and should be interpreted with caution; we do not consider the FR-I sample in detail further in this work.

2.3 The role of environment

2.3.1 The relationship between radio source and host galaxy properties

The 16 FR-IIs and 6 FR-Is in our sample have similar redshift distributions (identical at the $p = 0.05$ level, shown in Figure 2.6), and as such we can confidently compare the typical environments inhabited by the two morphological classes. Figure 2.7, taken after Owen & Ledlow (1994), shows the relationship between lobe luminosity and host galaxy optical magnitude. We recover the previously found result that FR-Is are hosted by more massive galaxies (i.e. optically brighter) than FR-IIs, albeit at only at a 2σ confidence level, most likely due to the small FR-I sample size. There is however no clear separation between FR-I and FR-II sources in this plot, consistent with the results of Best (2009) who similarly used a redshift-matched sample.

Figure 2.8 probes the large-scale (out to 1 Mpc) environment of the radio sources in our sample, quantified via counts of galaxies with $M_z < -20.47$ mag (corresponding to $m_z = 20.5$ mag at $z = 0.3$, our highest redshift). Perhaps surprisingly, FR-Is do not appear to inhabit denser environments as has been reported by several authors previously (e.g. Miraghaei & Best, 2017; Sabater et al., 2013). This is again likely due to our selection effect against compact radio sources, which dominate number counts in dense environments (Shabala et al., 2008). Conversely, this result shows that the large-scale environment is not a crucial factor in the determination of the radio lobe morphology; the FR-I morphology is likely determined much closer to the active nucleus.

2.3.2 FR-II sources

Theoretical considerations

Dynamical models of double-lobed radio sources make clear predictions for the relationship between FR-II size and radio continuum luminosity, and environment properties. For a classical FR-II expanding into a power-law atmosphere of the form $\rho(r) = \rho_0 \left(r/r_0\right)^{-\beta}$, Equations 1 and 4 of Shabala & Godfrey (2013) give the scalings between source linear size D, continuum
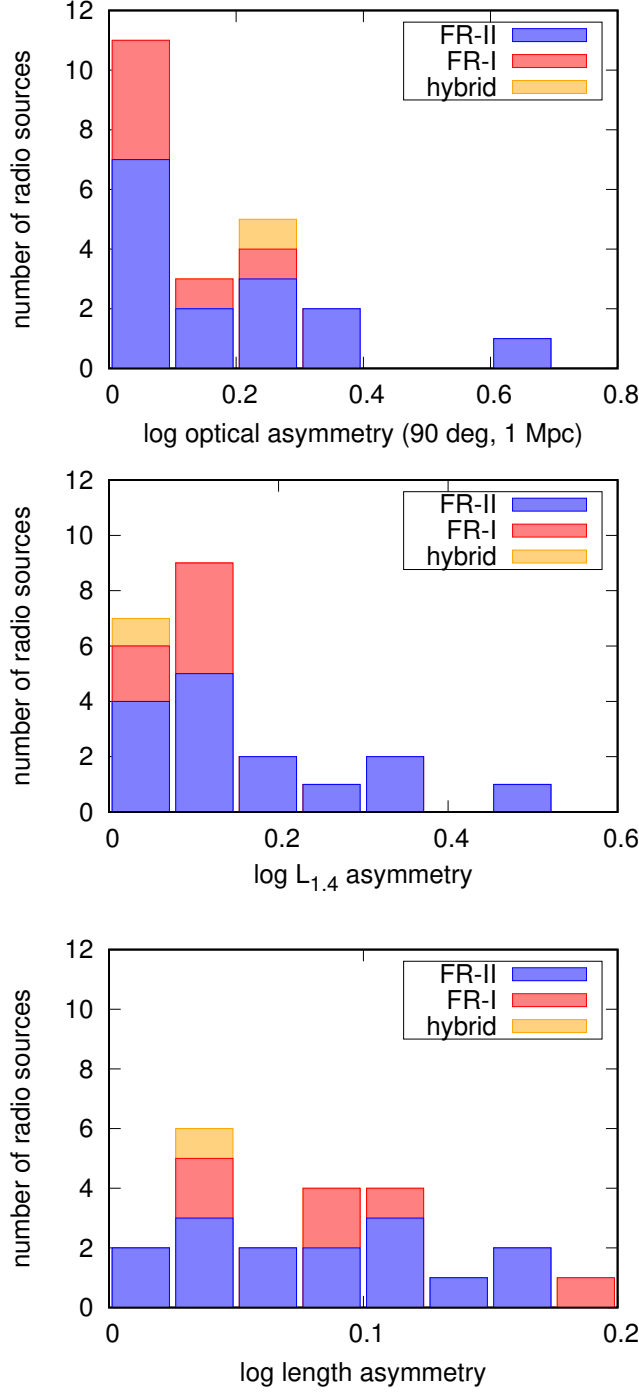
Figure 2.5: Distribution of asymmetries in radio source properties for FR-II (blue), FR-I (red), and Hybrid (brown) sources, shown as stacked bars. *Top*: Distribution of asymmetry in galaxy clustering associated with each lobe, defined as the log ratio of the number counts of galaxies brighter than 20.5 mag in SDSS *z*-band, located within a 90 degree wedge of 1 Mpc radius centred on the host galaxy. *Middle*: Asymmetry in 1.4 GHz FIRST radio luminosity, integrated out to 5σ for each lobe. *Bottom*: Asymmetry in lobe lengths which are defined by the bounding rectangle described in Section 2.2.1 and Figure 2.3.
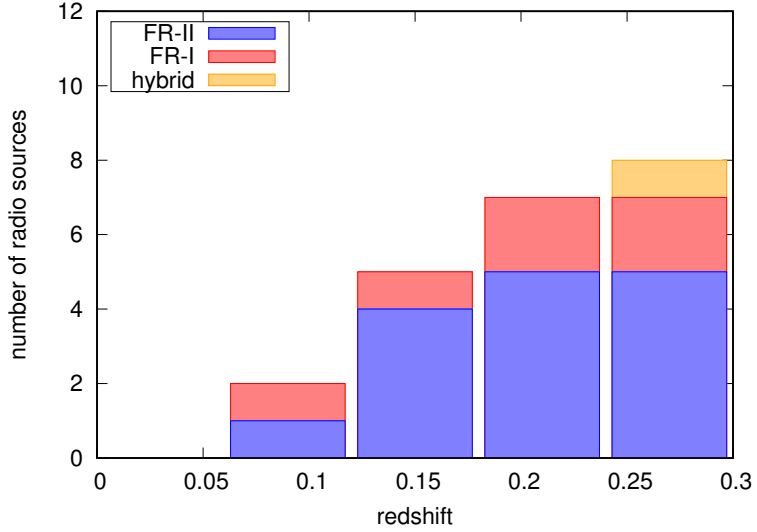
Figure 2.6: The distribution in redshift for sources out to the redshift limit $z = 0.3$, shown as stacked bars. Colours are as in Figure 2.5.
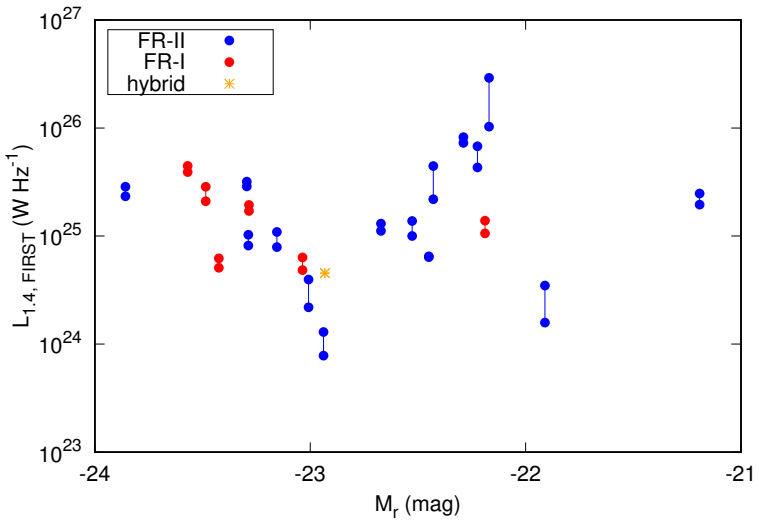
Figure 2.7: The host galaxy optical absolute r-band magnitude versus lobe luminosity for each source, known as the Ledlow-Owen relation, taken after Owen & Ledlow (1994). Each lobe is represented by a single point, with lobe pairs corresponding to a single source connected via a solid line. No clear separation of the classes is seen. Colours are as in Figure 2.5.
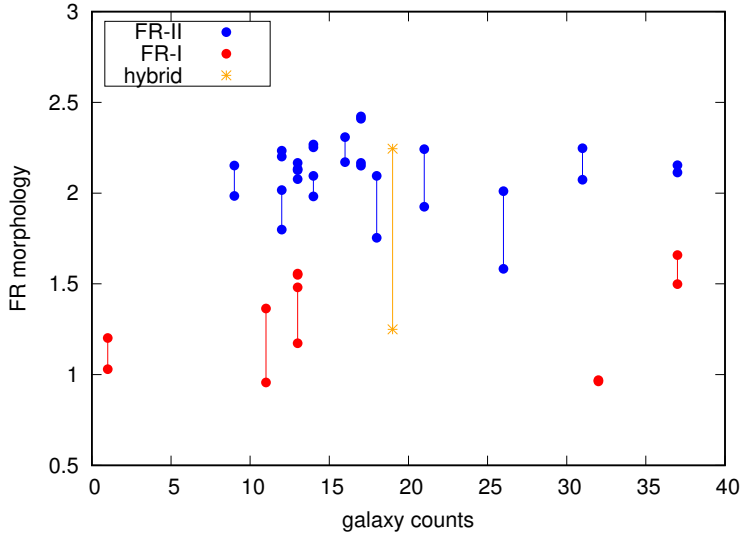
Figure 2.8: The complete ($m_z > 20.5$ mag) SDSS galaxy counts within 1 Mpc of the active nucleus as a function of FR index. Consideration of the large-scale environment does not provide a clear distinction between the morphologies in this sample. Colours are as in Figure 2.5.

luminosity L_ν and atmosphere gas density ρ_0,

$$D \propto \rho_0^{-\left(\frac{1}{5-\beta}\right)}$$
$$L_\nu \propto \rho_0^{\frac{5+s}{12}} D^{3-\left(\frac{4+\beta}{3}\right)\left(\frac{5+s}{4}\right)} \tag{2.1}$$

where $s = 2 - 2.5$ is the power-law index of the electron energy distribution at the hotspot (Kaiser et al., 1997; Willott et al., 1999; Turner et al., 2018b).

Assuming typical β values between 0 and 2, the expected scalings are $D \propto \rho_0^{[-0.33,-0.2]}$, $L_\nu \propto D^{[-2.63,-2.25]}$, and $L_\nu \propto \rho_0^{[-0.13,+1.25]}$. The luminosity calculation above assumes no electron ageing, and a direct mapping between radio lobe pressure and continuum luminosity. In practice, factors such as spectral ageing (Murgia, 2003; Turner, 2018), non-equipartition magnetic fields (Croston & Hardcastle, 2014), magnetic field inhomogeneities (Hardcastle, 2013) and particle re-acceleration (Jones et al., 1999) will introduce significant scatter in the luminosity relations, and we therefore expect the size–density relation to be the tightest.

Dependence on the large-scale environment

Figure 2.9 shows the relationship between lobe length asymmetry and galaxy clustering. Both quantities are calculated by taking the ratio of the relevant quantity (length, or galaxy counts above the completeness limit) of the eastern lobe divided by the western lobe. Environment asymmetry is calculated for both 500 kpc and 1 Mpc radii from the AGN host, and using galaxies within 45 and 90 degree wedges centred on the lobe axis. Uncertainty in lobe length ratio
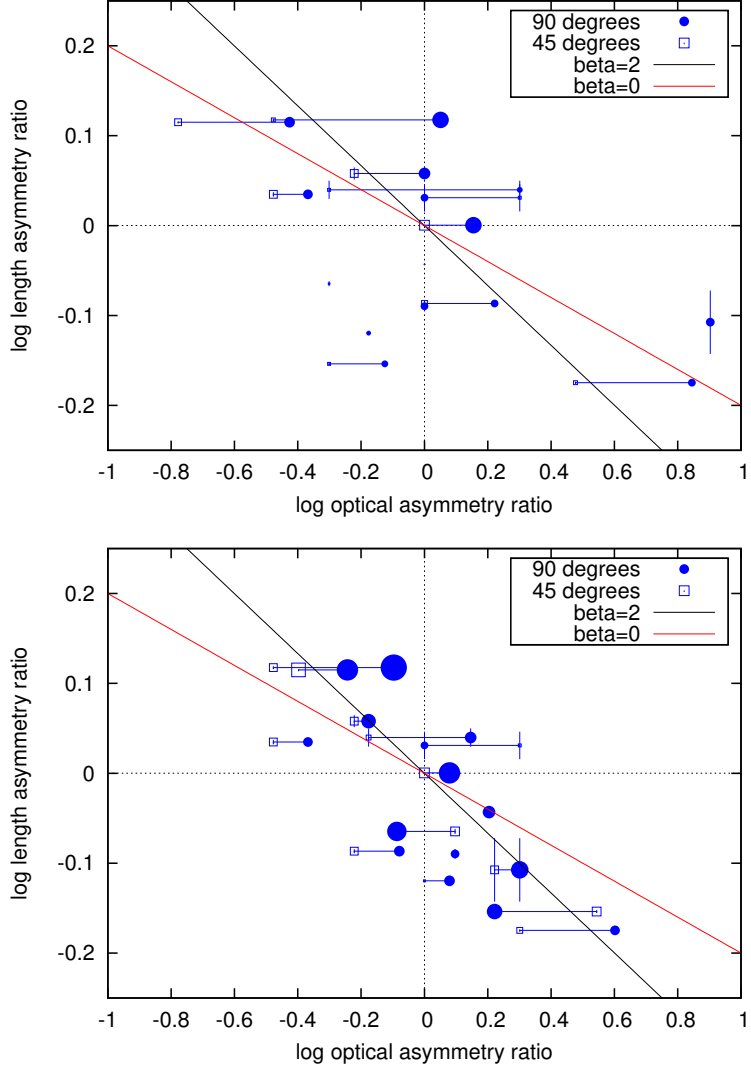
Figure 2.9: Asymmetry in FR-II lobe length and environment. Symbol size is proportional to the total number of galaxies used in the environment asymmetry calculation, i.e. larger points correspond to higher galaxy counts. Environment asymmetry is quantified using galaxies with photometric redshift consistent with the AGN host, within either 500 kpc (*top*) or 1 Mpc (*bottom*) radius from the host galaxy. Model predictions correspond to a flat ($\beta = 0$) density profile typical of inner (~ 30 kpc) regions of clusters; and steep ($\beta = 0$) environments more representative of large (>100 kpc) clustercentric radii.
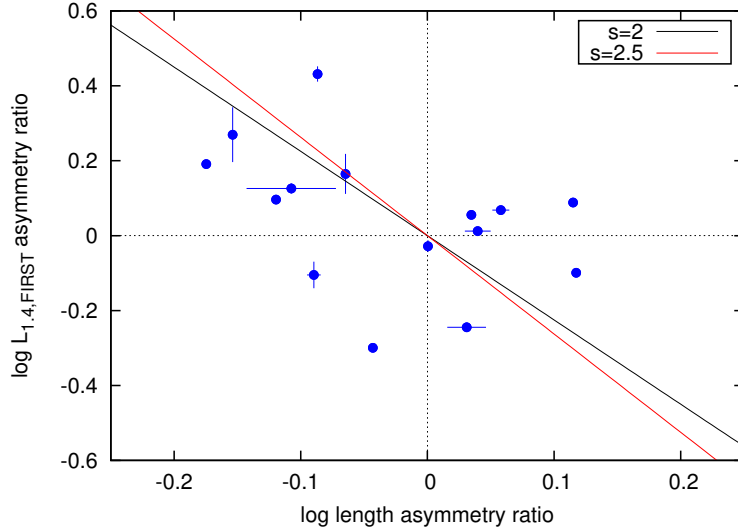
Figure 2.10: Lobe luminosity and length asymmetry for FR-II sources. Symbols are as in Figure 2.9.

is estimated by calculation of this quantity for two cuts in the signal-to-noise ratio, at 5σ and 3σ respectively; length measurements of prominent FR-II lobes are not expected to vary substantially with the adopted noise cut. Regardless of the environment metric, there is a consistent, clear anti-correlation between these two quantities as indicated by a deficit of sources in the top right and bottom left corners of the plot. Moreover, the slope of the observed relation ($D \propto \rho_0^{-0.29\pm0.07}$, a non-zero slope at the 4σ level for the 500 kpc, 90 degree case) is consistent with expectation from analytical models if the galaxy clustering traces the underlying gas density profile, shown as solid lines for steep (black) and flat (red) gas density profiles. The best-fit relationship suggests the typical radio source in the sample expands into a host environment with a pressure profile falling off with radius as $\rho_0 \propto r^{-1.6}$, representative of gas distribution at large cluster-centric radii.

The simplest analytical models of the kind described in Section 2.3.2 assume that radio lobes evolve self-similarly over their lifetime. This assumption is inconsistent with the observed increase in the radio source aspect ratio with length (Hardcastle et al., 1998; Turner et al., 2018b), which is also predicted by more realistic analytical models (Turner & Shabala, 2015) and numerical simulations (Hardcastle & Krause, 2013). Recent numerical simulation work (Vandorou et al., in prep.) shows that relaxing the self-similarity assumption can explain much of the observed scatter in the length–environment asymmetry relation shown in Figure 2.9.

Figure 2.10 shows the observed relationship between asymmetry in lobe length and luminosity. Definition of which emission belongs to the lobe is important: taking a higher threshold in the signal-to-noise ratio will systematically affect the lobe luminosity ratio by preferentially resolving out emission from the lower surface brightness lobe. Following our approach for lobe length measurement, the uncertainty in lobe luminosity ratio is again calculated by considering the difference in this quantity for signal-to-noise ratios of 3 and 5σ. Both the approximate anti-
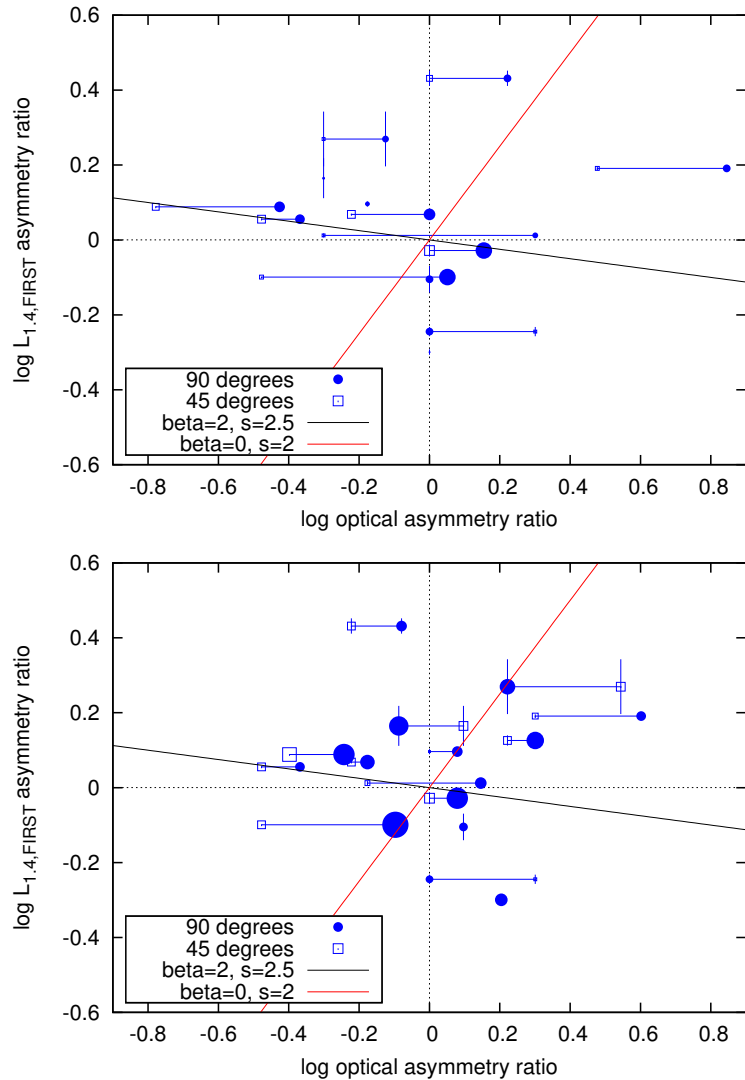
Figure 2.11: Asymmetry in FR-II lobe luminosity and environment. Panels and symbols are as in Figure 2.9.

correlation of $L_\nu \propto D^{-3.9\pm1.9}$ (non-zero slope at the 2σ level) and large scatter in Figure 2.10 are qualitatively consistent with the expectation from models. Idealized model predictions in Figure 2.10 are only indicative as they do not take into account electron ageing, which will be significant for the large (and hence old) radio galaxies in our sample. The complex luminosity evolution of individual radio sources (by over an order of magnitude, and strongly environment-dependent; Hardcastle & Krause, 2013) will significantly contribute to the scatter in these relations; for example, using FR-II samples carefully matched in jet power and source size, Shabala & Godfrey (2013) showed that environment can contribute approximately 0.3 dex to scatter in radio luminosity. We defer a detailed discussion of these points to future work.

Finally, we plot the relationship between lobe luminosity asymmetry ratio and environment in Figure 2.11. Unlike lobe length, which increases monotonically with age, lobe luminosity is predicted to vary non-monotonically over a radio source lifetime; hence the lobe luminosity asymmetry ratio will depend on source age in addition to jet and environment properties (Hardcastle & Krause, 2013; Shabala, 2018). The lack of any correlation at above the 2σ level in Figure 2.11 is expected from the wide range of factors which influence the lobe luminosity, as demonstrated by the broad range of predictions from analytical models (solid lines).

2.3.3   FR-I and hybrid sources

There are only six FR-I sources in our sample, hence we are unable to perform a similar analysis for these objects. From Table 2.1 there appears to be no obvious relationship between length or luminosity asymmetry and environment for FR-I sources, in broad agreement with complex expectations from the models. Jets are theoretically expected to propagate slower in denser environments (Kaiser et al., 1997), however such environments may also be more conducive to keeping the jets collimated (Krause et al., 2012), allowing them to propagate further. Environmental boosting (Arnaud et al., 2010) is also likely to increase the jet surface brightness (and luminosity), enabling those jets propagating into denser gas to be visible to larger distances from the host galaxy (Shabala et al., 2017; Turner et al., 2018a). Given these competing effects and the small size of our sample, we are unable to draw any meaningful conclusions about the FR-I population.

A single hybrid radio source (RGZ J082835.2+322825) is present in our sample, and is shown in Figure 2.2. The SW lobe shows a clear FR-II morphology, while the northern lobe appears to have a bright flare point followed by a gradual decrease in surface brightness. The FR indices are 2.24 and 1.25 respectively, consistent with the visual classification of this source as a hybrid. Small number statistics make environmental analysis difficult: there are 4 galaxies in a 90-degree wedge within 1 Mpc of the AGN host on the FR-I side, and 7 galaxies on the FR-II side, reducing to only 2 galaxies on each side for a 45-degree wedge; we refrain from speculating on the causes of this source's morphology.

2.4   Conclusions

We have presented a sample of extended radio AGN identified as part of the Radio Galaxy Zoo citizen science project. Our sample consists of 16 FR-II objects, 6 FR-Is and one hybrid morphology radio source. The environments into which these objects expand have been quantified using optical photometry from SDSS, to investigate the effect that the large-scale environment has on the size and luminosity evolution of radio sources. Small sample numbers preclude us from drawing any meaningful conclusions about the FR-I and hybrid populations.

For the FR-II sources, we find that:

- The length of an FR-II radio lobe is strongly negatively correlated (statistically significant at the 4σ level) with the number density of galaxies in the environment into which it expands; this relationship is consistent with analytical models (e.g. Kaiser & Alexander, 1997; Turner & Shabala, 2015).

- Luminosity ratio of FR-II lobes is moderately (statistically significant at the 2σ level) negatively correlated with the lobe length ratio, again consistent with analytical models.

- There is no clear correlation between the asymmetry in luminosity of FR-II lobes and the number density of galaxies in their vicinity; the large observed scatter is consistent with the sensitivity of this relation to changes in the environment density profile and lobe electron energy distribution.

The excellent agreement between data and predictions from analytical models suggests that galaxy clustering provides a useful measure of the radio lobe environment. In the coming years, a combination of radio source models (e.g. Turner & Shabala, 2015; Hardcastle, 2018) and large-area radio continuum surveys supplemented by galaxy clustering information, such as the GAMA Legacy ATCA Southern Survey (GLASS), the Evolutionary Map of the Universe (EMU; Norris et al., 2011), and the LoFAR Two-metre Sky Survey (LoTSS; Shimwell et al., 2016), will enable a detailed census of the physical properties of radio AGN populations.

CHAPTER 3

Existing models for embedded radio sources

Within Chapter 2, the role of environment in radio source morphological evolution was demonstrated by analysis of a sample of FRII sources. Within this chapter, a number of models for radio sources and extragalactic environments are adapted from the literature so that Faraday Rotation may be investigated as an additional method of study for such systems. Galaxy clusters and groups with halo dark matter masses of $M_{200} = 10^{12}$, 10^{13}, and $10^{14} M_\odot$ are then simulated for increasingly complicated distributions for magnetic field strength $\underline{\boldsymbol{B}}$ and thermal electron number density n_e, and for sources angled at $0°$, $30°$, and $45°$ to the plane of the sky.

Section 3.1 outlines the physical dependencies of Faraday Rotation that must be modelled, with these parameters explored in Section 3.2 for the environment and radio source, along with a consideration of the source position and lobe shape, and with the construction of virtual observing beams, which may further impact on observed parameters, in Subsection 3.2.3. In Section 3.3, some possible variations of these models are explored. Cases not shown within this chapter can be found in Appendix C.

3.1 Faraday Rotation

Given that the Rotation Measure (RM) of polarised AGN emission (Burn, 1966, see Chapter 1 for details),

$$RM = 812 \int_0^s \left[\frac{n_\mathrm{e}}{\mathrm{cm}^{-3}} \right] \left[\frac{\underline{\boldsymbol{B}}}{\mu\mathrm{G}} \right] \cdot \left[\frac{d\underline{\boldsymbol{s}}}{\mathrm{kpc}} \right], \tag{3.1}$$

is dependent on the electron number density n_e and magnetic field strength $\underline{\boldsymbol{B}}$ (along the line of sight $d\underline{\boldsymbol{s}}$), these two parameters must be carefully modelled. Any line of sight between an observer here on Earth and an extended radio source will pass through both the intervening

medium and some internal part of the radio source structure. As will be shown throughout this Chapter, the distributions of n_e and $\underline{\boldsymbol{B}}$ are dissimilar within the lobes of a radio source and the external medium, and for this reason, are modelled separately in these different environments. Within this work, the galaxy cluster and its embedded radio source are assumed to be located at a redshift $z = 0$, and so properties within the intergalactic and interstellar media are not explored.

3.2 Theoretical considerations

3.2.1 Environment properties

The intracluster environment is modelled as a sphere of gas with a virial radius (Gunn & Gott, 1972):

$$r_{\text{vir}} = \left(\frac{3}{4\pi} \frac{M_{\text{vir}}}{\Delta_c \rho_{\text{crit}}} \right)^{1/3}, \tag{3.2}$$

for enclosed halo mass M_{vir}. Δ_c is the mean overdensity of the material, which is Δ_c times the critical density ρ_{crit} for a spherical collapse of gas:

$$\rho_{\text{crit}} = \frac{3H^2(z)}{8\pi G}, \tag{3.3}$$

where G is the gravitational constant and $H(z)$ is the Hubble parameter for redshift z:

$$H^2(z) = H_0^2 \left[\Omega_r (1+z)^4 + \Omega_m (1+z)^3 + (1 - \Omega_{\text{tot}})(1+z)^2 + \Omega_\Lambda \right]. \tag{3.4}$$

Here, H_0 is the Hubble constant and Ω_x are the various density parameters for radiation (r), matter (m), and dark energy (Λ), which sum to $\Omega_{\text{tot}} = 1$ by construction. Within an Einstein – de Sitter (EdS) universe, $\Delta_c = 18\pi^2 = 178$ (Rubin & Loeb, 2013). This parameter will vary over $\sim 100 - 500$ depending on cosmology and the gas density profile assumed, but is typically taken to be $\Delta_c = 200$ (White, 2001), which is the value adopted for this work. Under this convention, the virial mass and radius are denoted M_{200} and r_{200} respectively.

Three different environments are simulated with $M_{200} = 10^{12}, 10^{13},$ and $10^{14} M_\odot$ (Figure 3.1), corresponding to a small group, a large group, and cluster of galaxies, and associated with virial radii of $r_{200} \sim 206, 444,$ and 958 kpc respectively. For simplicity, these environments will be collectively referred to as clusters hereafter.

Simulations of these clusters are contained within a cube of 250^3 computational cells, with each cell representing a physical length of 8 kpc. Density and magnetic field values are generated within a sphere of radius $R = 1$ Mpc within this cube; the outer boundary is motivated by the virial radius of the most massive halo at ~ 958 kpc (Figure 3.2).

Density distribution

The thermal electron number density within the galaxy cluster is typically derived from X-ray observations (e.g. Cavaliere & Fusco-Femiano, 1976, and references therein), with the most
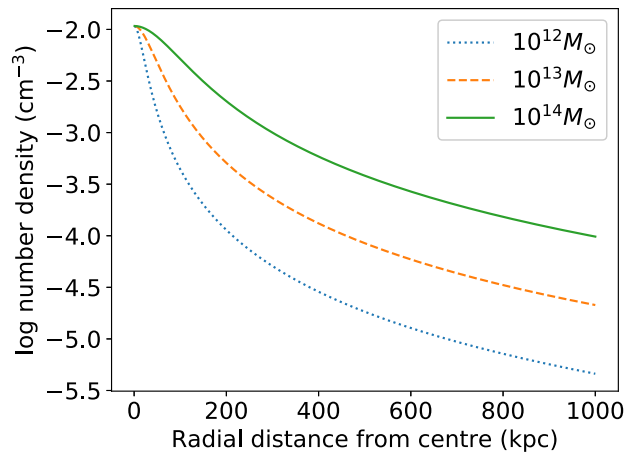
Figure 3.1: Variation in the intracluster density profile for different dark matter halo masses. The solid line corresponds to the cluster of $M_{200} = 10^{14} \ M_{\odot}$, the dashed line to $10^{13} \ M_{\odot}$, and the dotted line to $10^{12} \ M_{\odot}$.
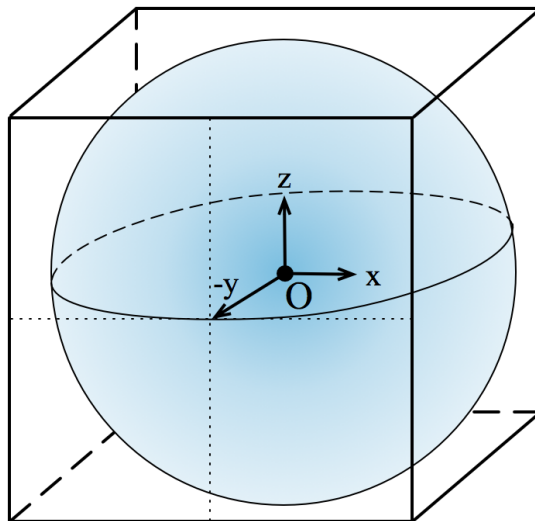
Figure 3.2: The coördinate system of the spherical gas cloud.
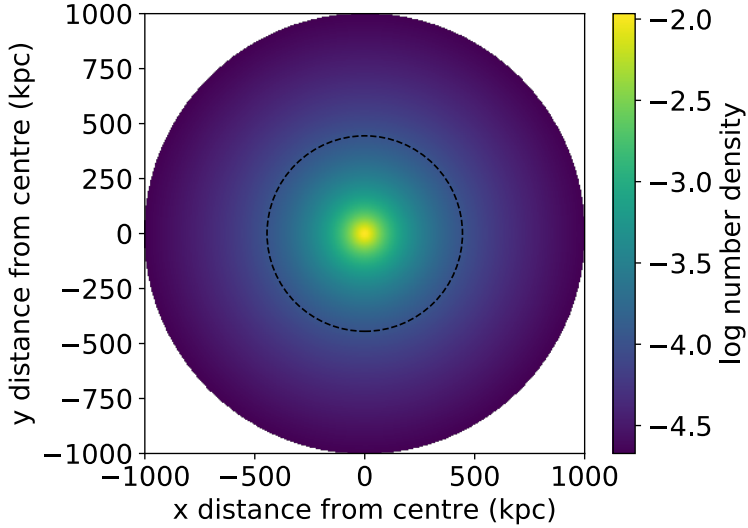
Figure 3.3: The thermal electron number density of the $M_{200} = 10^{13} M_\odot$ cluster taken at $z = 0$ and sliced through the mid-plane, governed by the modified King model (Equation 3.6). The black dashed line shows the virial radius for this dark matter halo mass, $r_{200} \sim 444$ kpc.

common fit described by a radial power law. An initial attempt at determining this function was made on the Coma cluster by Rood et al. (1972) and King (1972), whose data was well-approximated by what is now known as the King model:

$$n_{\mathrm{e}}(r) = n_0 \left(1 + \frac{r^2}{r_c^2} \right)^{-1}. \tag{3.5}$$

A general form of this model simply allows for variation in the fit by a parameter β, and is known as the *modified King model*:

$$n_{\mathrm{e}}(r) = n_0 \left(1 + \frac{r^2}{r_c^2} \right)^{-3\beta/2}, \tag{3.6}$$

where n_0 is the central thermal electron density, r_c is the core radius of the density profile, and r is the distance from the cluster centre to a particular cell ($r^2 = x^2 + y^2 + z^2$). Typical values which are adopted for these parameters are $n_0 \sim 0.01$ cm^{-3} (Cavaliere & Fusco-Femiano, 1976), $r_c \sim 0.1 r_{200}$ (Vikhlinin et al., 2006), and $\beta = 3/2$ (Carilli & Taylor, 2002), producing the thermal electron density distribution of Figure 3.3.

Magnetic field structure

Following the method laid out by Huarte-Espinosa et al. (2011b) (see also Tribble, 1991; Murgia et al., 2004), the magnetic field structure of the cluster gas is defined by a vector potential $\tilde{\underline{A}}(\underline{k})$ in Fourier space of the form:

$$\tilde{\underline{A}}(\underline{k}) = \underline{A}(\underline{k}) \exp\left(i\underline{\theta}(\underline{k})\right), \tag{3.7}$$

with wavenumber, amplitude, and phase vectors of $\underline{k}$, $\underline{A}$, and $\underline{\theta}$ respectively, where wavenumbers are taken to be the inverse of the distance from the cluster centre for each grid point. At each grid point, the amplitude and phase of $\underline{A}(\underline{k})$ are chosen from:

$$P(A, \theta)dAd\theta = \frac{1}{2\pi} \frac{A}{|A_k|^2} \exp\left(-\frac{A^2}{2|A_k|^2}\right) dAd\theta, \tag{3.8}$$

i.e. $\underline{\theta}$ is chosen from a uniform random distribution between 0 and 2π and $\underline{A}$ is sampled from a Rayleigh distribution. The Rayleigh distribution is a probability distribution for continuous, positive random variables x, of general form:

$$P(x; \sigma) = \frac{x}{\sigma^2} \exp\left(-\frac{x^2}{2\sigma^2}\right), \tag{3.9}$$

with scale parameter σ, which determines the statistical dispersion of the distribution.

For Equation 3.8, a scale factor of $\sigma = |A_k|^2$, where $|A_k|^2 \propto k^{-\zeta}$ ($k^2 = k_x^2 + k_y^2 + k_z^2$), is chosen as a power law ansatz of slope ζ. Huarte-Espinosa et al. (2011b) choose a Kolmogorov 3D turbulent slope of $n = 11/3$, which can be related to $|A_k|$ by $-\zeta = -n - 2$, and which is also used in this work.

The magnetic potential is found by multiplying the vector potential $\tilde{\underline{A}}(\underline{k})$ with wavenumber $\underline{k}$ in Fourier space and then taking the curl of this product. The potential field is mapped into real space by the inverse Fourier Transform resulting in the magnetic field $\underline{B}$ within the ICM. However the scale factor of the Rayleigh distribution, $|A_k|^2$, remains poorly constrained. The generated magnetic field must be normalised down to more physical values following the pressure and temperature values of the cluster.

Analysis of X-ray clusters (e.g. Vikhlinin et al., 2001a) shows discontinuities over a factor of $2 - 5$ in X-ray surface brightness in the direction of cloud motion, the increase in density in these regions being associated with a decrease in temperature which leaves the pressure relatively unchanged over the discontinuity. In order to maintain the approximately constant temperature profile within the cluster (Arnaud et al., 2001), thermal conduction must be suppressed, otherwise cooler structures on ~ 100 kpc scales will be evaporated via these discontinuities on timescales of ~ 10 Myr (Carilli & Taylor, 2002). Magnetic fields can allow for the suppression of thermal conduction and Kevin-Helmholtz mixing along the boundaries of hot and cold regions if the magnetic tension of the gas is high enough. Using Chandra data on cluster A3667, Vikhlinin et al. (2001a) propose a model in which the magnetic field is sheared along these
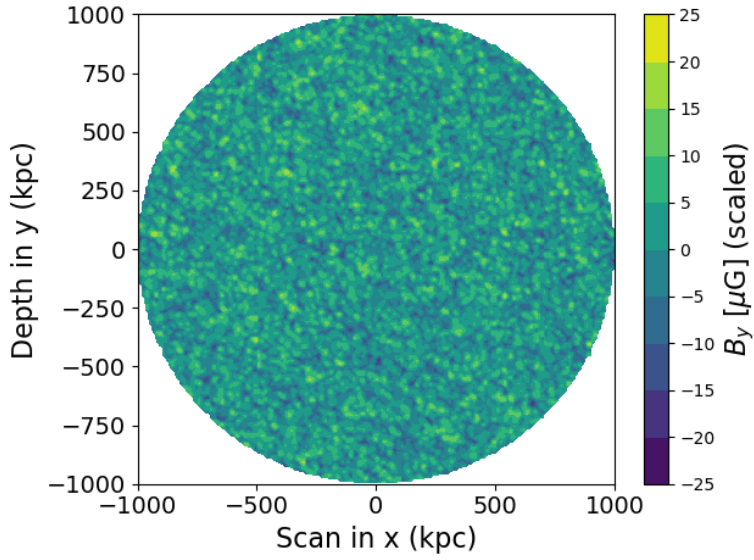
Figure 3.4: The resultant cluster magnetic field (viewed along a slice at the midplane) generated by the potential 3.7 for the large group ($M_{200} = 10^{13} M_{\odot}$), and scaled such that the magnetic pressure is $\sim 10\%$ of the thermal pressure in the cluster.

boundaries via fluid motions. In order to generate sufficient magnetic tension, this implies that the magnetic pressure p_B is between $10 - 20\%$ of the thermal pressure p_T. This yields a magnetic field strength along the discontinuity between $7 - 16 \, \mu$G (Vikhlinin et al., 2001a), however the unperturbed cluster field is likely a factor of a few lower at $1 - 10 \, \mu$G, the exact scaling factor being uncertain (Carilli & Taylor, 2002; Vikhlinin et al., 2001b).

Here, the scaling of mean cluster magnetic field to ICM pressure is taken as $\beta_m = p_T/p_B \sim 10$ everywhere within the cluster (Huarte-Espinosa et al., 2011b), giving:

$$\langle \underline{B} \rangle \sim \sqrt{\frac{2n_{\mathrm{e}} k_{\mathrm{B}} T \mu_0}{\beta_m}}, \tag{3.10}$$

for n_{e}, the thermal electron number density from Equation 3.6, $T \sim 10^7$ K, the approximate and assumed constant temperature of the galaxy cluster, and Boltzmann constant k_{B}.

3.2.2 Radio Source properties

The radio source is modelled with the central engine coincident with the cluster centre. The lobes are assumed to be ellipsoidal, with their surface described by:

$$\frac{x^2}{a^2} + \frac{y^2}{b^2} + \frac{z^2}{c^2} = 1, \tag{3.11}$$
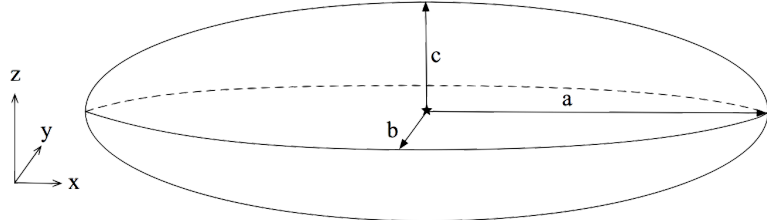
Figure 3.5: The ellipsoid model of the radio source.
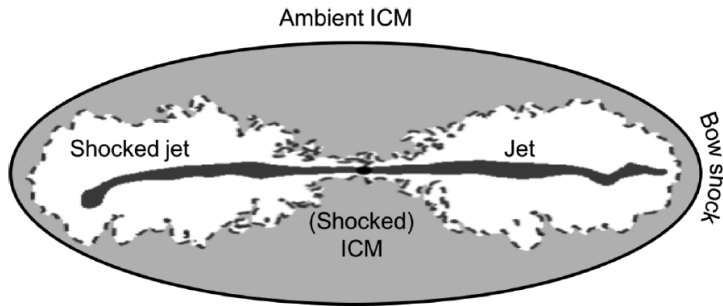
Figure 3.6: The two separate regions within the radio source – the jet and lobe (here, the "shocked jet") – and the outer cocoon of ICM material. Adapted from Bourne & Sijacki (2017).

for axis lengths of a, b, and c ($a > b, c$) in the x-, y-, and z-directions respectively. When embedded at the centre of the cluster environment, the combination of environment and radio source forms *the system*, with the radio source viewed as in Figure 3.5. Circular symmetry is assumed around the major axis, hence $b = c$.

Lobes can also be angled with respect to the observer. Due to the added spherical symmetry of the environment being simulated, it is only necessary to consider radio source orientations in a single plane. For this work the radio source may be rotated $0°$, $30°$, or $45°$ from the plane of the sky, corresponding to a rotation in the xy-plane. Rotations in all other planes may be recovered by a rotation of the system as a whole. The orientation of the radio source is designated by θ and is measured anticlockwise from the positive x-axis in the xy-plane.

Motivated by the simulations of Huarte-Espinosa et al. (2011b) and Bourne & Sijacki (2017), the radio source is separated into two components: an inner jet and surrounding back-flow, hereafter the *jet* (j) and *lobe* (l). In addition, an intermediate region (the *cocoon*, c) is defined marking the transition from radio source material to the ambient ICM (Figure 3.6). This region has a density identical to that of the ambient cluster environment, but the magnetic field may either be disordered as in the ICM, or ordered as in the lobe (Section 3.2.2). The level of order is described by a parameter $f \in [0, 1]$, with $f = 0$ corresponding to the ICM field distribution and $f = 1$ corresponding to the field distribution of the lobe.
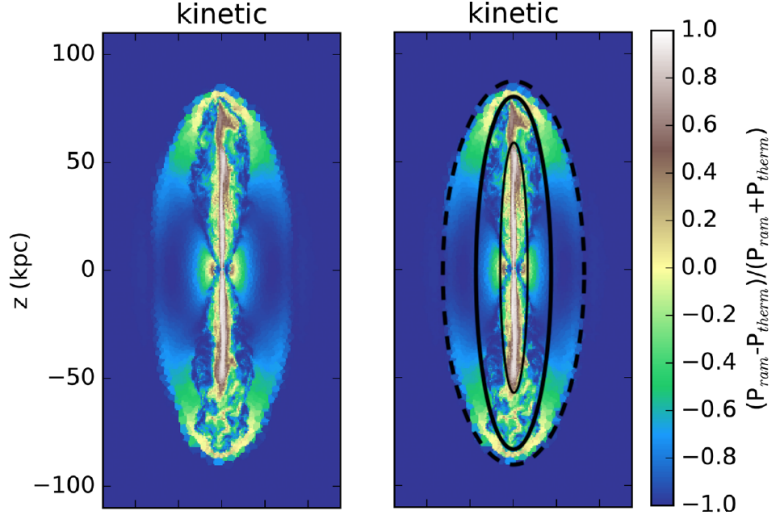
Figure 3.7: The "kinetic" jet simulation of Bourne & Sijacki (2017) (*left*), and with equivalent ellipsoidal overlays (*right*) corresponding to the jet and lobe (inner solid ellipses), and the cocoon material (dashed ellipse).

Rough estimates of the axial ratios, $\alpha = D/w$ for total source length D and width w, for the lobe and cocoon regions are obtained from Bourne & Sijacki (2017) (Figure 3.7):

$$\alpha_l \sim 4.6 \tag{3.12}$$

$$\alpha_c \sim 2.7, \tag{3.13}$$

where the envelope of the cocoon is $\sim 10\%$ longer than that of the lobe. The inner jet is also modelled by an ellipsoid fitted to its length, which is assumed to be $\sim 30\%$ shorter than that of the lobe and self-similar (i.e $\alpha_l = \alpha_j$). Throughout this work, radio lobes are assumed to be symmetric FRIIs with total source shape that is highly regular and ellipsoidal, making the assumption of self-similarity a reasonable one. Under conditions with particularly young or old, irregular, or restarted FRIIs, or for sources with alternate morphologies such as FRIs and HyMoRS, these conditions will break down.

Density distribution

The thermal electron number density within the jet and lobe is assumed to be significantly lower than that of the surrounding environment for a relatively fast-moving jet with Lorentz factor $\Gamma_j \sim 2$, related to the central group/cluster density n_0 by

$$n_j = \eta n_0 \tag{3.14}$$

for fraction $\eta \sim 10^{-4}$ (Krause, 2005) and cluster core density $n_0 = 0.01$ cm^{-3} (Cavaliere & Fusco-Femiano, 1976). As described above, the cocoon assumes the density of the ambient ICM.
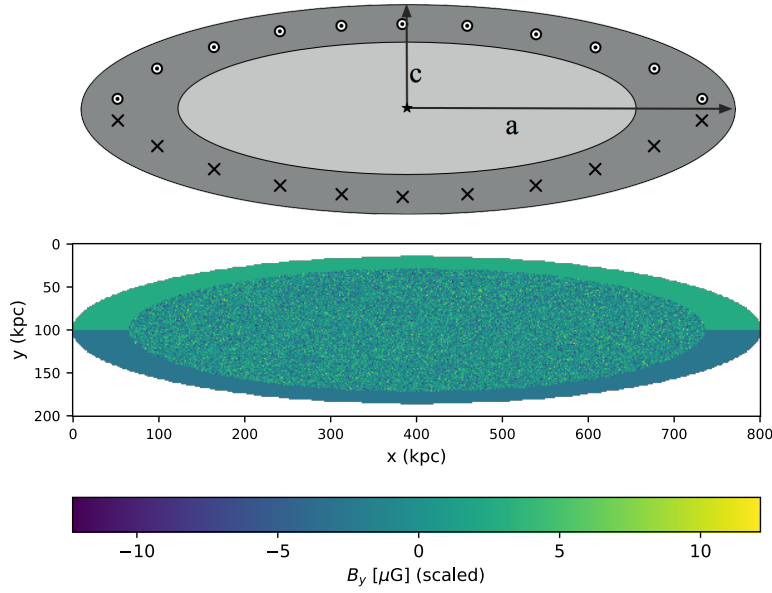
Figure 3.8: *Top:* A schematic of the magnetic field of the lobes, composed of the toroidal component within the lobe (dark grey) and Gaussian component within the jet (light grey), viewed from above. Crosses indicate a field directed out of the page, while dots show the field into the page. *Bottom*: The simulated version of the magnetic field, showing the component along the line-of-sight.

Magnetic field structure

The magnetic field within the jet is described by a Gaussian normal distribution with mean $\mu = 0$ and standard deviation $\sigma = B_{50}$, where B_{50} is the magnetic field strength corresponding to $\beta_m = p_T/p_B \sim 50$ (Huarte-Espinosa et al., 2011a).

Within the lobe, the field is regular and toroidal. As the direction of the back-flow of plasma is not modelled in this work, the direction of rotation for this toroidal component is an arbitrary one. In generating this toroidal field, the ellipsoidal radio source is "sliced" vertically according to x-value (Figure 3.9). This is equivalent to Equation 3.11 for a particular value of $x = k$ (and $b = c$), giving the radius normal to the x-axis:

$$\frac{k^2}{a^2} + \frac{y^2}{c^2} + \frac{z^2}{c^2} = 1 \tag{3.15}$$

$$\frac{y^2}{c^2} + \frac{z^2}{c^2} = 1 - \frac{k^2}{a^2} \tag{3.16}$$

$$r_k^2 = c^2\left(1 - \frac{k^2}{a^2}\right). \tag{3.17}$$
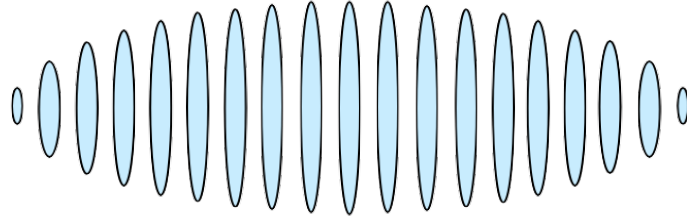
Figure 3.9: The model radio source, split vertically into disks according to x-value.

Horizontal slices in $y = m$ return an equivalent result through similarity rules,

$$r_m = r_k \frac{a}{c}. \tag{3.18}$$

The angle ϕ from the positive z-axis to the outer edge of the slice is then determined for each cell within the lobe and used to generate a circularly rotating field in the yz-plane,

$$\underline{\boldsymbol{B}}_l = T\hat{\underline{x}} + U\hat{\underline{y}} + V\hat{\underline{z}}, \tag{3.19}$$

for components

$$\begin{cases} T & = 0 \\ U & = B_0 \cos{(\phi)} \\ V & = -B_0 \sin{(\phi)}, \end{cases} \tag{3.20}$$

where $B_0 = \sqrt{\frac{2n_e k_\mathrm{B} T}{\beta_m}}$, $\beta_m = 50$.

In the case of a lobe orientation $\theta \neq 0$, the field for each one of these slices in x must be rotated anticlockwise about the z-axis by an angle θ using the rotation matrix:

$$\begin{bmatrix} \cos^2(\theta/2) - \sin^2(\theta/2) & -2\cos(\theta/2)\sin(\theta/2) & 0 \\ 2\cos(\theta/2)\sin(\theta/2) & \cos^2(\theta/2) - \sin^2(\theta/2) & 0 \\ 0 & 0 & 1 \end{bmatrix}, \tag{3.21}$$

giving a rotated toroidal field of

$$\underline{\boldsymbol{B}}_{l,\mathrm{rot}} = T_\mathrm{rot}\hat{\underline{x}} + U_\mathrm{rot}\hat{\underline{y}} + V\hat{\underline{z}}. \tag{3.22}$$

As all calculations for the RM are done along the line-of-sight $\hat{y}$, only the component U_rot is needed.

This field is applied throughout the lobe region. Within the jet itself, the y-component of the $\underline{\boldsymbol{B_j}}$ field is drawn from a Gaussian normal distribution of $N(\mu = 0, \sigma = B_0)$.
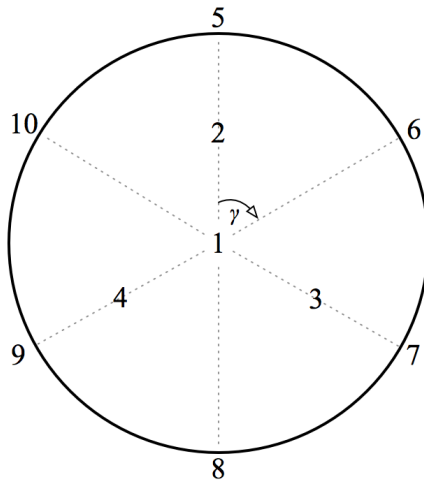
Figure 3.10: The construction of a single beam containing 10 rays arranged in regular order (numbered $1 - 10$ above). For simplicity, it is assumed that the FWHM of the beam is circular.

3.2.3   Beam and ray effects

Values for RM are determined by the cumulative effect of B_y and n_e along a particular line of sight defined by specific coördinates in x and z. Such lines of sight are hereafter referred to as *rays*, and in a physical observing system, multiple rays are combined and averaged into a single beam. This averaging of rays will contribute to the depolarisation of the observed emission, termed *beam depolarisation*.

Beams are defined by their full-width at half-maximum (FWHM) and contain 10 rays, split into 3 groups. The first ray is located at the centre of the beam, the next 3 are equally spaced in angle along an inner circle with radius of $d_b/4$, and the remaining 6 equally spaced along the beam edge (Figure 3.10). These beams are then packed as densely as possible along the projected jet axis of the lobes, with the outer extent of a single beam tangent to those neighbouring it (Figure 3.11).

The size of the beam FWHM relative to the projected size of the embedded radio source is a function of the source redshift, observing frequency, and is dependent on the radio dish used. For example, both FIRST (Faint Images of the Radio Sky at Twenty Centimeters; Becker et al. 1995) and NVSS (NRAO-VLA Sky Survey; Condon et al. 1998) observe at 20cm, however FIRST has a $5.4''$ beam whilst NVSS uses a $45''$ beam.

3.2.4   Conclusions

Within this Section, a theoretical framework was built for modelling a galaxy cluster and centrally-embedded radio source. For the environment, a power-law distribution describes the thermal electron number density, whilst the magnetic field distribution is random and isotropic, with a power-law spectrum. For the radio source, physical lobe sizes and axis ratios were adapted from
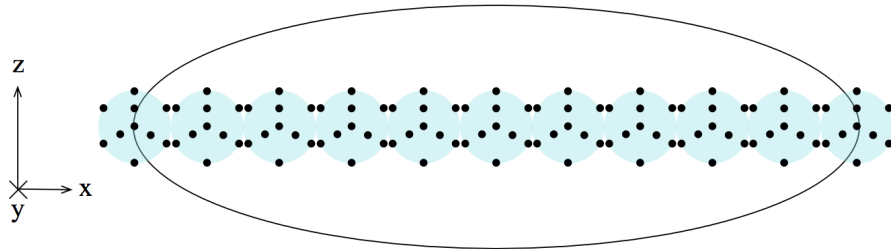
Figure 3.11: The ellipsoid lobe viewed in projection with beams (blue circles) and associated rays (black dots) distributed equally along the x-direction, corresponding to the semi-major axis of the ellipsoid.

the literature. The number density is assumed to be some small fraction of that within the ambient ICM, with a magnetic field distribution that is inwardly random and outwardly toroidal. Between the cluster environment and radio lobes lies an intermediate cocoon of shocked material which adopts the density of the ambient ICM and a magnetic field of varying degrees of toroidal order. Finally, the possible effects of telescope beam size on the observed radio source depolarisation were outlined, and the model generalised to allow for different beam FWHMs. With these simplistic models constructed, the relative impact of different density and magnetic field distributions can be investigated.

3.3   Investigation of simple models

Beginning first with the source model outlined in the previous Section, a series of galaxy cluster environments are simulated and the associated RM distributions calculated. The radio source adopts the properties outlined in Subsection 3.2.1 for all of the following cases, along with an arbitrary total source size $D = 400$ kpc, and is embedded at the centre of the galaxy cluster. The source is assumed to have equal surface brightness over all regions within the lobe. Hence, there is a computational weighting of 1 for all emission originating inside the source structure and a weighting of 0 outside it. This has the effect that any line of sight which does not intersect the radio source will measure zero RM.

3.3.1   Constant density

Constant magnetic field strength

The simplest non-trivial case is for constant density and magnetic field strength. Here, the thermal electron number density n_e is taken to be equal to $n_0 = 0.01$ cm^{-3} everywhere, corresponding to the maximum of the density distribution assumed by Carilli & Taylor (2002). The magnetic field strength $\underline{\boldsymbol{B}}$ is set such that the magnetic pressure is 10% of the thermal pressure as given in Equation 3.10, leading to a field strength of $\langle \underline{\boldsymbol{B}} \rangle \sim 0.6 \ \mu G$ everywhere within the cluster.

As seen in Figure 3.12, a decreased source angle with respect to the line of sight causes the source to appear shorter in x due to projection effects. Due to the constant thermal electron density for each galaxy cluster, different halo masses have no effect on the shape of the RM distribution. RM values are purely positive here due to the strictly positive values of B_y.

For a radio source in a constant density and constant magnetic field environment, the only differential factor across the projected jet axis is the depth of the line of sight. The effect of increasing and decreasing the path length of emission from the radio source is most apparent for larger angles, with the far lobe exhibiting greater RM. This would lead to a greater change in the polarisation angle of the observed radiation, however, as the radiation is not subject to field reversals along any line of sight, this will ultimately not lead to depolarisation.

3.3.2 King model density

Constant magnetic field strength

Consider the case with a constant magnetic field strength as in Subsection 3.3.1 but with a thermal electron number density which declines with radius as given by Equation 3.6. Now the varying density $n_{\rm e}(r)$ is a function of radius r from the cluster centre and is affected by the cluster halo mass, which then has an impact on the RM. The lower average density throughout the cluster also impacts the scaling for the magnetic field, which is now $\underline{B} \sim 3.5$ everywhere.

The impact of varying $n_{\rm e}$ with radius can be seen in Figure 3.13 for a source laying flat in the plane of the sky, where the greater density towards the centre of the cluster leads to a peak in RM. As the angle of the source increases, the RM of the far lobe is greatly increased from ~ 20 to 80 rad m^{-2}, whilst that of the near lobe is only slightly depressed and remains within $\sim 20 - 30$ rad m^{-2}. This shape is broadened when the underlying density distribution varies more slowly, as in a larger mass cluster (Figure 3.14).

Additionally, for source angles away from $0°$, an artefact – a sharp peak – is visible on the side of the far lobe. This appears to match the original transverse axis of the radio lobe, which, as the lobe is rotated, in intersected at increasingly large x away from zero. As this feature is not visible in Figure 3.12, it must be primarily a function of density along the line of sight.

With the added complexity in the density model, a pattern more reminiscent of the Laing-Garrington effect is also appearing. The large and sudden variation in RM around the transverse jet axis artefact could represent greater depolarisation at that location in the lobe, although the effect is not global; i.e. it does not extend over the entirety of the far lobe. Hence, whilst the density of the intervening medium does appear to contribute to changes in RM across the lobe, it cannot be the main driver of lobe depolarisation for any single line of sight.
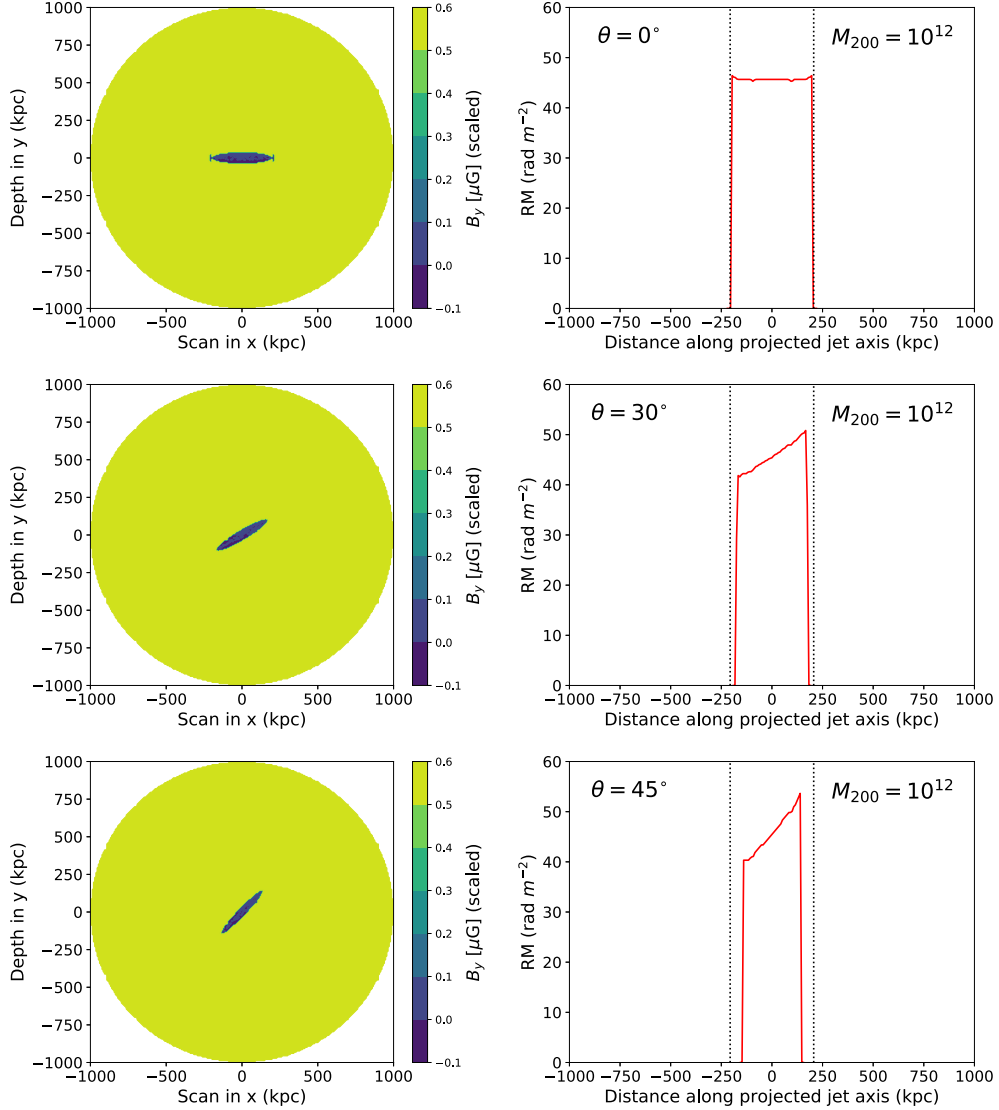
Figure 3.12: (*Left*): The magnetic field strength along the line of sight in a $M_{200} = 10^{12} M_\odot$ halo when sliced along the horizontal mid-plane, with embedded radio sources at angles of (*from top to bottom*) $\theta = 0°$, $30°$, and $45°$ to the plane of the sky. (*Right*): The RM as measured along the projected jet axis. The dashed black lines indicate the virial radius for the given halo, with the $10^{12} M_\odot$ halo mass cluster shown, giving $R_{vir} \approx 206$ kpc.
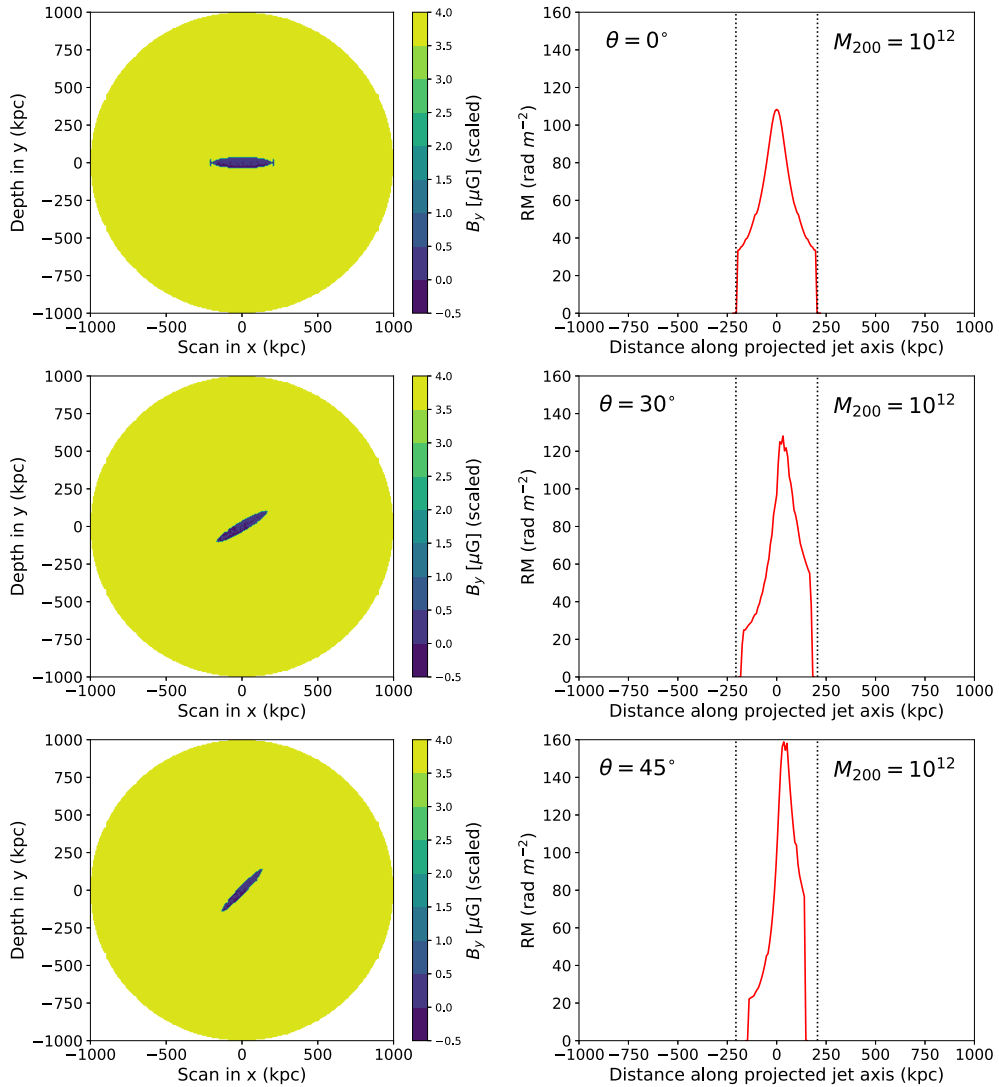
Figure 3.13: As in Figure 3.12, but for a varying thermal electron number density profile.
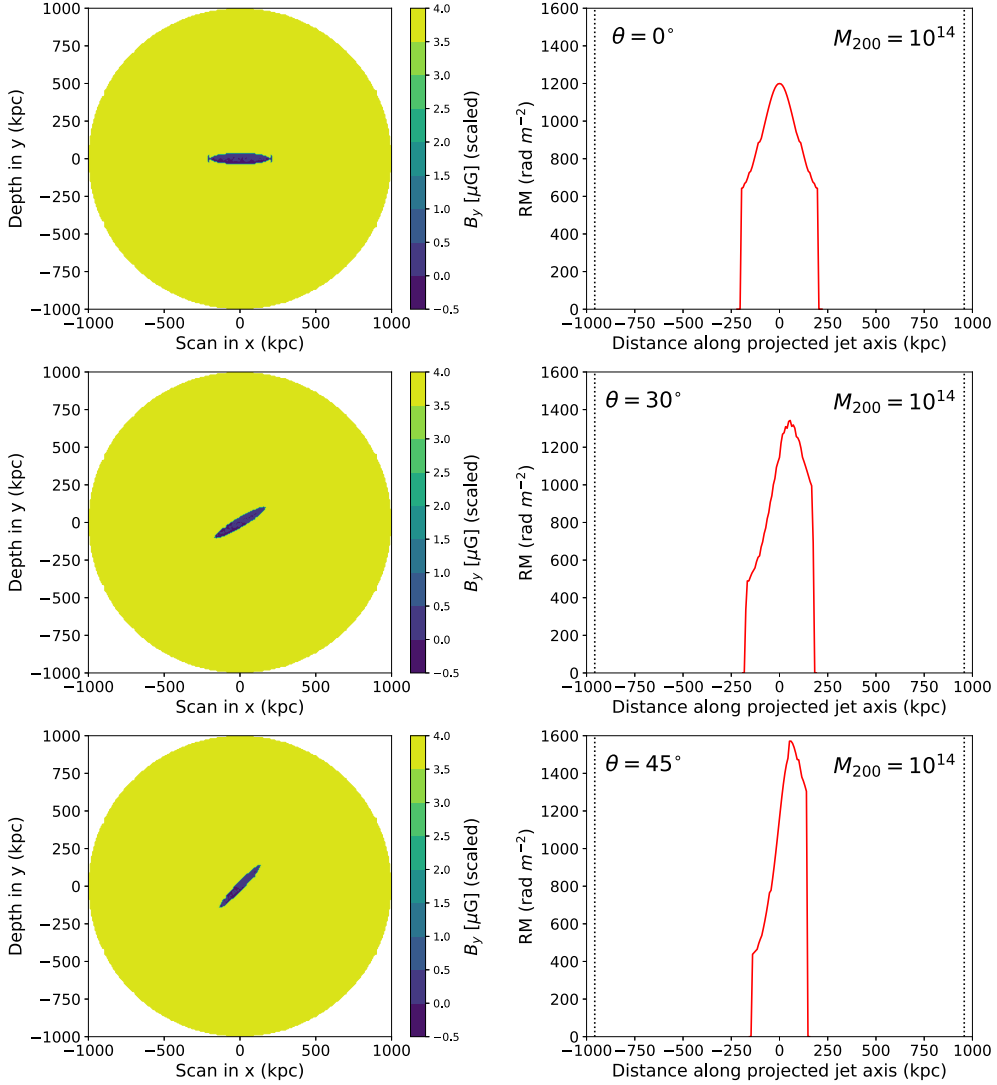
Figure 3.14: As in Figure 3.13, but for a cluster dark matter halo mass of $M_{200} = 10^{14} M_{\odot}$, giving a virial radius of 957 kpc.
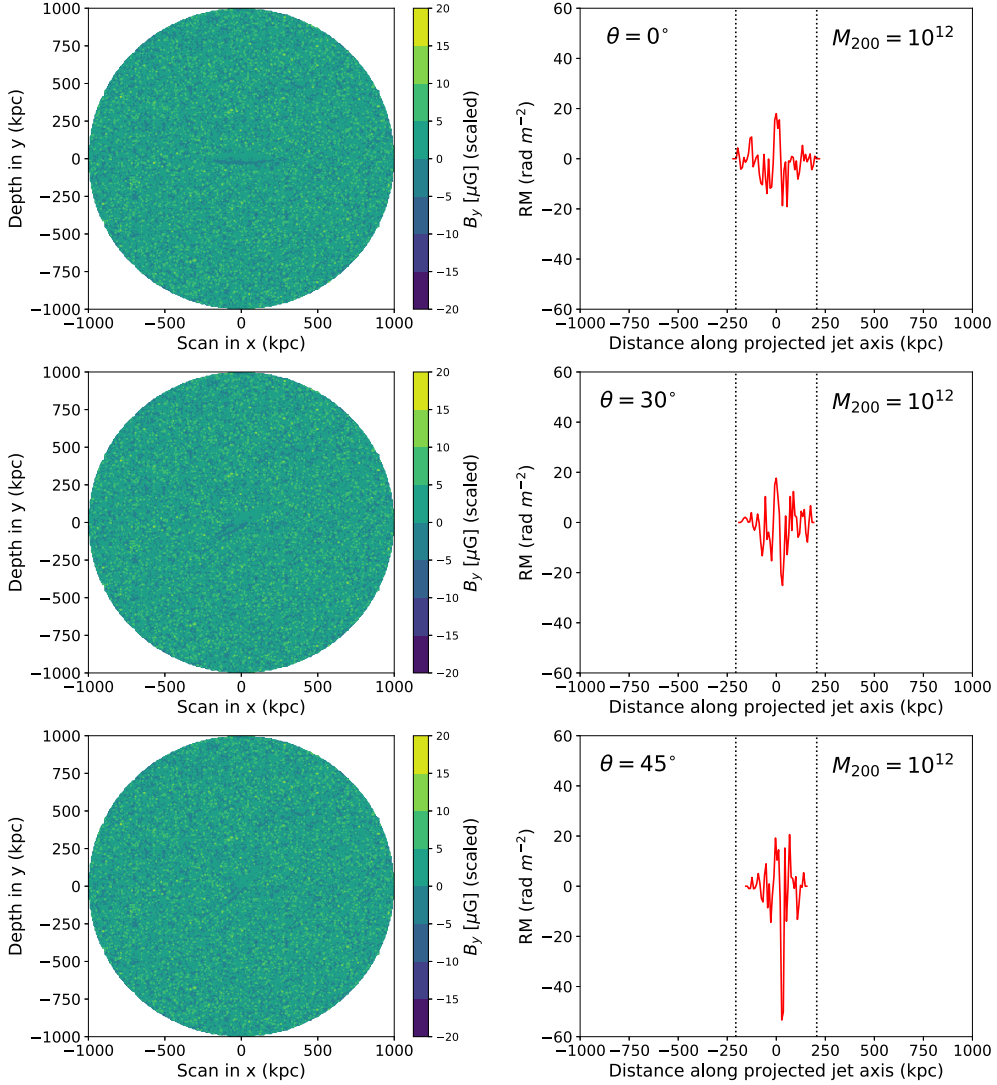
Figure 3.15: As in Figure 3.12, but for a varying thermal electron number density profile and random normal magnetic field strength.

Random magnetic field via normal distribution

We now enter into the regime where both the density n_e and magnetic field strength $\underline{\boldsymbol{B}}$ vary with location within the galaxy cluster. If $\underline{\boldsymbol{B}}$ is sampled from a normal distribution $N(0,1)$ then the distributions of Figure 3.15 are obtained. The fine grain of this normal distribution, however, adds noise into the RM profile, making it difficult to ascertain whether any significant asymmetry is present in the $45°$ case when compared to $0°$. Unlike previous cases there is no clear amplification of the RM signal with increasing angle, excluding an artefact present at $45°$.

There is no clear evidence of the Laing-Garrington effect for a randomly-distributed magnetic field, even when paired with the modified King model for thermal electron density as used previously. As such, the magnetic field distribution appears to be critical in amplifying or concealing differential RMs across the projected jet axis. The random B-field model therefore appears unphysical, and is not considered further in this work.

Random magnetic field via Fourier space

If $\underline{B}$ follows the isotropic random field of Equation 3.7, then the distribution of Figure 3.16 is achieved. This magnetic field distribution is of approximately the same strength along the line of sight as that of Section 3.3.2, but it is clumpier on scales of $10 - 20\,\mathrm{kpc}$, corresponding to the scale length of the magnetic field.

When comparing RM values for lobes angled at $0°$ and $45°$ to the plane of the sky, the difference is apparent. Their magnitude is suppressed for the nearer lobe and amplified for the farther one, once again with a spike near the centre of the source. Whilst the amplification on the far lobe side is generally towards more negative numbers in this case, it still follows the general trend of increasing the greatest magnitude of RM at higher angles. However, measuring the Laing-Garrington effect is made more difficult by the limited source size, particularly when seen in projection.

3.3.3 Cocoon

In each of the examples above the fractional ordering of the magnetic field within the cocoon is set to zero ($f = 0$), i.e. the area immediately outside of the lobe region has the same density and magnetic field configuration as that of the ambient cluster gas. Consider now a source for which $f = 1$, such that the magnetic field configuration of the cocoon is completely ordered with the same toroidal configuration as that within the lobe region.

As can be seen in Figure 3.17, a toroidal magnetic field within the cocoon around the radio source acts to increase the effective extent of that source into the environment. This leads to a greater suppression of RM for the nearer jet and a general increase in RM to more positive values for the receding jet. The magnitude of the RM extrema are decreased for the ordered case ($|RM|_{max} \sim 125 \rightarrow 60$), leading to a clearer signal similar to that of Figure 3.13.
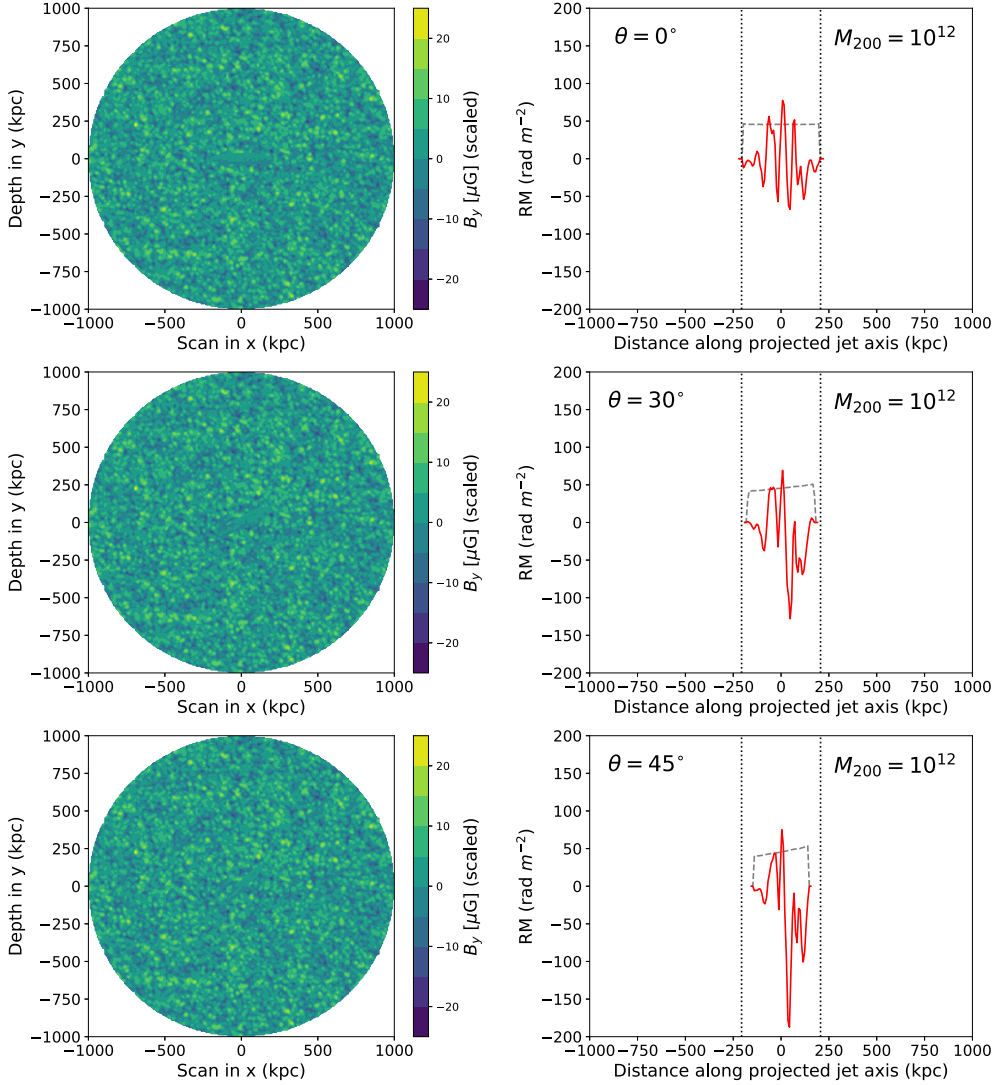
Figure 3.16: As in Figure 3.12, but for a varying thermal electron number density profile and magnetic field generated via Equation 3.7. The solid line denotes the results of Section 3.3.2, whilst the dashed line corresponds to Section 3.3.1
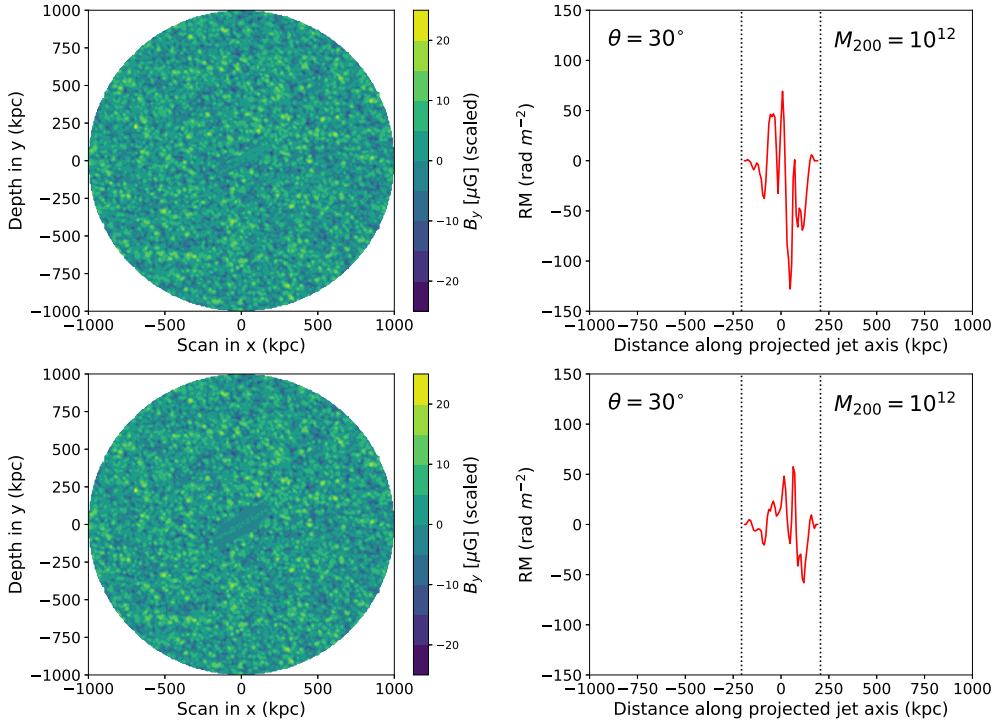
Figure 3.17: (*Left*) The magnetic field strength along the line of sight in a $M_{200} = 10^{12} \ M_\odot$ halo when sliced along the mid-plane, without an ordered cocoon (*top*) and with one (*bottom*). (*Right*) The RM as measured along the projected jet axis for source angled at $\theta = 30°$ to the plane of the sky. The dotted line gives the virial radius for this cluster at $r_{200} = 206$ kpc.

3.4 Conclusions

In this Chapter, models for a galaxy cluster and embedded radio source were presented. The relative importance of thermal electron number density n_e and magnetic field $\underline{\bm{B}}$ in producing Faraday Rotation was given in Section 3.1, with model distributions of the relevant parameters explored in Section 3.2. These models were then simulated and the resulting Rotation Measure RM analysed in Section 3.3.

The results of a model with constant $\underline{\bm{B}}$ and power-law n_e in Figure 3.13 demonstrated that a varying density distribution can lead to a significantly asymmetrical RM distribution along the projected jet axis, with the RM of the near lobe being depressed and that of the far lobe increased. This general shape persists over a wide range in halo mass ($M_{200} = 10^{12} - 10^{14} \ M_\odot$; Figure 3.14), albeit broadened for higher masses as these clusters see a less precipitous drop in density over the extent of the radio lobes. When this constant $\underline{\bm{B}}$ is replaced by a random normal distribution in $N(0, 1)$, this asymmetry is not apparent.

For the full model of this thesis, consisting of a power-law density distribution and random

isotropic magnetic field, slight asymmetries in the RM are seen once again. Figure 3.16 demonstrates that the extrema of the RM tend to increase in magnitude for the far lobe and decrease for the near lobe, with the effect greatest for sources that are closer to the line of sight ($45°$). Including an outer cocoon of entrained ICM material around the radio source acts to smooth the RM distribution, reducing the overall magnitude and variance (Figure 3.17). This smoothing allows for greater detail in the distribution to be seen, including an apparent increase in the relative variance of the RM on the side of the far lobe versus that at the near lobe. Such a pattern matches that expected for the Laing-Garrington effect (Section 1.3), in which the far lobe is preferentially depolarised due to the greater path length travelled by the emitted radiation. Greater variance in RM for one lobe may then lead to preferential depolarisation on that side when beam sizes are taken into account.

These computationally-tractable models suggest that Faraday Rotation may prove to be a useful metric in further constraining radio source and environment properties, however, the radio source properties as modelled in this chapter do not yet relate directly to radio observables. What remains is to introduce dynamical models for these sources, and to measure their radio observables when placed into a number of different of environments.

CHAPTER 4

Faraday Rotation from model radio sources

In Chapter 3, a series of models were outlined and combined for a radio source whose properties were motivated by results within the literature. In this chapter, more realistic source parameters are taken from the *Radio AGN in Semi-analytic Environments* model (RAiSE; Turner & Shabala, 2015), which traces the dynamical evolution of AGN radio lobes. Such dynamical models (e.g. Kaiser & Alexander, 1997; Blundell et al., 1999) can be used to infer the basic features of radio sources, and the predictions from these models can be compared to real observations to both test the theoretical models of radio source evolution, and to constrain the properties of those observed sources. To do so, the complex inner fluid dynamics of the jet must be converted to observables accessible by radio telescopes which view the radio source in projection (i.e. on the plane of the sky), such as the linear source size and the total surface brightness of the lobes. As discussed in Section 1.1.2 and demonstrated in Chapter 2, the environment into which a radio source expands can have a significant effect on its evolution, and so a model which is able to constrain the properties of that environment may be more accurate in its predictions for source properties. As shown in Chapter 3, the Faraday Rotation signature across a radio source (as characterised by the Rotation Measure, RM) can be used to probe the intracluster environment properties in addition to those of an embedded radio source.

Within this Chapter, the accuracy of this thesis' model for predicting various source and environment parameters is tested. In Section 4.1, the main components of the RAiSE model sources are outlined and compared to their counterparts from Chapter 3. A sample of radio source models are constructed from the larger parameter space in Section 4.2, and radio observables including Rotation Measure are characterised. In Section 4.3, the utility of RM in constraining source and environment properties is tested.

4.1 The RAiSE framework

In the RAiSE model, the radio lobe is described by many small volume elements in pressure equilibrium that grow independently over time, though typically assumed to be expanding into identical environments on either side of the active nucleus. The RAiSE model can simulate both FRII and jetted FRIs, the latter of which dominate in cluster populations of resolved radio sources; however, in this work, only FRII sources are considered. The default RAiSE environment is modified in this work, instead assuming jets are injected into an environment at $z = 0$ with a constant temperature profile of $T = 10^7$ K and density profile described by the modified King model of Section 3.2.1, matching the models used previously. Radio lobes modelled through RAiSE differ in how the energy and magnetic field strengths are determined, with the energy distribution of injected electrons following a power-law energy distribution $N(E) = N_0 E^{-s}$ for exponent $s = 2.4$ and normalisation constant N_0 (Turner et al., 2018b). Energy is lost from these electrons through multiple radiative modes (Kardashev, 1962), including adiabatic expansion, synchrotron radiation, and inverse-Compton scattering of photons from the CMB. The effect of these losses is characterised by the spectral break frequency ν_b, above which losses cause the spectrum to steepen by $\delta\alpha = 0.5$ (assuming a continuous injection of electrons).

The magnetic field strength within the lobes is considered to be homogeneous and locally described by a Maxwell-Boltzmann distribution (Hardcastle, 2013), with large-scale variations due to pressure changes over the lobe. This produces filamentary structures in the magnetic field which are observed in real sources (Eilek et al., 1997), which may exacerbate the effects of synchrotron losses by allowing high-energy electrons to travel into regions of locally high magnetic field strengths. The magnetic field strength and synchrotron losses then determine the synchrotron age of the radio source electron population for redshift z:

$$\tau = \frac{vB^{1/2}}{B^2 + B_{\rm ic}^2} \left[\nu_b(1+z)\right]^{-1/2},\qquad(4.1)$$

for microwave background equivalent field $B_{\rm ic} = 0.318(1+z)^2$ (Turner et al., 2018b) and constant of proportionality:

$$v = \left[\frac{243\pi m_e^5 c^2}{4\mu_0^2 e^7}\right]^{1/2}.\qquad(4.2)$$

Inverse-Compton losses are much less significant at low z, although synchrotron losses affect all sources of large physical extent.

The magnetic fields assumed by the RAiSE model are homogeneous in both magnitude and direction, at odds with the models previously assumed in Section 3.2.2, which are characterised by a Gaussian-distributed spine and constant toroidal sheath. In this work, the spatial distribution of the RAiSE magnetic field is not considered, and instead the resulting magnitude is applied to the distribution previously modelled in Chapter 3.

The magnitude of the magnetic field within the cocoon and lobe is scaled according to the
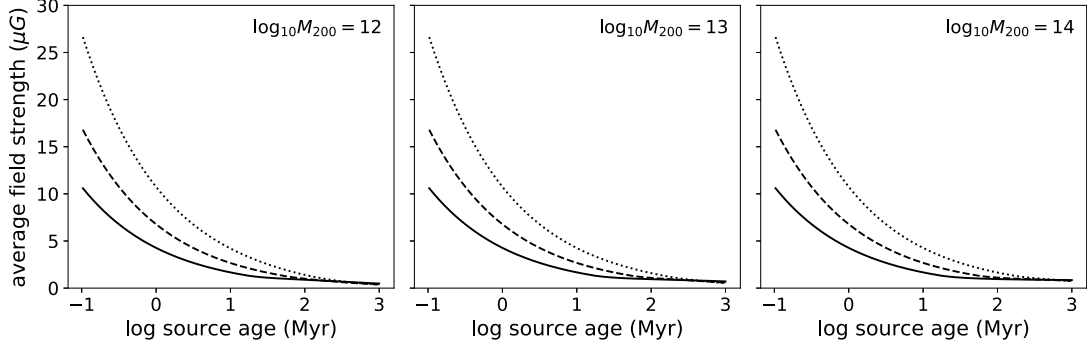
Figure 4.1: The average magnetic field strength within the radio lobes from RAiSE over the source age t_{age} for a subsample of dark matter halo masses of (*left*) $10^{12}\ M_{\odot}$, (*middle*) $10^{13}\ M_{\odot}$, and (*right*) $10^{14}\ M_{\odot}$. Solid lines are for jet powers Q of 10^{37} W, dashed for 10^{38} W, and dotted for 10^{39} W.

magnetic energy density at time t_{age} (Kaiser et al., 1997):

$$u_B(t_{\mathrm{age}}) = \frac{qp_c(t_{\mathrm{age}})}{(\Gamma_c - 1)(q + 1)}, \tag{4.3}$$

where $q = 0.02$ is the ratio of the magnetic energy density u_B to the particle energy density $u_e + u_T$ (Kaiser et al., 1997; Turner et al., 2018b). The ratio of magnetic field strength to equipartition field strength is then $B/B_{\mathrm{eq}} = q^{2/(s+5)} = 0.35$ for all radio lobes at all times. The generated magnetic field strengths of $\sim 1 - 4\ \mu$G (Figure 4.1, Table 4.1), are comparable to those found by Ineson et al. (2017), showing that they are reasonable in this context.

The source length D and axis ratio $\mathscr{A}$, lobe pressure p_c and density ρ_c, jet axis Mach number $\mathscr{M}_{maj}$, and luminosity L_ν are modelled over the evolutionary history of the source at regular steps in age t_{age} up to a maximum age of 1 Gyr. The total source length and axis ratio are used to set the extent of the radio lobe, with ellipsoid parameters for the cocoon and inner jet set by the same relative proportions as outlined in Section 3.2.2. Lobes in the supersonic regime may expand self-similarly (Kaiser & Alexander, 1997), however, the rate of expansion is lower for the subsonic phase and so the assumption of self-similar growth does not apply in this regime. If growth is self-similar, then the axis ratio of the radio lobe will remain constant with time. As is seen in Figure 4.2 for an injected axis ratio of $A = 4$, self-similar expansion is not a reasonable assumption beyond an age of ~ 10 Myr for the sources modelled here. In addition, the effects of buoyancy and large inverse-Compton losses are not considered for very old (> 300 Myr) sources, and the treatment of instabilities for these sources may not be valid. The evolving axis ratio described by the RAiSE model is accounted for in this work, however the source shape at ~ 300 Myr deviates somewhat from ellipsoidal (Figure 4.3). As all volume elements are considered to contribute equally to the total source luminosity, this shape irregularity has no effect on the analysis.

Table 4.1: The magnetic field magnitude within the radio source and cocoon for a subsample of models with integer values for $\log M_{200}$ and $\log Q$. Columns are (1) the dark matter halo mass of the cluster/group, (2) the jet power, and (3-6) the magnetic field strength at each of the source ages of 10, 30, 100, and 300 Myr.

M_{200}	Q	$\langle |B| \rangle \, [\mu G]$			
$[\log_{10} M_\odot]$	$[\log_{10} W]$	10 Myr	30 Myr	100 Myr	300 Myr
(1)	(2)	(3)	(4)	(5)	(6)
12	37	1.65	1.10	0.89	0.68
12	38	2.64	1.63	0.98	0.62
12	39	4.17	2.53	1.38	0.71
13	37	1.66	1.11	0.94	0.84
13	38	2.66	1.66	1.08	0.82
13	39	4.22	2.64	1.56	0.91
14	37	1.66	1.12	0.96	0.89
14	38	2.66	1.67	1.10	0.92
14	39	4.23	2.67	1.63	1.05
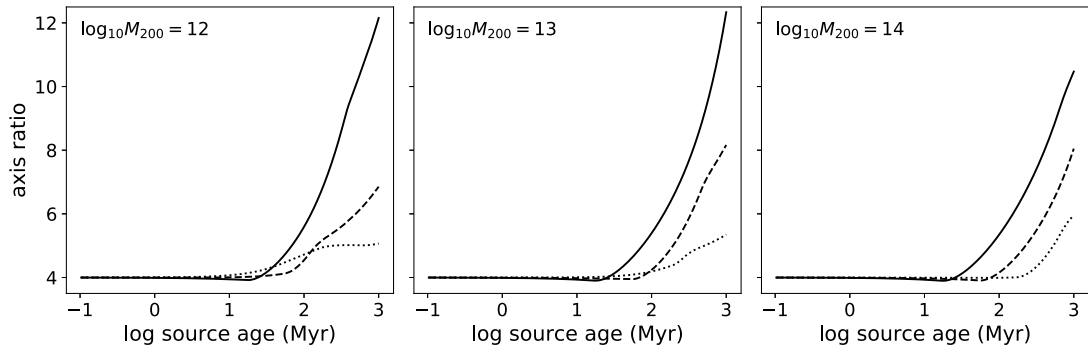
Figure 4.2: The radio lobe axis ratio $\mathscr{A}$ over the source age t_{age} for dark matter halo masses of (*left*) $10^{12} \, M_\odot$, (*middle*) $10^{13} \, M_\odot$, and (*right*) $10^{14} \, M_\odot$. Line styles are as in Figure 4.1.
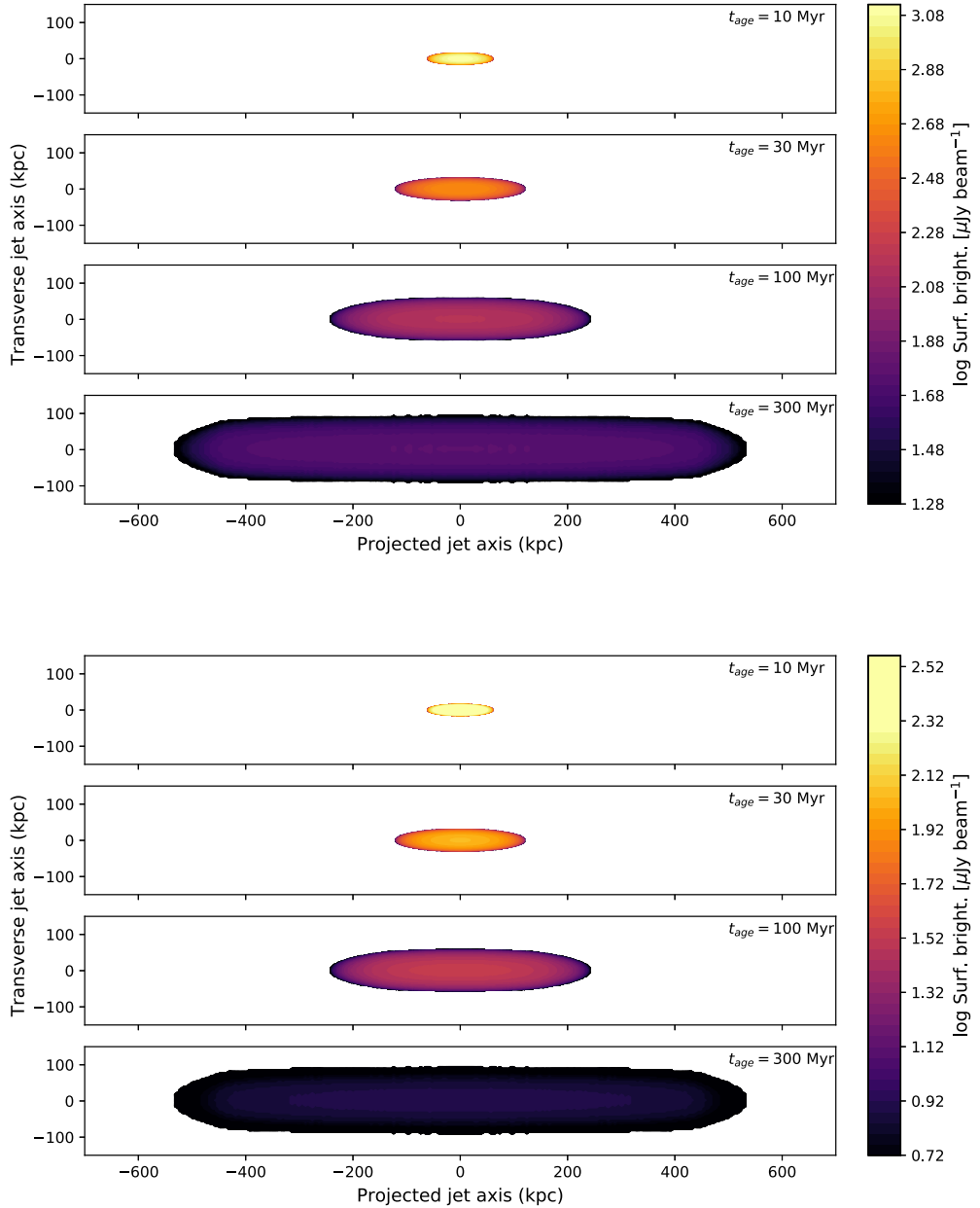
Figure 4.3: The evolution of projected surface brightness over time for a $Q = 10^{38}$ W source in a $M_{200} = 10^{13} M_\odot$ environment, observed at $\nu = 204$ MHz (*top*) and $\nu = 1400$ MHz (*bottom*).

The density of the source is determined using the pressure inside the lobes:

$$\rho_c = \frac{\Gamma_c p_c}{c_c^2}, \tag{4.4}$$

for adiabatic index Γ_c and sound speed c_c inside the cocoon/lobe, from Kaiser & Alexander (1997):

$$c_c = c \sqrt{\frac{\Gamma_c(\Gamma_c - 1)(5 - \beta)(\gamma_j - 1)}{9\left[\Gamma_c + (\Gamma_c - 1)\frac{c_2}{4\phi^2}\right] - 4 - \beta}}, \tag{4.5}$$

with β of Equation 3.6, opening angle ϕ, jet Lorentz factor γ_j, and function c_2 depending only on the adiabatic indices Γ_c and Γ_j of the cocoon and jet respectively:

$$c_2 = \left[\frac{(\Gamma_c - 1)(\Gamma_j - 1)}{4\Gamma_c} + 1\right]^{\Gamma_c/(\Gamma_c - 1)} \frac{\Gamma_j + 1}{\Gamma_j - 1}. \tag{4.6}$$

Typical values are adopted for these and other parameters, which are summarised in Table 4.2 (Kaiser & Alexander, 1997; Turner et al., 2018b).

Assuming that the lobe material is optically thin, the luminosity of the radio lobes is calculated by summing the individual contributions from each volume cell along the line of sight through the source, producing two-dimensional surface brightness maps as in Figure 4.3. Older sources ($\geq$ 100 Myr) are less luminous due to adiabatic losses and inverse-Compton upscattering of CMB photons. Luminosity is also reduced at higher frequency due to the power-law dependence of the electron energy distribution, $L_\nu \propto \nu^{(1-s)/2}$ for $s = 2 - 3$. In spite of these losses, the surface brightness of the radio lobes appears consistent with a model in which volume cells contribute an equal amount to the overall luminosity, with only the total luminosity and source size varying over time. As a result, it is assumed that all cells within the lobe generate the same level of emission.

4.2 Selected sources

To test the utility of RM in improving estimations for source and environment parameters, sources are taken from the RAiSE simulations of Section 4.1 and embedded into the environments of Section 3.3.2, where observables of source length and source luminosity are measured. The same observables are determined for a smaller set of randomly sampled sources, and based on these observed parameters, a best-fit RAiSE model is assigned. This process is then repeated including additional observables on RM, and the goodness-of-fit of the best-fit models are compared for the two-observable and four-observable methods. This allows for an investigation on how RM data can help constrain radio source and environment parameters.

Radio sources with jet powers ranging from $Q = 10^{37}$–10^{39} W in increments of 0.25 dex are simulated within environments with dark matter halo masses $M_{200} = 10^{12}$–10^{14} M$_\odot$, again in steps of 0.25 dex. As in Chapter 3, radio sources are observed at angles of $\theta = 0°$, $30°$, and $45°$ to the plane of the sky. These sources are evolved up to an age of 1 Gyr. Below the age of

Table 4.2: Initial RAiSE model parameters

Environment parameters		Values
Temperature	T	10^7 K
Density profile	β	1.5
Radio source parameters		Values
Initial axis ratio	A	4
Equipartition factor	q	0.02
Injection index	s	2.4
Adiabatic index	Γ_c, Γ_j	4/3
Lorentz factor	γ_j	2
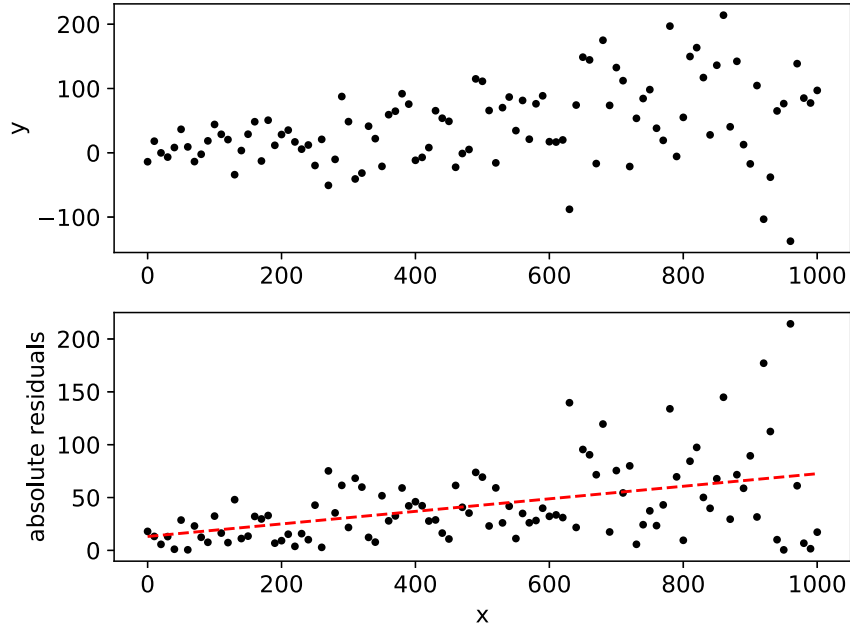
~ 10 Myr, projected source sizes may be too small to perform any reasonable analysis on the distribution of RM along the projected jet axis, whilst sources significantly above ~ 100 Myr in age are less accurately fit by an ellipsoidal model due to both greater inverse-Compton and synchrotron losses in the older parts of the lobe near the nucleus (Turner et al., 2018a), making them increasingly unsuitable for analysis in this work. From these available parameter spaces, 108 different combinations of Q, M_{200}, t_{age}, and θ are produced, with three observable frequencies for each model – 204, 232, and 1400 MHz. The range of $204-232$ MHz is representative of the new generation of low-frequency telescopes (e.g. LOFAR and the MWA), whilst 1400 MHz is well-sampled by existing VLA surveys such as FIRST and NVSS. As such, the scope of this work covers both the large set of radio data already existing along with sources that will be well-sampled within the next decade.

One $L - D$ track from the RAiSE models is chosen at times of approximately $t = 10$, 30, 100, and 300 Myr into the source evolution (Table 4.3), providing values for source length D and luminosity L_ν. The RM distributions of each source then provide two additional metrics which may be used to constrain the system properties: the dispersion, σ_{RM}, and the heteroscedasticity, H.

A variable is described as heteroscedastic if its variance changes with a change in another variable. An example of this can be seen in Figure 4.4, with an increasing variance in the y variable as the x variable is increased. Heteroscedasticity is also apparent in the RM of modelled sources (Figure 4.5), with an increasing variance in RM as the jet axis becomes more aligned with the line of sight. The level of heteroscedasticity is assessed by performing linear regression on the absolute value of the RM, and the slope of this fit is then assigned to the observed parameter H. As the RM is susceptible to large, random fluctuations in the underlying magnetic field distribution, it is first smoothed by a median window filter of size 3 before the linear fit is determined.

Table 4.3: Selected model parameters. † identifies values which are observed.

| Environment parameters		Values	
Halo mass	M_{200}	10^{12}–10^{14} [in steps of 0.25 dex]	$M_\odot$
Radio source parameters		Values	
Power	Q	10^{37}–10^{39} [in steps of 0.25 dex]	W
Age	t_{age}	10, 30, 100, 300	Myr
Orientation	θ	0, 30, 45	deg
Frequency	ν	204, 232, 1400	MHz
Total source length†	D		
Total source luminosity†	L_ν		
RM dispersion†	σ_{RM}		
RM heteroscedasticity†	H		

Figure 4.4: (*Top*): Mock data displaying heteroscedasticity in the y variable. (*Bottom*): The absolute residuals of the mock data after performing linear regression. There is a clear increase in the residuals of this fit with increasing x (dashed).
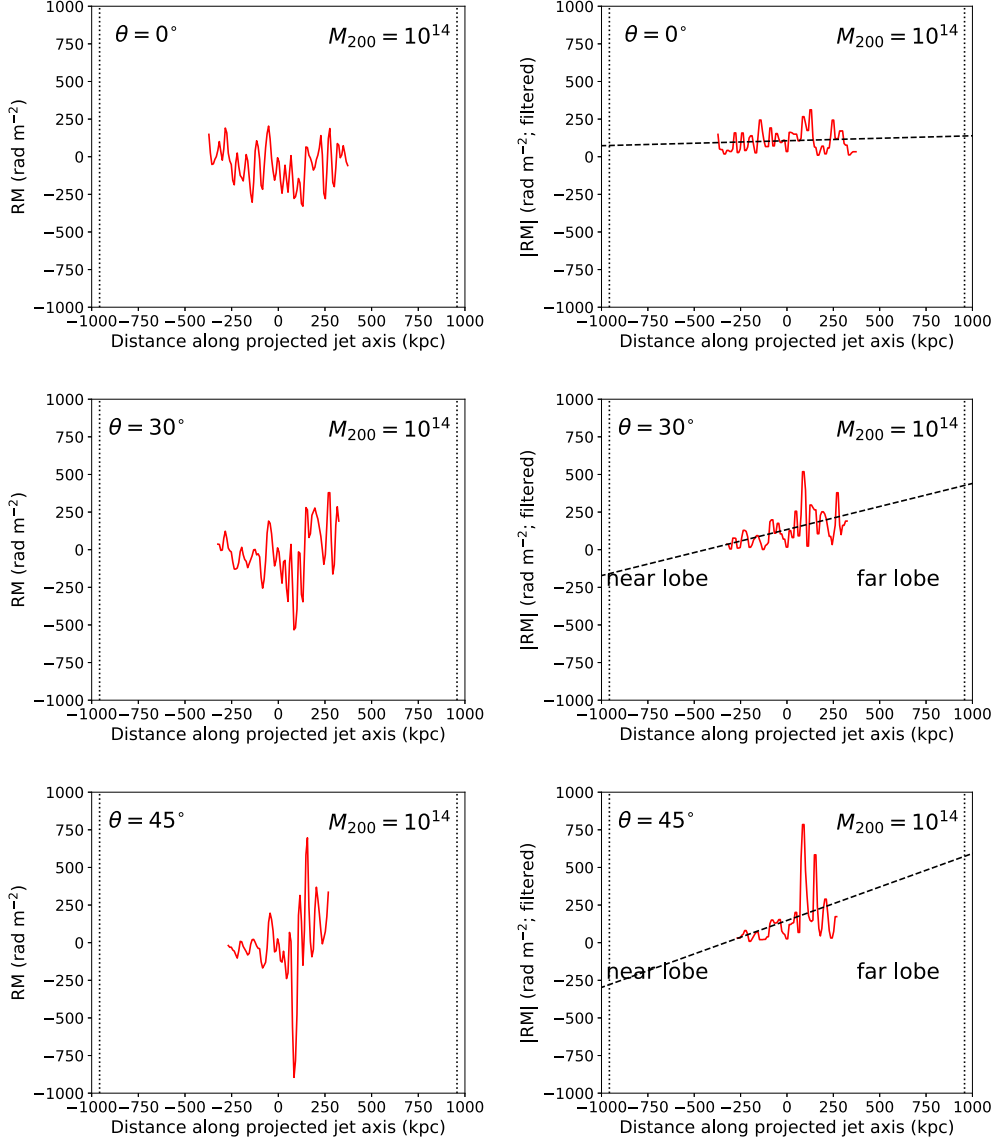
Figure 4.5: (*Left*): The RM signature for a source with $Q = 10^{39}$ W, $t_{\text{age}} = 100$ Myr, and $M_{200} = 10^{14}\ M_\odot$ for source orientations of (*top to bottom*) $0°$ (source in the plane of the sky), $30°$, and $45°$. (*Right*): The linear fit to $|RM|$ (dashed line), the slope of which is a measure of the heteroscedasticity and denoted H, after applying a median window filter of size 3. Dotted lines indicate the virial radius of this cluster at $r_{200} \sim 957$. The corresponding magnetic field distribution is shown in Figure 4.6.
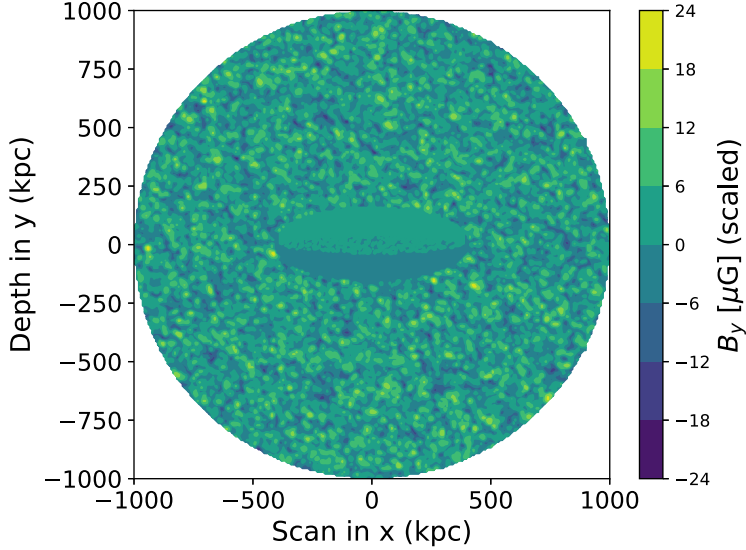
Figure 4.6: The magnetic field strength along the line of sight in a $M_{200} = 10^{14} M_\odot$ halo when sliced along the horizontal mid-plane, with embedded radio source at angle of $Q = 10^{39}$ W, $t_{\text{age}} = 100$ Myr, and $\theta = 0°$ to the plane of the sky.

The slope of the linear fit H is observed to increase with an increasing angle, i.e. the H value is consistently larger for sources angled at both $30°$ and $45°$ than for those at $0°$, although the small total sizes in the youngest sources may obscure this relationship. This can be seen by comparing the level of heteroscedasticity of the angled sources ($\theta = 30°$ and $45°$) to those flat in the plane of the sky at $0°$. For each combination of Q, M_{200}, and L_ν at a given source age t_{age}, the log difference in heteroscedasticity for the different orientations is calculated. For each source age, the distributions of $\log|H_{30°}| - \log|H_{0°}|$ and $\log|H_{45°}| - \log|H_{0°}|$ are produced, and are shown in Figure 4.7. These results show that sources at both $30°$ and $45°$ tend to display greater heteroscedasticity than those at $0°$, with values tending towards zero as the source age decreases and plateauing for the oldest sources, the latter likely due to radio lobes exceeding the virial radius of the cluster (Appendix D) in radial length. This is a consequence of the density dependence of the RM, as lower mass halos have their mass concentrated over a physically smaller region, and so a larger proportion of the radio source is viewed through less dense material.

Heteroscedasticity in RM may be a visible consequence of the Laing-Garrington effect as described in Chapter 1, Section 1.3. Here, emission originating from the far lobe must travel through a greater distance of the depolarising cluster material and is subjected to a greater number of magnetic field reversals along the line of sight, leading to more significant variation in RM. Since the sources modelled here are not viewed at a large angle to the plane of the sky (close to $90°$), Doppler beaming is not a significant factor and is not included in the model. Additionally, unlike the sources modelled in Chapter 3, the sources within this model are not young (< 10 Myr) and hence have a sufficiently large physical extent that allows this effect to
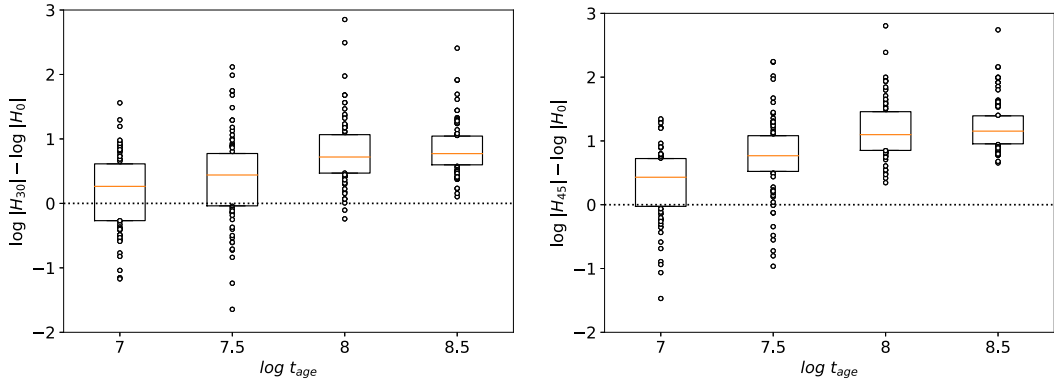
Figure 4.7: The log difference in heteroscedasticity H between sources angled at 30 degrees (*left*) and 45 degrees (*right*) to those at 0 degrees, at four different ages. Older sources generally have larger H values, whilst those at 45 degrees have larger slopes more consistently than those at 30 degrees as a whole. Boxes extend from the lower to upper quartile, with the median represented by the orange line. All points outside of the interquartile range are shown as open circles. The horizontal dashed line represents the case where there is no difference in heteroscedasticity between $0°$ and the angle being tested (either $30°$ or $45°$). Each source age shown above contains 243 data points.

be discerned above the noise. As such, the Laing-Garrington effect as seen here is a result only of the plasma properties within the source and surrounding environment, with the latter having the greatest impact on the overall RM profile . This supports the idea that the Laing-Garrington effect is a phenomenon that predominately arises from properties external to the radio source, as opposed an intrinsic one-sidedness, Doppler beaming, or internal depolarisation.

4.2.1 Test sources

Values of M_{200} and Q are randomly sampled from their discrete parameter spaces. The source age, t_{age}, can take on any value between ~ 10 and ~ 300 Myr, and the source orientation θ can be any integer value between 0 and $45°$. These parameters are then combined to form a series of test sources or *observations* – five for each halo mass – against which the model's accuracy can be tested. The chosen parameters for a subset of 10 cases are shown in Table 4.4; the total sample numbers 135.

For these test sources, as in the total model population of this chapter, the source length, luminosity, RM dispersion, and RM heteroscedasticity is measured for the three different frequencies. These test cases are then compared to each of the known models, and the best fit identified both with and without inclusion of RM metrics when performing the comparisons. By quantifying how well a randomly-generated source can be matched to a known model when measures of the RM are known, compared to when they are not, the utility of RM statistics in constraining source and environment properties can be assessed.

Table 4.4: A subset of the randomly sampled parameters used to generate the test sources. Columns are (1) model identifier, (2) cluster/group dark matter halo mass, (3) jet power, (4) radio source age, (5) source orientation with respect to the plane of the sky.

#	M_{200}	Q	t_{age}	θ
	$\log \mathrm{M}_\odot$	$\log \mathrm{W}$	Myr	Degrees
12_01	12	39.00	17	39
12_02	12	37.25	322	6
12_03	12	39.00	67	25
12_04	12	37.00	13	32
12_05	12	37.00	54	34
$\vdots$	$\vdots$	$\vdots$	$\vdots$	$\vdots$
14_01	14	38.00	151	36
14_02	14	38.00	168	24
14_03	14	38.00	151	38
14_04	14	37.25	33	17
14_05	14	38.25	259	27

4.3 Testing predictive power

The goodness-of-fit between an observation and any given model is determined through the χ^2 statistic in log-space:

$$\chi^2 = \left(\frac{\log x_{1,r} - \log x_{1,m}}{\sigma_{\log x_1}} \right)^2 + \left(\frac{\log x_{2,r} - \log x_{2,m}}{\sigma_{\log x_2}} \right)^2 + \ldots \tag{4.7}$$

where x_i are the observables being compared, the subscripts r and m denote the observed sample and the model being compared against, and $\sigma_{\log x_i}$ is the uncertainty of parameter x_i. As the purpose of this thesis is to investigate the potential of Faraday Rotation in constraining radio source and environment properties, the χ^2 statistic is calculated first for observables L and D only, and then for observables L, D, σ_{RM}, and H. The uncertainty in these fits is dominated by the sparse sampling of the model in t_{age}, with a conservative estimate of $\sigma_{\log L} = \sigma_{\log D} = \sigma_{\log \sigma_{RM}} = \sigma_{\log H} = 0.5$ dex. The only requirement placed on the system is that the frequency of observation of the test source match that of the models it is compared against.

The relative χ^2 probability is then, for approximately two degrees of freedom:

$$P(\chi^2) \propto \exp \left(-\frac{\chi^2}{2} \right), \tag{4.8}$$

which determines the relative likelihood of each test model matching each observed source. The model which produces the greatest value of $P(\chi^2)$ is taken to be the best estimate of the source and environment properties for that test case.

The log difference between the best predicted values of t_{age}, θ, M_{200}, and Q and the actual values are shown in Figure E.1. Whilst the inclusion of the RM parameters in the χ^2 fit greatly constrains the halo mass, the model has notable difficulty in fitting the source angle. This increased spread will then be distributed over the predicted values for other source parameters, including age and length. The parameters which were sampled from discrete distributions (M_{200} and Q) for the comparison sources are unsurprisingly the best-fitted, and the spread in other parameters can be partly attributed to the inherent improbability of finding a perfect-match model. As such, an analysis limited only to the accuracy of the best-fit model is heavily influenced by the sampling rate of parameter spaces in the model population, and this undersampling of M_{200} and Q make the histograms in Appendix E an inadequate representation of the model fitting.

An alternative assessment of the goodness-of-fit is to consider the spread of probabilities for a given test case, as shown by a set of marginalised one-dimensional relative-probability distributions. This spread is well described by a Gaussian distribution, however, test cases with parameters that lie near the extreme of their parameter space (e.g. $Q = 10^{37}$ and 10^{39} W) cannot be accurately fit by a Gaussian distribution as they are expected to peak at the boundary of the sampled space, leaving one side of the fit unconstrained and artificially increasing both the displacement of the maximum away from zero and the FWHM. As such, only observed sources with ages of $t_{\text{age}} = \sim 20 - 180$ Myr, angles of $5 - 40°$, masses of $M_{200} = 10^{12.25} - 10^{13.75}\ M_\odot$, and jet powers $Q = 10^{37.25} - 10^{38.75}$ W are shown..

On an individual observation basis, the marginalised one-dimensional relative-probability distributions are formed by summing over all other variables within the model, and scaled such that the distribution has a peak of $a = \frac{1}{\sigma\sqrt{2\pi}}$ for standard deviation σ. The resultant distribution is approximately log-normal, with the peak of this curve corresponding to the probability per dex centred at the mean. The model which returns the greatest a value is taken to be the best-fitting model for the observation (Figure 4.8). The average fits to source age, source angle, jet power, and galaxy cluster dark matter halo mass are shown in Figure 4.9. The inclusion of RM metrics at any given frequency aids in constraining the best-fit model in all cases with the exception of the jet power which is correctly identified in $\sim 100\%$ of tests regardless.
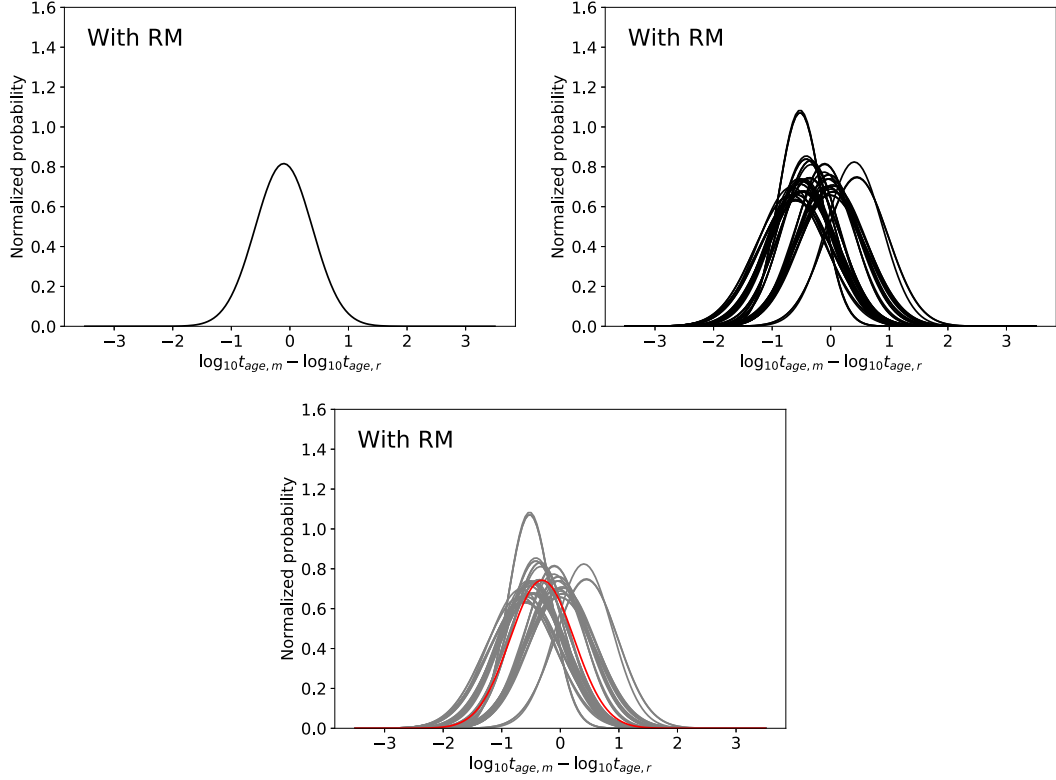
Figure 4.8: (*Top left*): An individual marginalised, one-dimensional relative-probability distribution for test source 12_05 (Table 4.4) in source age, the maximum confidence being associated with the best-fit model to the observation. (*Top right*): The relative-probability distributions for all observations with t_{age} between $20 - 180$ Myr. (*Bottom*): The average relative-probability distribution for the log difference between observed age and model age in red, overlaying the individual distributions in grey.
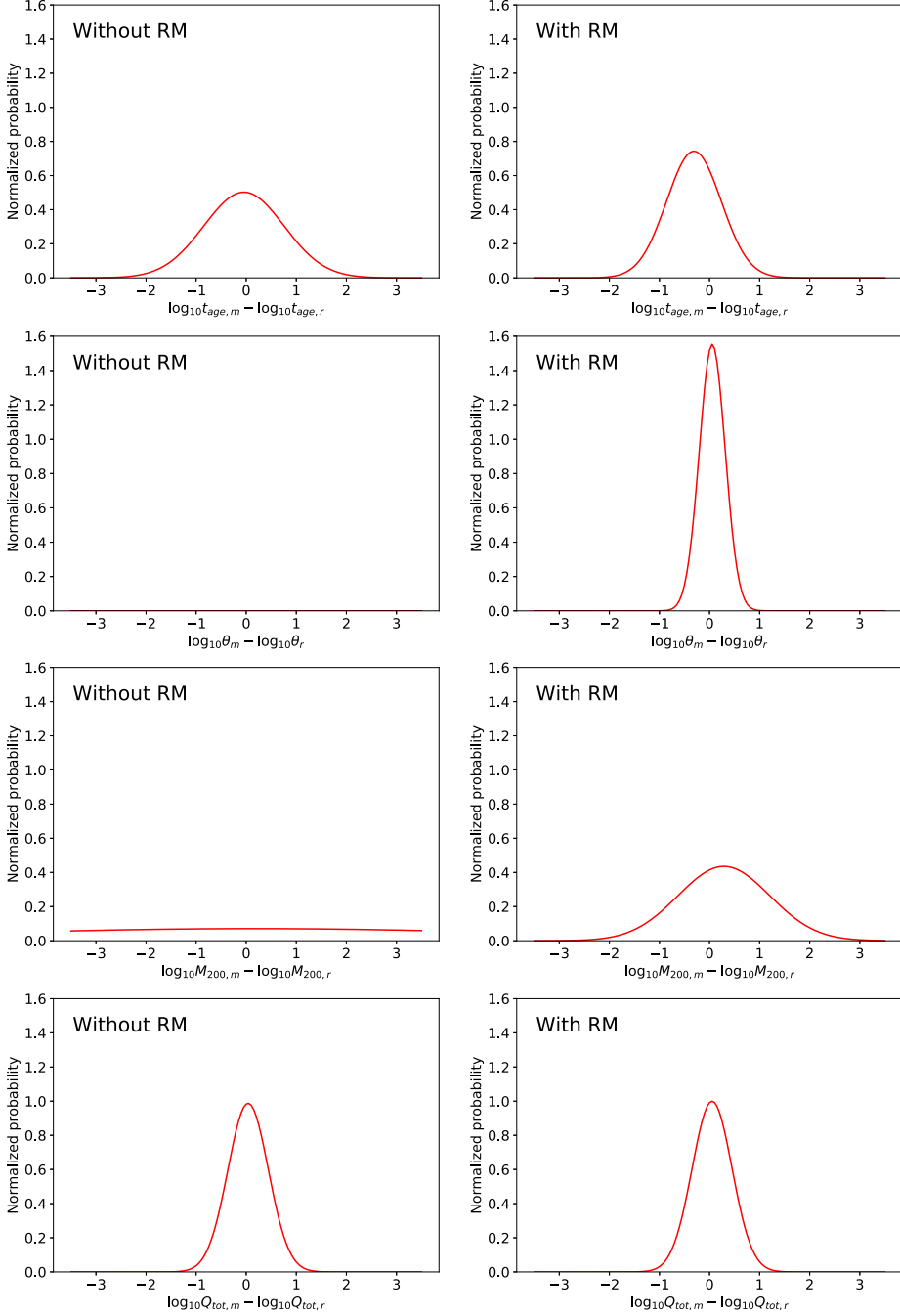
Figure 4.9: The average log difference relative-probability distribution between (*from top to bottom*) all observed and model source ages between $20 - 180$ Myr, source angles between $5 - 40°$, environment dark matter halo masses between $10^{12.25} - 10^{13.75}$ $M_{\odot}$, and jet powers between $10^{37.25} - 10^{38.75}$ W, both when RM parameters are not included in the χ^2 model (*left*) and when they are (*right*).

Table 4.5: Measures of the goodness-of-fit between test cases and the model population, as fitted by Gaussian distributions, with the RM measures alternately excluded (2-4) and included (5-7). Columns are (1) the parameter being fitted, (2,5) the certainty of the average best-fit model (3,6) the average log difference between the test parameter and the best-fit model parameter, and (4,7) the standard deviation of the average best-fit model.

Parameter [log units]	Without σ_{RM} and H			With σ_{RM} and H			$\frac{P_{RM}}{P_{\text{no } RM}}$
	$P(\mu)_{av}$ [per dex]	μ_{av} [dex]	σ_{av} [dex]	$P(\mu)_{av}$ [per dex]	μ_{av} [dex]	σ_{av} [dex]	
(1)	(2)	(3)	(4)	(5)	(6)	(7)	(8)
t_{age}	0.50	-0.05	0.80 ± 0.08	0.74	-0.31	0.54 ± 0.06	1.48
θ	~ 0	~ 0	3535.82 ± 265.98	1.55	0.05	0.26 ± 0.11	1.38×10^4
Q	0.99	0.04	0.40 ± 0.01	1.00	0.05	0.40 ± 0.02	1.01
M_{200}	0.07	0.15	5.64 ± 1.80	0.44	0.29	0.92 ± 0.28	6.16

For source age, source angle, and halo mass, the addition of RM and H into Equation 4.7 makes the best estimate more precise (i.e. lower standard deviation), but less accurate (i.e. greater non-zero mean). As shown in Table 4.5, including RM statistics when fitting sources to a model increases the normalised probability ($P(\mu)_{\text{av}}$), but tends to fit to models that are further away from the true value of that parameter (μ_{av}). Significant improvements are also seen in the standard deviation of the average relative-probability distribution (σ_{av}), with the only outlier to this patten is for the jet power Q, however this parameter is correctly estimated in all cases already. The best improvement is for the source angle, for which the probability that the fit is accurate to within a log-scale tolerance of ϵ is a factor of 1.38×10^4 greater when including RM and H, followed by the halo mass with a fractional improvement on the confidence of 6.16 ± 0.07, although this is accompanied by an increase in the mean from $\sigma_{\text{av}} = 0.15 \rightarrow 0.29$ (i.e. a decrease in accuracy). A similar large increase in mean is seen for the source age. This may again be due to the nature of the test sources – as the test source age is sampled finely within $\sim 10 - 300$ Myr, an exact match between test and model is not possible in many cases. Of interest, however, is the lack of a large μ_{av} increase for the source angle. This parameter is the most sparsely sampled of those observed with only three sampled values ($0°$, $30°$, and $45°$), whilst the same parameter for the test cases is finely sampled within that space, making an exact match unlikely.

4.3.1   With *a priori* information

Previously, the only constraint placed on the best-fit model was for it to be observed at the same frequency as the test observation as this is the minimum amount of *a priori* information that can be expected. However, it may be possible to place limitations on some observed parameters by inference from other source properties.

The total jet power may be constrained by hotspot luminosity measurements, combined with the redshift z and total linear source size D (Shabala & Godfrey, 2013):

$$\frac{Q}{10^{36} \text{ W}} = 1.5^{+1.8}_{-0.8} (1 + z)^{1.0} \left(\frac{L_{151}}{10^{27} \text{ W Hz}^{-1}} \right)^{0.8} \left(\frac{D}{\text{kpc}} \right)^{0.58 \pm 0.17} \tag{4.9}$$

where L_{151} is the monochromatic hotspot luminosity at 151 MHz. Estimating this parameter is made more difficult by its reliance on source size and redshift as the former is already included in the model as a fitted observable, and the latter may be another parameter of interest. As shown in Figure E.1, the source power is also already well-fitted, and hence the constraints placed on Q would have no impact on which model is identified as the best-fitting in any case.

An alternative constraint may be placed on the source angle with respect to the plane of the sky. Following from Scheuer & Readhead (1979), if the jet-to-counterjet flux density ratio and jet bulk flow velocity are known, then the orientation θ can be estimated assuming the source is symmetric aside from the effects of Doppler beaming (e.g Hocuk & Barthel, 2010):

$$\frac{S_j}{S_{cj}} = \left(\frac{1 + v_j \cos \theta}{1 - v_j \cos \theta} \right)^{2 - \alpha}, \tag{4.10}$$

for jet and counterjet flux densities of S_j and S_{cj} respectively, a jet bulk flow velocity of v_j (in units of c), and spectral index α.

Effective upper limits to the source angle can also be imposed if the visible radio lobes approach and exceed ~ 1 Mpc in projection, classifying them as so-called *giant radio sources* (GRSs). Such large sources are exceptionally rare; the complete Third Cambridge Catalogue of Radio Sources (3CRR) only identifies $\sim 8\%$ as GRSs (Laing et al., 1983), and as of 2018, the most complete catalogue of these objects numbers only 349 (Kuźmicz et al., 2018). The scarcity of these sources, particularly at high redshift, may suggest that a source with a projection length $D > 1$ Mpc is more likely to lie near the plane of the sky. Otherwise, if such a large source were directed at a relatively small angle to the line of sight then the true linear size of the radio source would be so large as to be unrealistic. This reasoning must be treated with caution, however, as the known population of GRSs remains small and poorly sampled for low-power, high-redshift sources (Kuźmicz et al., 2018), despite evidence that GRSs may evolve from otherwise regular, high-power FRIIs. The number of observable low-power GRSs is likely impacted by inverse-Compton losses, which grow to dominate large sources. As the sensitivity of radio surveys increases, it is expected that more sources within the low-power population will be discovered.

GRSs provide another point of interest to this work: such sources are often asymmetric. Saripalli et al. (2005) find that, within a sample of GRSs from the Sydney University Molonglo Sky Survey (SUMSS), nearly 70% of sources have one lobe $> 25\%$ longer than the other, with the shorter of the lobes also predominately being the brightest. These findings are in broad agreement with those of Chapter 2, further supporting the idea that environment plays a significant role in determining the morphology of radio lobes.

With these motivations in mind, constraints are placed onto the angle of the test sources. As these sources are assigned angles randomly sampled from $0° - 45°$ (Table 4.4), they cannot be matched to an exact corresponding model. Instead, these sources are compared only to those

Table 4.6: As in Table 4.5, assuming the source angle θ is well-constrained by additional data.

Parameter [log units] (1)	Without σ_{RM} and H			With σ_{RM} and H			$\frac{P_{RM}}{P_{no\,RM}}$
	$P(\mu)_{av}$ [per dex] (2)	μ_{av} [dex] (3)	σ_{av} [dex] (4)	$P(\mu)_{av}$ [per dex] (5)	μ_{av} [dex] (6)	σ_{av} [dex] (7)	(8)
t_{age}	0.50	-0.05	0.80 ± 0.08	1.18	-0.30	0.48 ± 0.12	2.34
Q	0.99	0.04	0.40 ± 0.01	1.02	0.05	0.39 ± 0.03	1.03
M_{200}	0.07	0.15	5.64 ± 1.80	0.53	0.27	0.75 ± 0.24	7.56

Table 4.7: As in Table 4.5, assuming the galaxy cluster dark matter halo mass M_{200} is well-constrained by additional data.

Parameter [log units] (1)	Without σ_{RM} and H			With σ_{RM} and H			$\frac{P_{RM}}{P_{no\,RM}}$
	$P(\mu)_{av}$ [per dex] (2)	μ_{av} [dex] (3)	σ_{av} [dex] (4)	$P(\mu)_{av}$ [per dex] (5)	μ_{av} [dex] (6)	σ_{av} [dex] (7)	(8)
t_{age}	0.51	-0.04	0.80 ± 0.08	0.79	-0.24	0.52 ± 0.08	1.56
θ	~ 0	~ 0	3535.82 ± 283.04	1.75	-0.02	0.23 ± 0.08	1.58×10^4
Q	0.99	0.04	0.40 ± 0.01	1.00	0.05	0.40 ± 0.02	1.01

models which have angles that are nearest to the true value. In the case of test "12_01" with $\theta = 32°$, only those models with $\theta = 30°$ are compared with as this is the nearest of the three discrete values possible for the models ($0°$, $30°$, and $45°$). Significant improvements are seen for the increase in confidence with RM for the source age and halo mass, with the former increasing from $P_{RM}/P_{no\,RM} = 1.48 \pm 0.10$ to 2.34 ± 0.09, and the latter from 6.16 ± 0.07 to 7.56 ± 0.06 (Table 4.6, Figure 4.10). There is no added improvement for the jet power, as expected.

The only other modelled parameter which may reasonably be inferred from additional data sets is that of the dark matter halo mass M_{200}, which is typically estimated from X-ray observations (Section 1.2.2). Difficulties arise both at high redshift and for faint radio sources, however it may be sufficient to constrain the cluster gas mass within a factor of 0.25 dex, which is the spacing of M_{200} in this work.
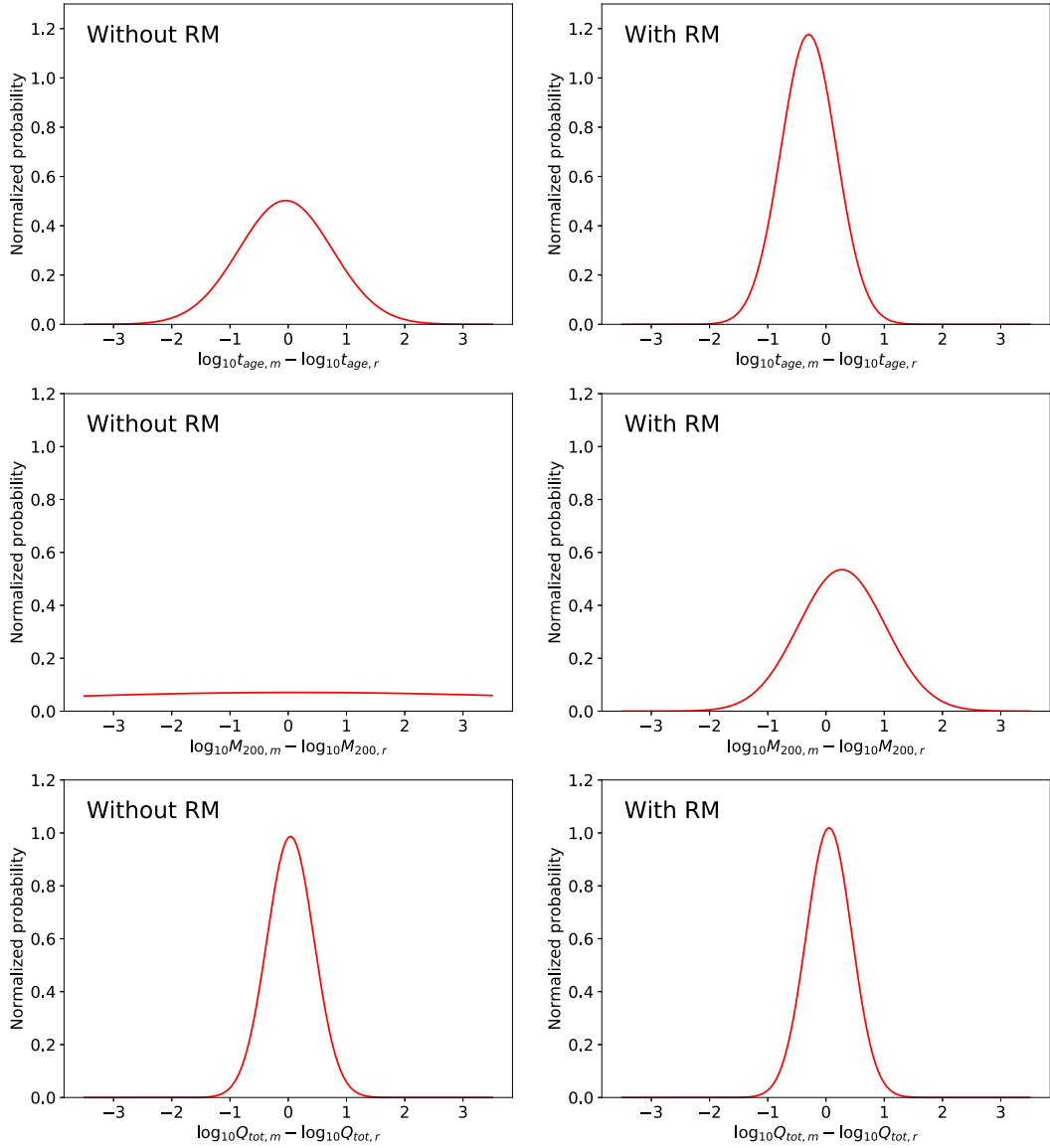
Figure 4.10: The average log difference relative-probability distribution between (*from top to bottom*) observed and model source ages, environment dark matter halo masses, and jet powers, both when RM parameters are not included in the χ^2 model (*left*) and when they are (*right*). There is assumed to be *a priori* knowledge of the source angle θ.
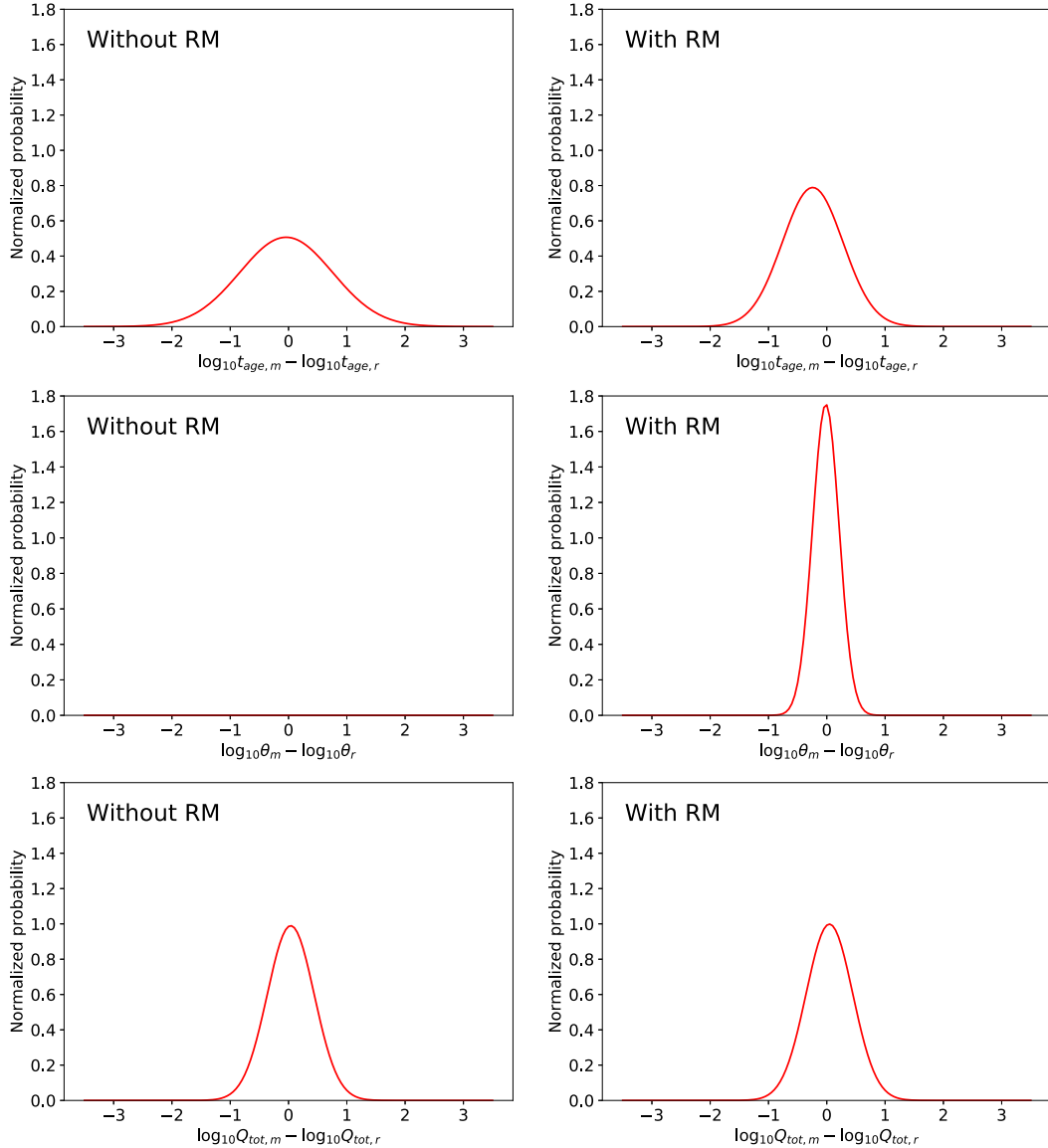
Figure 4.11: The average log difference relative-probability distribution between (*from top to bottom*) observed and model source ages, source angles, and jet powers, both when RM parameters are not included in the χ^2 model (*left*) and when they are (*right*). There is assumed to be *a priori* knowledge of the cluster dark matter halo mass M_{200}.

Similarly to source angle, having *a priori* information on the halo mass does appear to significantly impact the efficacy of parameter estimation. Barring jet power, parameters are fit more accurately and more precisely when mass information is included alongside RM metrics, than if only RM metrics are used (Table 4.7, Figure 4.11). The source angle sees the greatest improvement on the fractional increase of the confidence of the fit, going from $P_{RM}/P_{\text{no }RM} = 1.38 \times 10^4$ (for RM only) to 1.58×10^4 (for RM and constraint on M_{200}). The fit to the source age also sees improvement when a constraint is placed on the halo mass, however this change is within the errors on the values (from 1.48 ± 0.10 to 1.56 ± 0.11).

4.4 Conclusions

In this chapter, source properties from the *Radio AGN in Semi-analytic Environments* model (RAiSE; Turner & Shabala, 2015) were combined with the final model of Chapter 3 in order to investigate the utility of Faraday Rotation and Rotation Measure (RM) in constraining source and environment parameters. The RAiSE dynamical model gave the radio observables of luminosity L_ν and total linear source length D, alongside other intermediate values of importance for scaling the source magnetic field and density, up to an age of $t_{\text{age}} = 1$ Gyr (Section 4.1). This model was computed for source powers of $\log Q = 10^{37} - 10^{39}$ W (spaced by 0.25 dex) and angles of $\theta = 0°$, $30°$, and $45°$, embedded within environments of halo mass $M_{200} = 10^{12} - 10^{14}$ $M_\odot$ (spaced by 0.25 dex), and observed at frequencies of $\nu = 204$, 232, and 1400 MHz. These sources are then taken at discrete ages of $t_{\text{age}} = 10$, 30, 100, and 300 Myr. Altogether, this produced a sample of 972 unique models; 2916 when each frequency is counted independently. In addition to the luminosity and source length, observables for the RM standard deviation (σ_{RM}) and change in standard deviation (heteroscedasticity, H) were calculated, culminating in four possible observables with which to identify a given model.

In this thesis, it has been hypothesised that an estimation of the model parameters of M_{200}, Q, θ, and t_{age} will be less accurate when matching an observed source only on L_ν and D than when matching over L_ν, D, σ_{RM}, and H combined. To test this hypothesis, 135 random test models are produced in Section 4.2 from within the same parameter spaces as the model population. This subsample is then compared to each of the models in the larger population by a χ^2-test, and the relative probabilities of each match are used to construct a log-difference distribution (Section 4.3).

The greatest improvements introduced by the inclusion of the RM metrics are seen for the source angle and cluster dark matter halo mass, with the fits' accuracy (to within a small log-scale tolerance) increased by factors of $P_{RM}/P_{\text{no }RM} = 13764.57$ and 6.16 ± 0.07, respectively (Table 4.5). The source age sees a fractional increase in confidence of 1.48 ± 0.10, however, fits to the source age must be interpreted with caution as these parameters are sparsely sampled in 0.5 dex for the model population, making marginalisation over these parameters not possible. To reduce the impact of this sparse sampling, a Gaussian-fitting method has been used.

In Section 4.3.1, the tests of Section 4.3 were repeated with successive *a priori* information constraining the source angle and halo mass, respectively. Forcing the source angle to the nearest model value sees a small change in the increase in confidence from $P_{RM}/P_{\text{no }RM} = 1.48 \pm 0.10$

to 2.34±0.09 for the source age and 6.16±0.07 to 7.56±0.06 for the halo mass, but has marginal effect on the jet power. When *a priori* information is assume for the halo mass, improvements in confidence between the "RM" and "no RM" models only for the source angle (13764.57 to 15771.01), although this value is poorly constrained when RM metrics are not used, suggesting that the model is failing to accurately identify the source angle. It is promising, however, to see such improvements on this parameter with the inclusion of the RM metrics of σ_{RM} and H as these are parameters most likely to see the effects of the Laing-Garrington effect, which supports its use as a method to constrain the properties of radio sources and their surrounding environments.

CHAPTER 5

Conclusion

Presented in this work is a series of analytical models for the gas distribution and magnetic field strength in galaxy clusters and the radio-frequency-emitting structures inflated by supermassive black hole jets, and a study of the impact of the surrounding environment on the properties of radio source morphology. The purpose of this analysis was to investigate depolarisation and Faraday Rotation as additional methods alongside X-ray observations to measure the properties of intra-cluster gas and of an embedded radio source. This is an important addition as X-ray observations alone cannot constrain all of the parameters for an AGN jet or AGN feedback model.

Using a sample of nearby, large radio sources consisting of 16 FR-II objects, 6 FR-Is and one hybrid morphology source, the impact of environment on radio lobe morphology was investigated (Chapter 2). For the FR-II population, it was found that the lobe length is strongly negatively correlated (significant to the 4σ level) with the density of the environment, as measured by the number density of surrounding galaxies in 1 Mpc projected. Additionally, the luminosity of FR-II sources is moderately negatively correlated (significant to the 2σ level) with the lobe length, although there is no statistically significant correlation between luminosity and number density of nearby galaxies. These results are in agreement with analytical models (e.g. Kaiser & Alexander, 1997; Turner & Shabala, 2015), and demonstrate the power of utilising galaxy clustering data as a proxy for surrounding gas density. They also highlight the need for greater understanding of these environments, with Faraday Rotation measures likely playing a key role within the next decade.

Computationally tractable models including only the essential physics were generated for the thermal electron number density n_{e} and magnetic field distributions $\underline{B}$ of galaxy clusters, beginning first with the trivial case of both being constant. These were then evolved to increasingly realistic distributions, all placed at a redshift of $z = 0$ and for a telescope beam size corresponding to the maximum resolution of the simulations (Section 3.2). Radio sources were placed within these environments at angles to the plane of the sky of 0, 30, and 45 degrees, and the Rotation Measure (RM) of the inflated lobes was calculated for each incident line of sight (Section 3.3). RM distributions of early models with constant field strengths suggested that the thermal electron number density plays a vital role towards producing slopes in RM across a ra-

dio source, although the magnetic field distribution dominates for the preferential depolarisation of a source's far lobe – this is seen as the emergence of the Laing-Garrington effect.

The most complex models of n_e and $\underline{\boldsymbol{B}}$ for both the cluster and radio source were combined with radio sources parameters simulated by the *Radio AGN in Semi-analytic Environments* model (RAiSE; Turner & Shabala, 2015) and evolved up to an age of $t_{age} \sim 1000$ Myr. A sample of 972 unique models was produced from the parameter spaces for jet power Q, source age t_{age}, source orientation θ, and dark matter halo mass M_{200}, for which mock observations were generated for three separate frequencies corresponding to those of existing VLA surveys ($\nu = 1.4$ GHz) and for the next generation of radio telescopes ($\nu = 204 - 232$ MHz). The RM distribution was determined, and radio observables of luminosity L_ν, projected total linear size D, RM dispersion σ_{RM}, and the change in RM dispersion along the projected jet axis (the heteroscedasticity, H) were characterised (Section 4.1).

To test the efficacy of Faraday Rotation measurements such as the RM in helping to constrain the properties of radio lobe and their surrounding environment, a series of test cases were sampled from the same parameter space as the population of known models (Section 4.2). Maximum likelihood parameter estimation either including or excluding σ_{RM} and H was then performed on each of the test cases, and a best-fit model was determined (Section 4.3). It was found that including measures of the RM distribution when fitting a random source to a model identifies fits that are more precise but less accurate, although the decrease in accuracy is likely attributed to the sparse sampling of parameter spaces. The source power proved to be the most easily fit with 100% of test cases matched to a model with the same jet power regardless of the inclusion of RM metrics. The most significant improvements using RM metrics was seen in the source angle, which a fractional increase in confidence in the identified best-fit model of 1.38×10^4. This was followed by the cluster halo mass, with a fractional increase in confidence in the identified best-fit model of 6.16 ± 0.07. Including *a priori* information on the galaxy cluster dark matter halo mass in addition to RM metrics acts to constrain the source angle even greater than for the case without the constraint on halo mass, and so whilst Faraday Rotation may assist in determining environment properties, it is still best augmented by X-ray data where available. Alternatively, including *a priori* information for the source angle leads to a fractional increase in confidence in the identified best-fit model for source age of 2.34 ± 0.09 and for halo mass of 7.56 ± 0.06.

Further investigation into the limits of this model and its efficacy in predicting source and environment parameters requires a more finely-sampled set of parameter spaces. Of key interest is the source power as this parameter was consistently fit so well. Whether this is a function of the wide bins for this parameter or whether the model is indeed the most sensitive to this variable is not known, although the many relationships between source power, linear size, angle, and luminosity keep the jet power poised to dictate the final best-fit model. Such connections between observables (e.g. Shabala & Godfrey, 2013) may enable the redshift to be constrained, and the addition of the two RM metrics discussed in this work may assist in determining both the redshift and the host galaxy mass in AGN surveys where only radio-frequency observations are available (Turner, 2019).

This work has made numerous simplifying assumptions, however. Firstly, the environment and embedded radio source are located at a redshift of $z \sim 0$. A zero and constant redshift in the sample simplifies calculations for source size and minimises the complexity of inverse-Compton

and synchrotron losses, but it also prevents consideration of the intervening medium. For actual radio sources placed at $z \gg 0$, radiation emitted from the radio lobes intersect the cluster environment and multiple other segments of magnetised media before arriving at an Earth telescope (Section 1.3). This will potentially lead to greater depolarisation, although the precise distribution of these nearby magnetic fields will play an important role in determining whether the effect is global and simply adds noise, or whether the RM distribution will become biased. A low redshift also reduces the dependence of the RM distribution on the particular telescope or array used in observations as the beam size remains small. At high redshift, large beam sizes will average many smaller RM contributions into one and lead to beam depolarisation. As a key parameter in this work is the RM heteroscedasticity, which measures the change in the variance of the RM, beam depolarisation could significantly reduce the model's ability identify a match accurately. Whilst the capability exists to run the models in this work at a higher redshift, they are not expected to fare as well within this model, and must also be compared to observations of real systems. The smaller physical and surface brightness of higher redshift sources would likely prevent this model from working effectively.

For the next generation of radio telescopes, arrays, and surveys, a large influx of low-luminosity and high-redshift radio sources will provide more data to which this work can be directly applied (Section 1.4). In the absence of any other source of information on these parameters, this work shows the potential for polarisation studies and Faraday Rotation from black hole jets in constraining both source and environment properties. When combined with additional limitations from independent sources, the efficacy of parameter estimation can be improved even more. When environment parameters can be estimated directly from observations of radio jets alone, that environment might be better understood along with its effects on radio source evolution and morphology.

APPENDIX A

FR-II radio and optical images
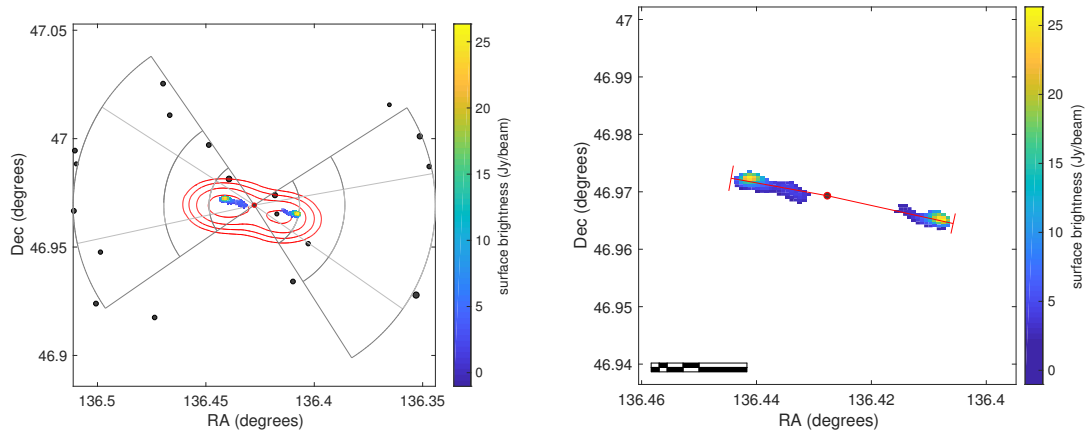
Figure A.1: FR-II source RGZ J090542.6+465809; symbols are as in Figure 2.1.
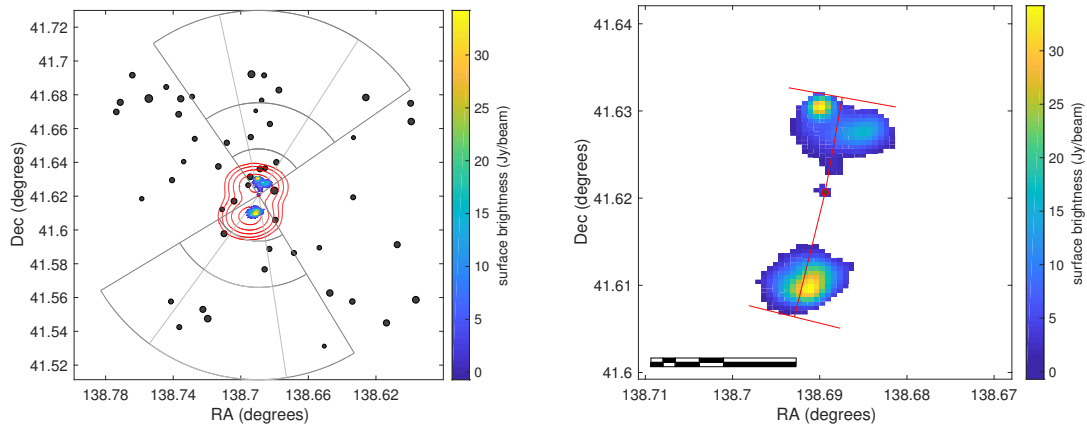
Figure A.2: FR-II source RGZ J091445.5+413714; symbols are as in Figure 2.1.
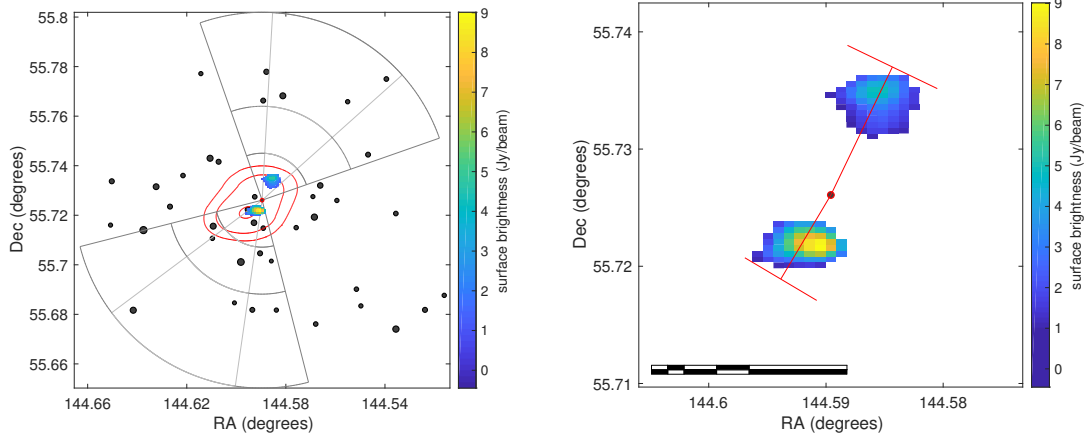
Figure A.3: FR-II source RGZ J093821.5+554333; symbols are as in Figure 2.1.
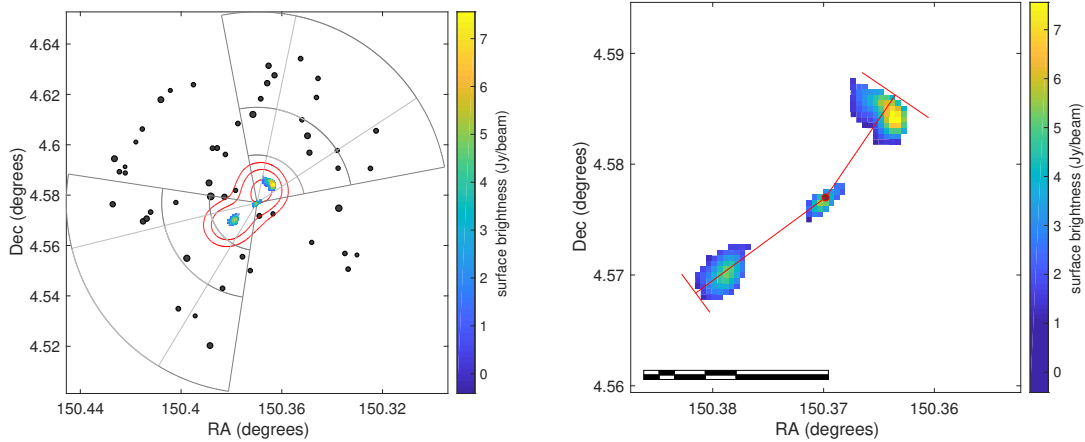
Figure A.4: FR-II source RGZ J100128.8+043437; symbols are as in Figure 2.1.
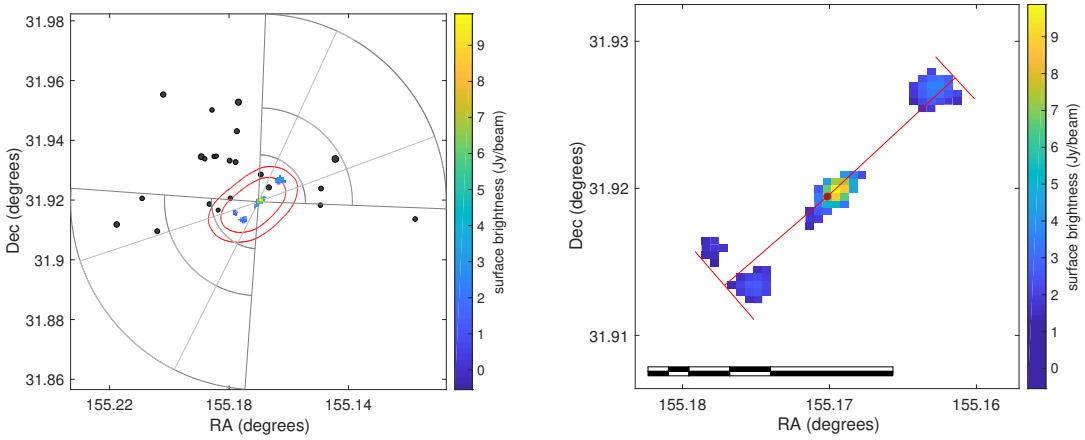
Figure A.5: FR-II source RGZ J102040.8+315509; symbols are as in Figure 2.1.
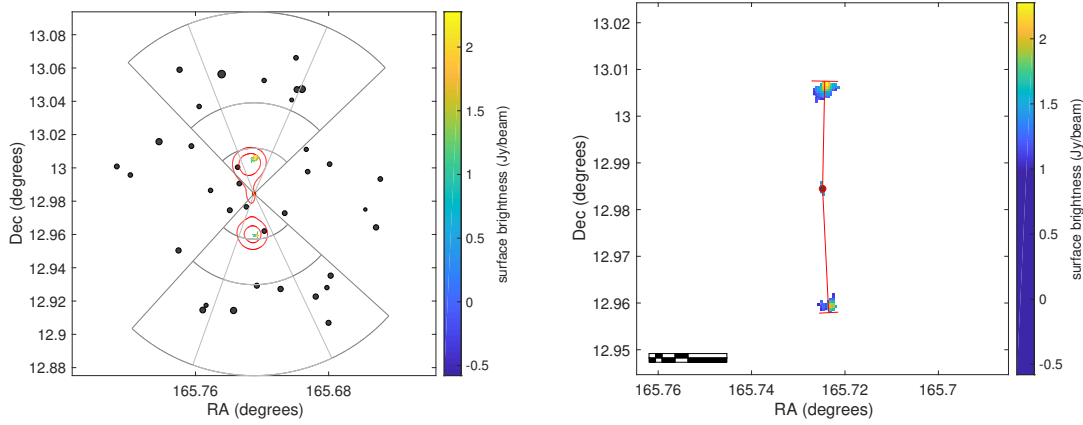
Figure A.6: FR-II source RGZ J110254.0+125904; symbols are as in Figure 2.1.
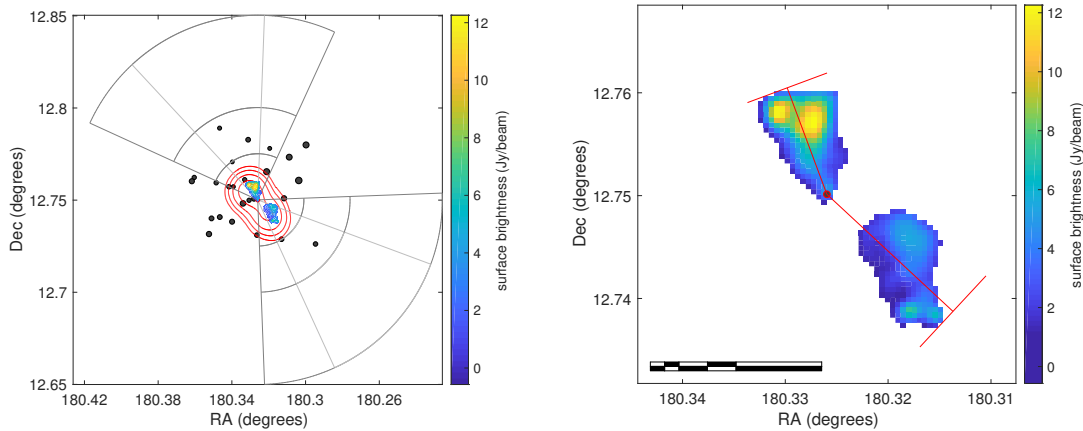
Figure A.7: FR-II source RGZ J120118.2+124500; symbols are as in Figure 2.1.
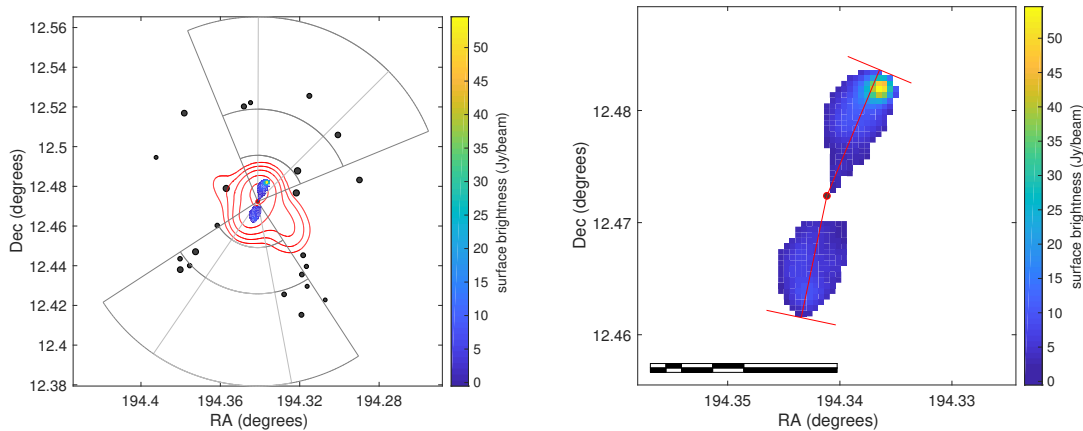
Figure A.8: FR-II source RGZ J125721.9+122820; symbols are as in Figure 2.1.
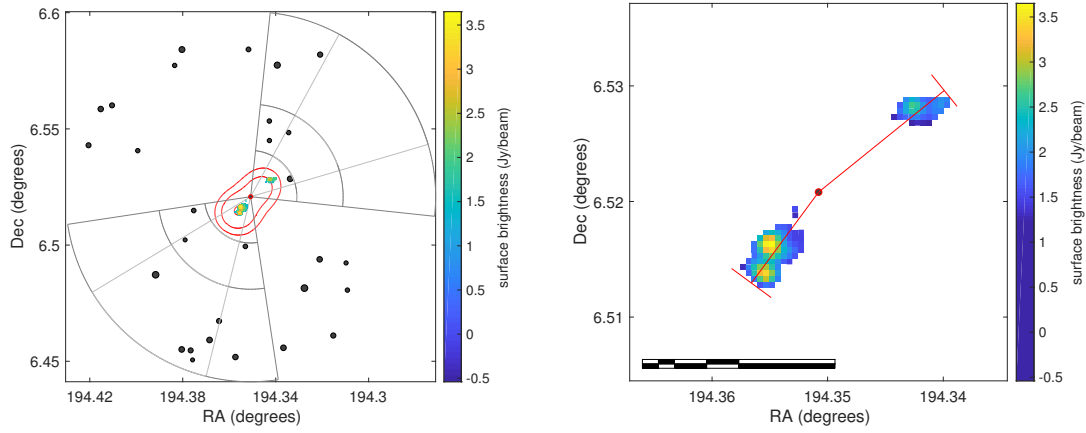
Figure A.9: FR-II source RGZ J125724.2+063114; symbols are as in Figure 2.1.
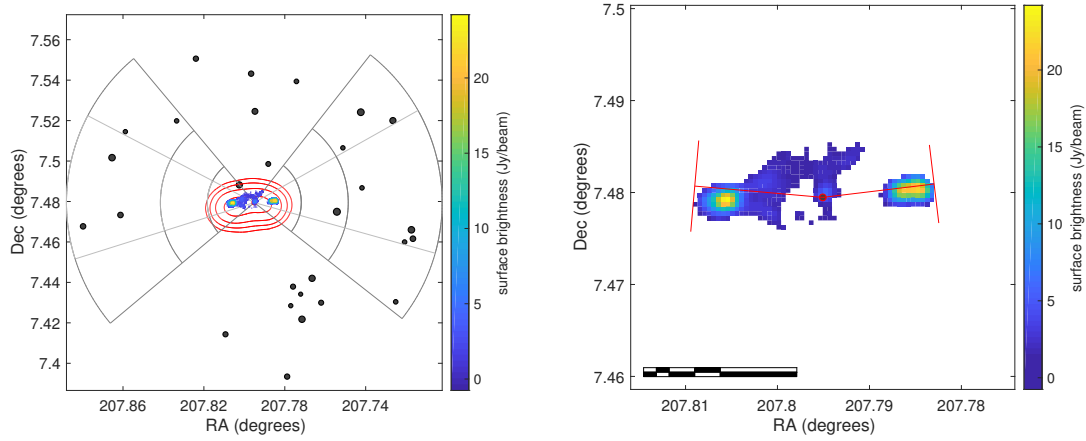
Figure A.10: FR-II source RGZ J135110.8+072846; symbols are as in Figure 2.1.
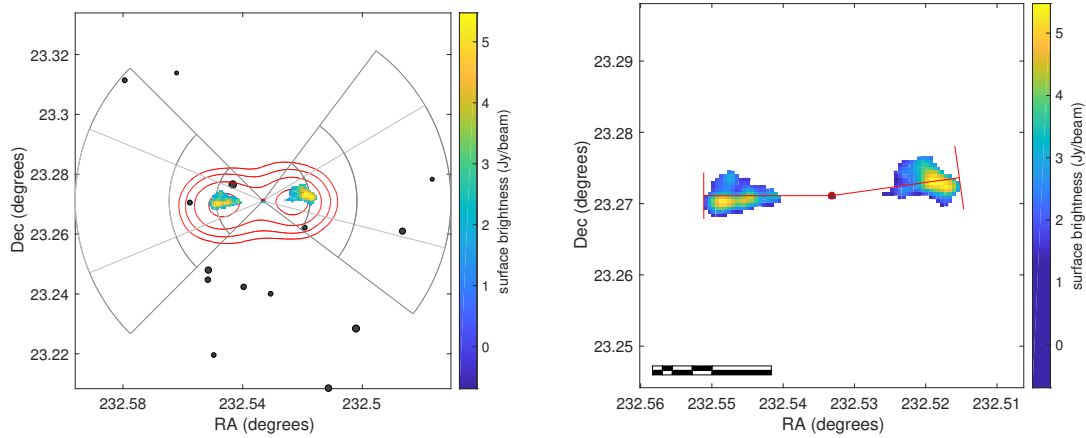
Figure A.11: FR-II source RGZ J153008.0+231616; symbols are as in Figure 2.1.
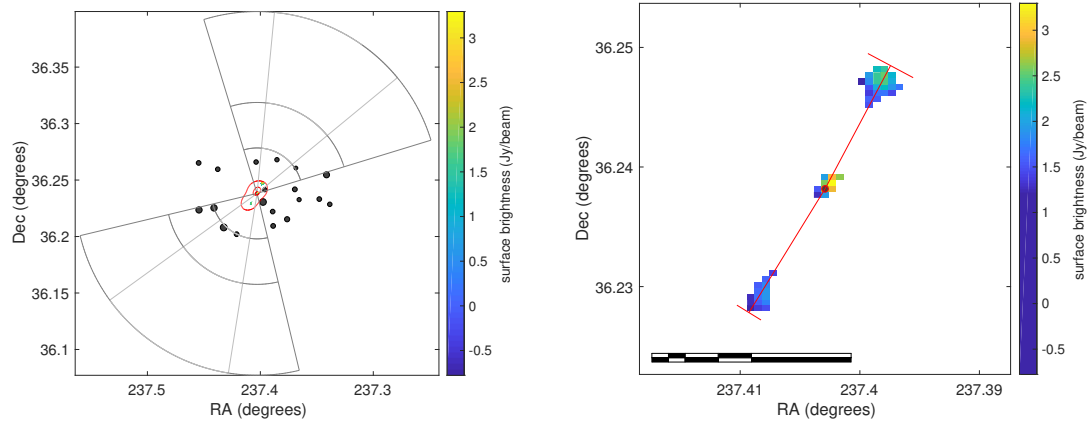
Figure A.12: FR-II source RGZ J154936.7+361417; symbols are as in Figure 2.1.
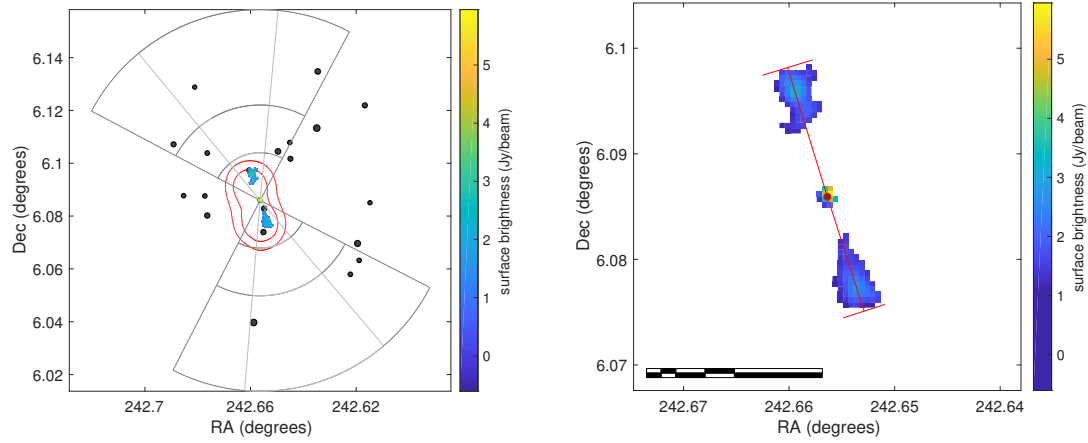
Figure A.13: FR-II source RGZ J161037.5+060509; symbols are as in Figure 2.1.
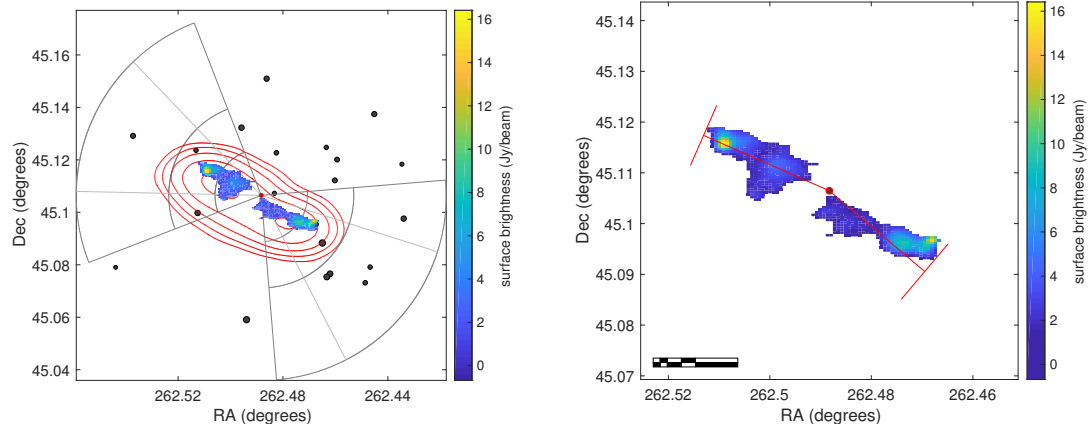
Figure A.14: FR-II source RGZ J172957.2+450623; symbols are as in Figure 2.1.
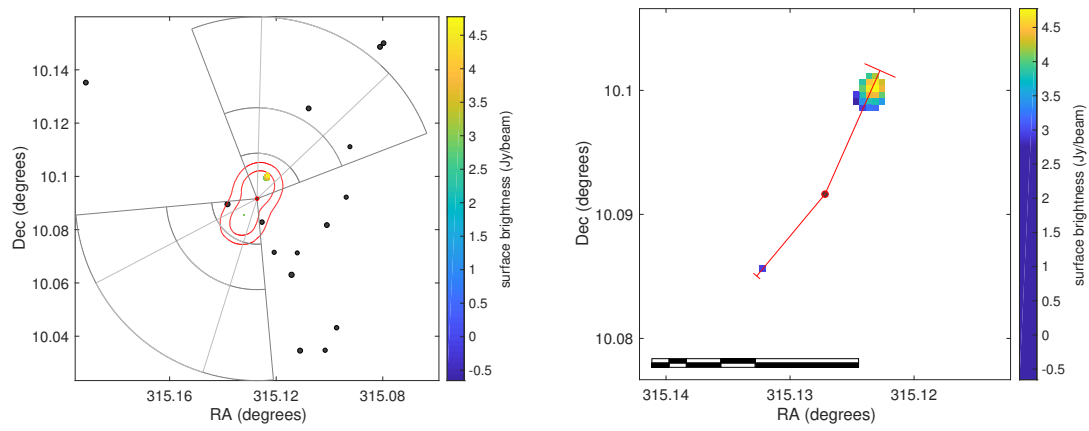
Figure A.15: FR-II source RGZ J210030.5+100529; symbols are as in Figure 2.1. This is the only FR-II source excluded from analysis, due to its hotspot dominance of integrated lobe luminosity.

APPENDIX B

FR-I radio and optical images
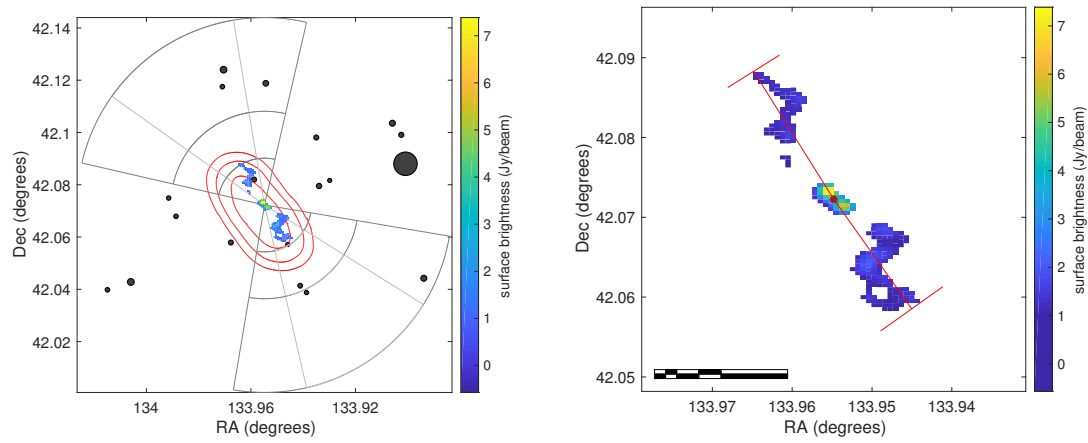
Figure B.1: FR-I source RGZ J085549.1+420420; symbols are as in Figure 2.1.
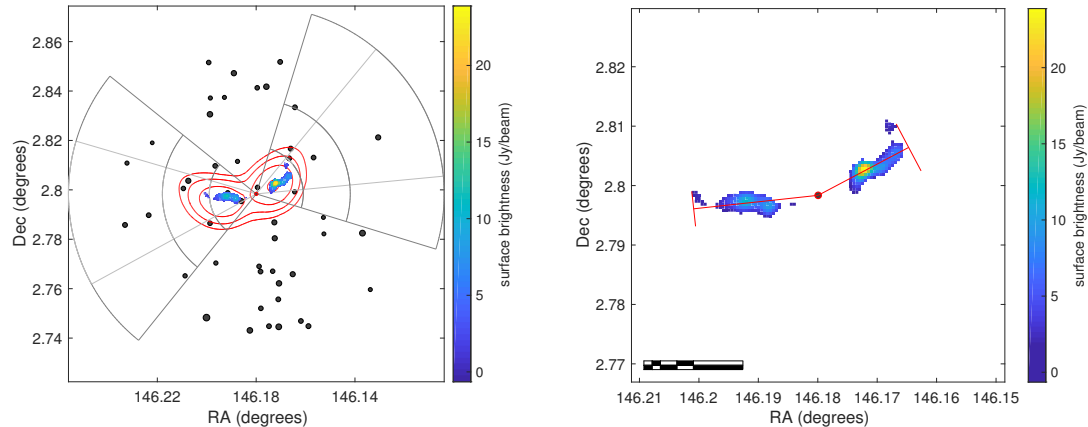
Figure B.2: FR-I source RGZ J094443.2+024754; symbols are as in Figure 2.1.
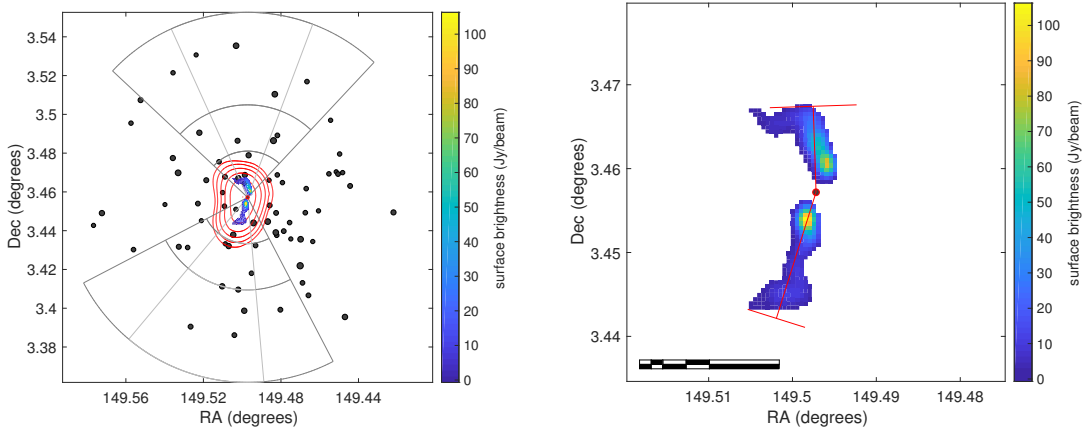
Figure B.3: FR-I source RGZ J095759.3+032725; symbols are as in Figure 2.1.
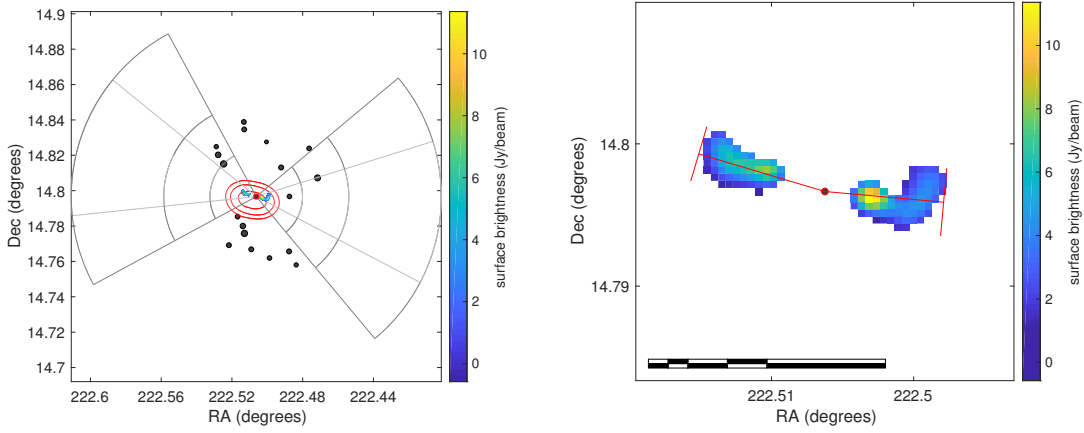
Figure B.4: FR-I source RGZ J145001.5+144747; symbols are as in Figure 2.1.
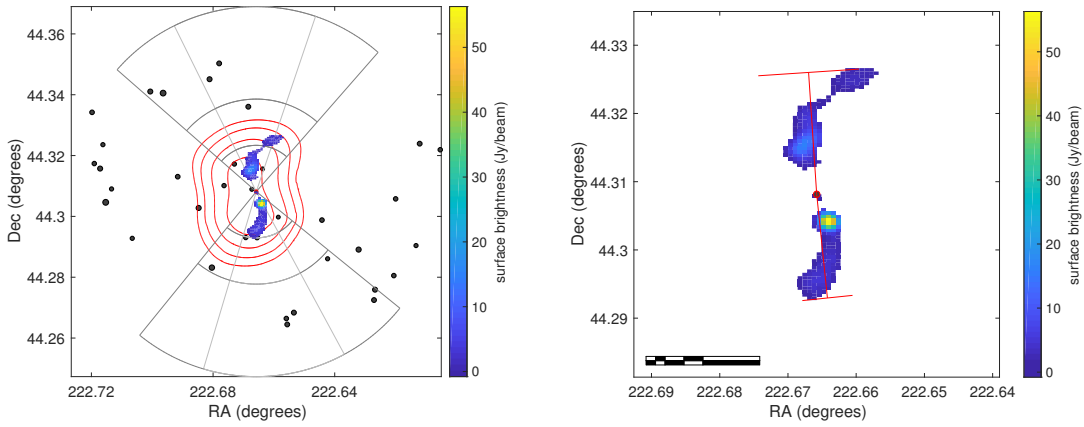
Figure B.5: FR-I source RGZ J145039.8+441829; symbols are as in Figure 2.1.

Additional Cluster Configurations
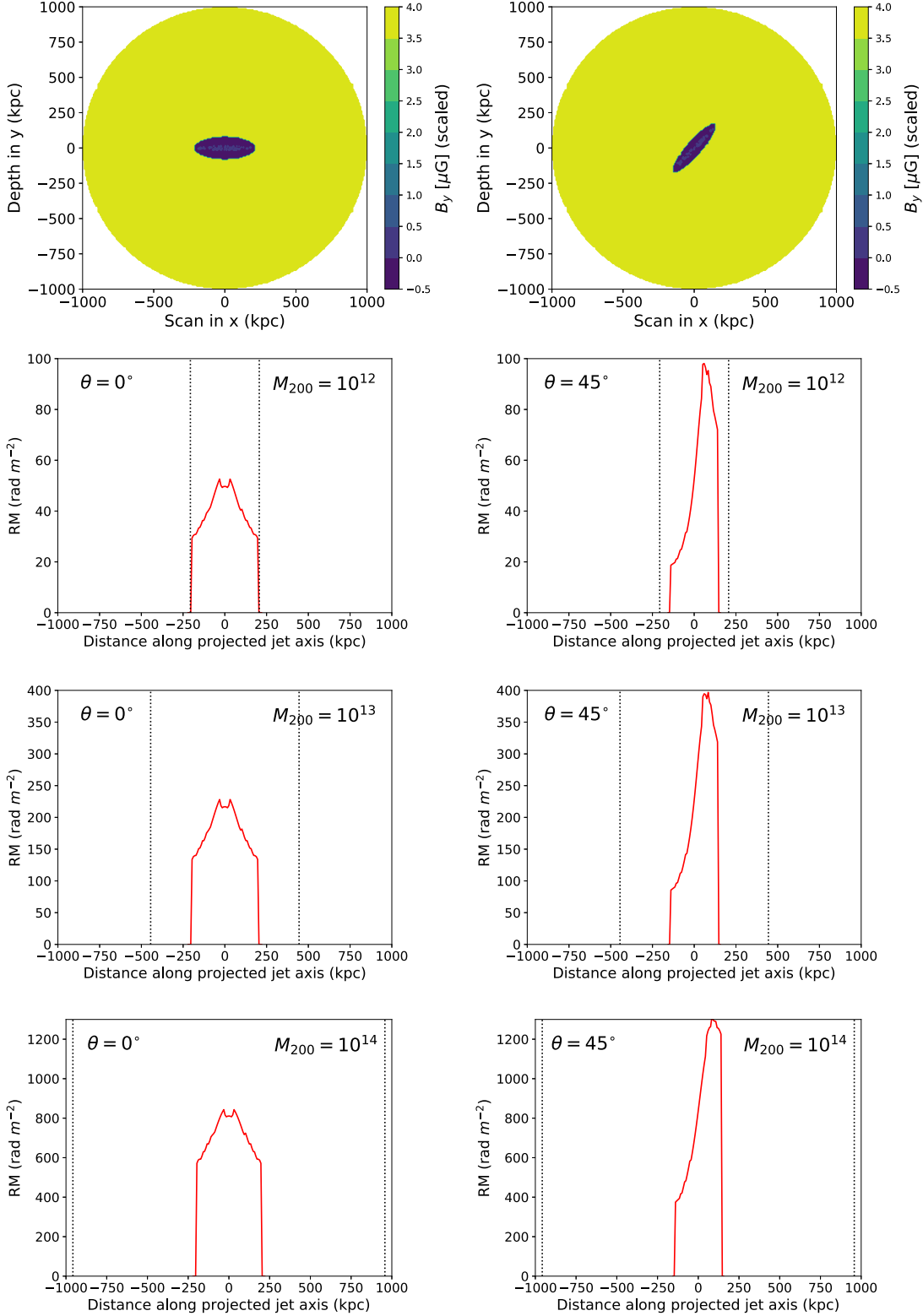
Figure C.1: (*Top*): Magnetic field slice as in Figure 3.12. (*Upper middle – bottom*) *RM* distributions for halo dark matter masses of $10^{12} M_\odot$, $10^{13} M_\odot$, and $10^{14} M_\odot$ respectively. Whilst the shape remains approximately constant, higher dark matter halos lead to larger core radii as shown by the black-dotted lines, thus giving greater and broader density profiles and correspondingly altered *RM* values.
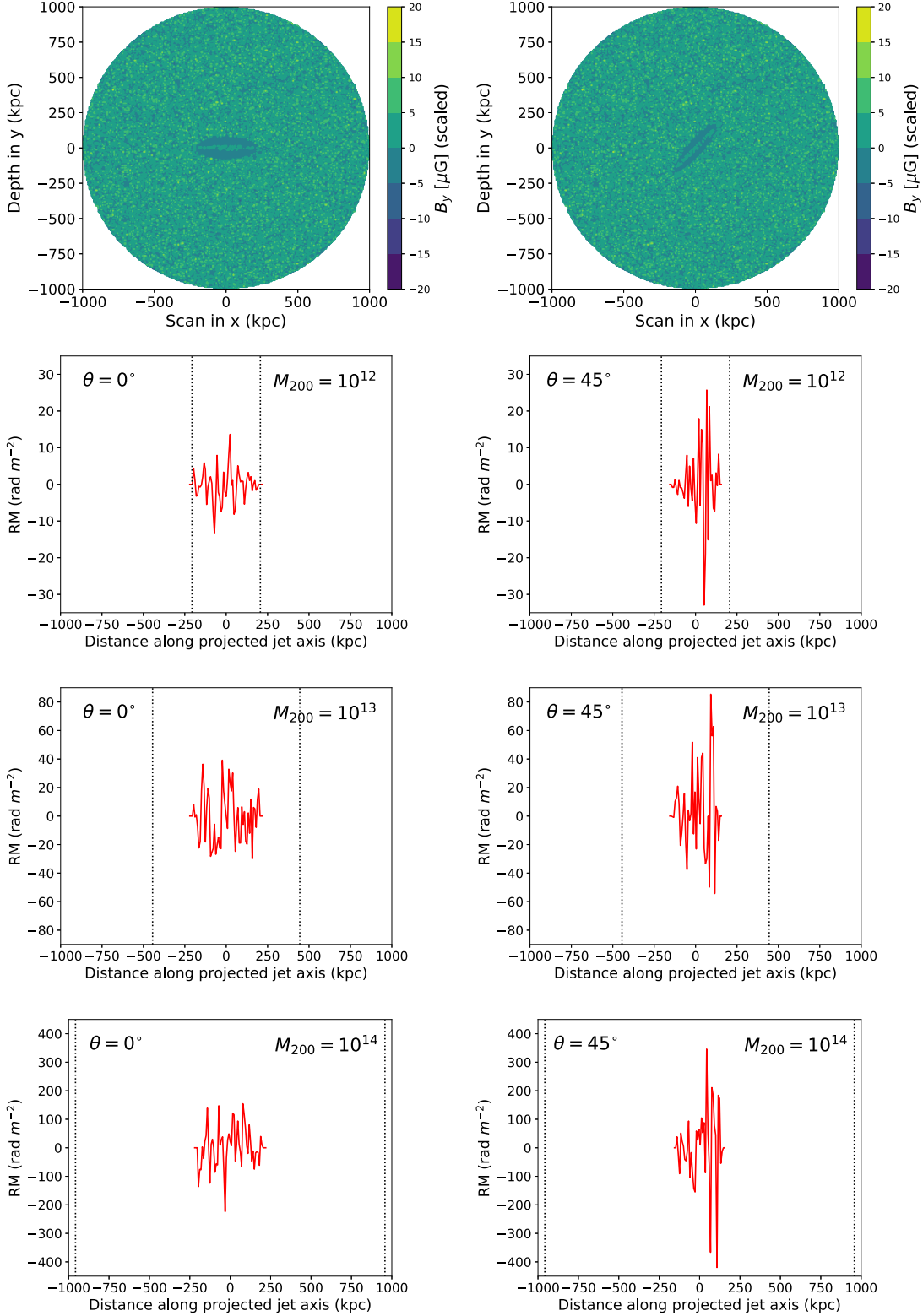
Figure C.2: As in Figure C.1, but with the normal random magnetic field from Section 3.3.2
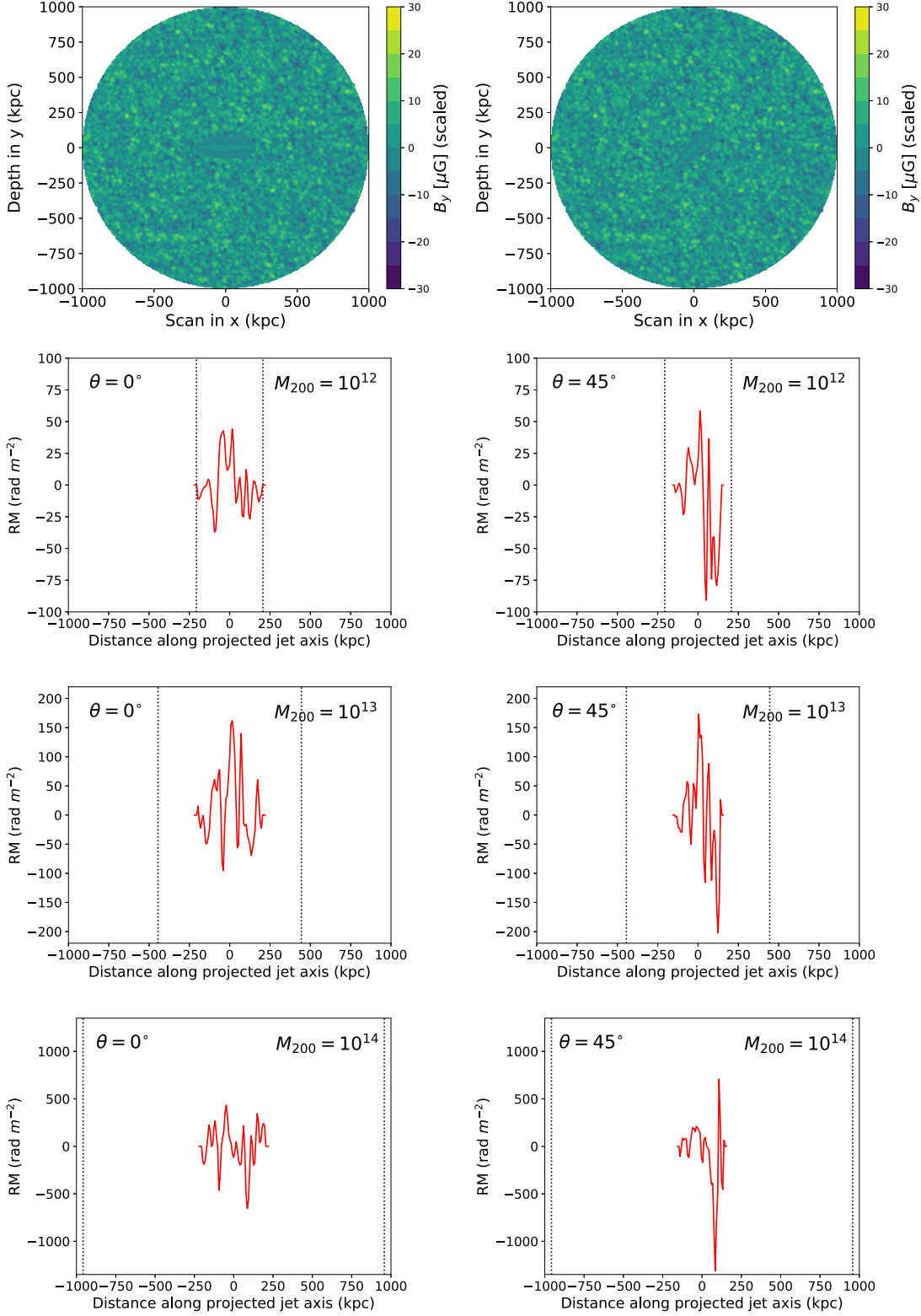
Figure C.3: As in Figure C.1, but with the Fourier spaced magnetic field from Section 3.3.2

APPENDIX D

# Heteroscedasticity in other environments
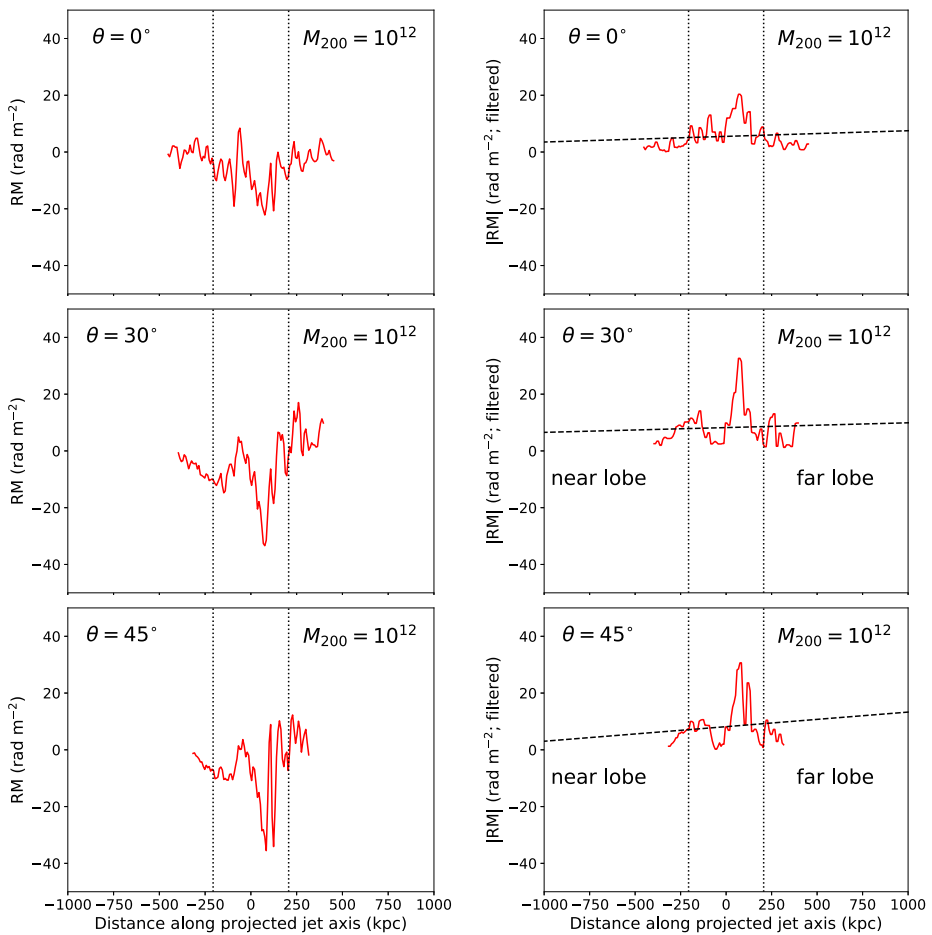
Figure D.1: As in Figure 4.5, but for an $M_{200} = 10^{12}$ $M_{\odot}$ environment.
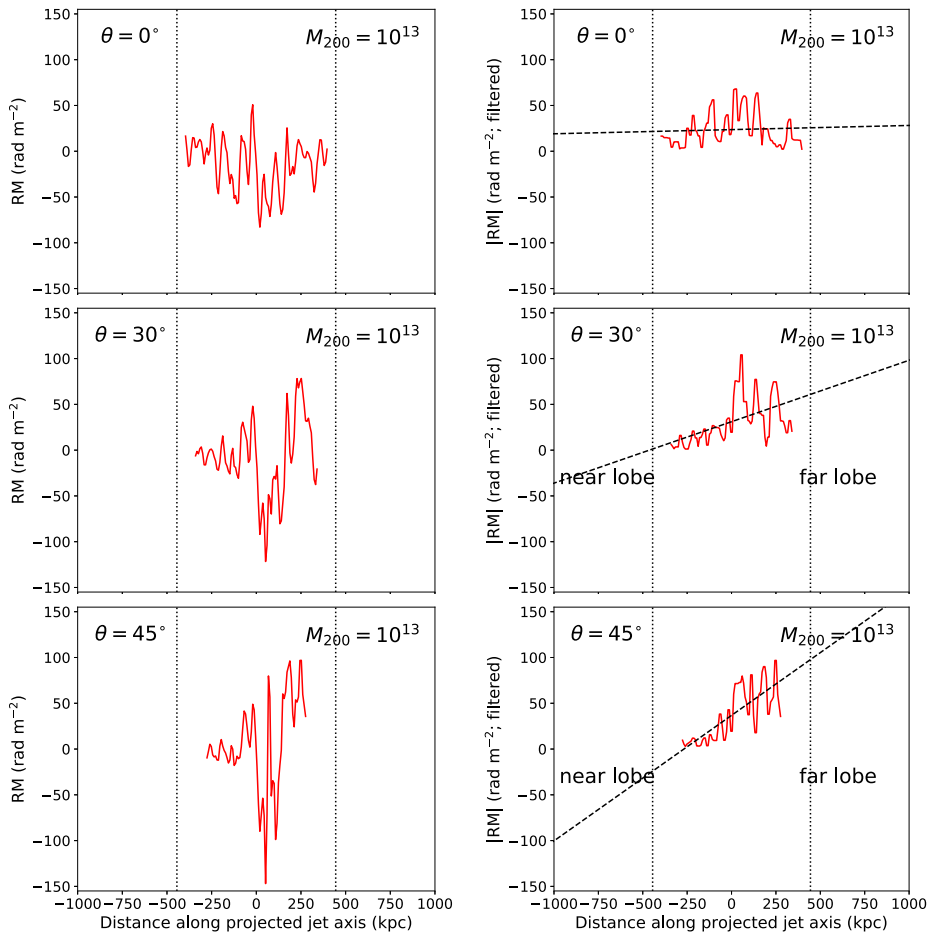
Figure D.2: As in Figure 4.5, but for an $M_{200} = 10^{13}$ $M_\odot$ environment.

Log-difference histograms
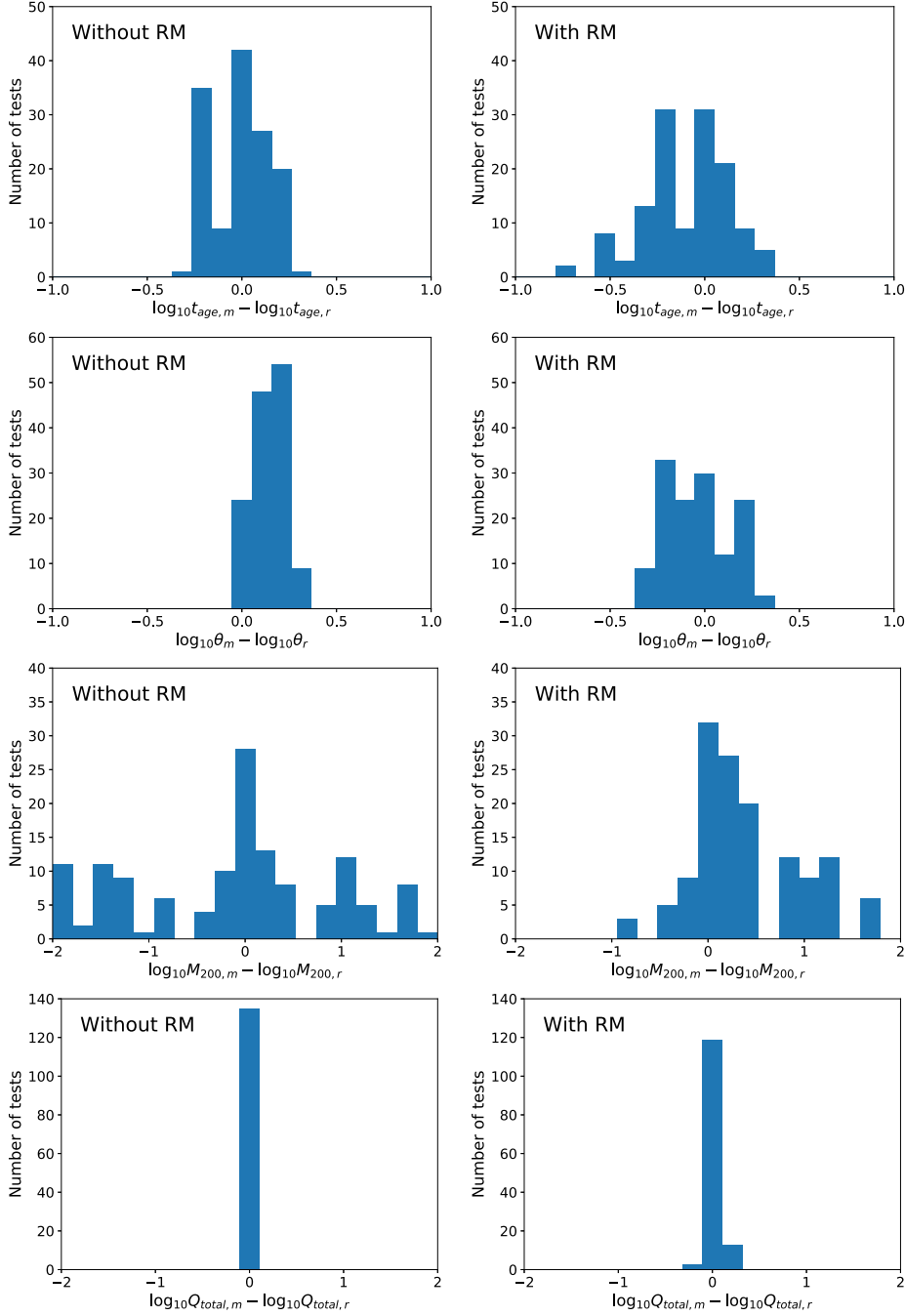
Figure E.1: The log difference between the best-fit model and a series of observed sources for the parameters of (*from top to bottom*) source age, source angle, environment dark matter halo mass, and jet power. (*Left*): The χ^2 not including measures for RM and H. (*Right*): Including RM and H in χ^2.

BIBLIOGRAPHY

Abazajian K. N., et al., 2009, ApJs, 182, 543

Aihara H., et al., 2011, ApJs, 193, 29

Akahori T., Gaensler B. M., Ryu D., 2014, ApJ, 790, 123

Alexander P., 2006, MNRAS, 368, 1404

Alger M., et al. 2018, Submitted to MNRAS

Allen S. W., Dunn R. J. H., Fabian A. C., Taylor G. B., Reynolds C. S., 2006, MNRAS, 372, 21

Arnaud M., Neumann D. M., Aghanim N., Gastaud R., Majerowicz S., Hughes J. P., 2001, A&A, 365, L80

Arnaud M., Pratt G. W., Piffaretti R., Böhringer H., Croston J. H., Pointecouteau E., 2010, A&A, 517, A92

Arora B. S., et al., 2016, PASA, 33, 14

Baldi R. D., Capetti A., Giovannini G., 2015, A&A, 576, A38

Baldry I. K., et al., 2010, MNRAS, 404, 86

Bambic C. J., Morsony B. J., Reynolds C. S., 2018, ApJ, 857, 84

Banfield J. K., et al., 2015, MNRAS, 453, 2326

Banfield J. K., et al., 2016, MNRAS, 460, 2376

Becker R. H., White R. L., Helfand D. J., 1995, ApJ, 450, 559

Begelman M. C., Cioffi D. F., 1989, ApJl, 345, L21

Benson A. J., Babul A., 2009, MNRAS, 397, 1302

Bernardi G., et al., 2013, ApJ, 771, 105

Best P. N., 2009, Astronomische Nachrichten, 330, 184

Best P. N., Heckman T. M., 2012, MNRAS, 421, 1569

Best P. N., Kauffmann G., Heckman T. M., Brinchmann J., Charlot S., Ivezić vZ., White S. D. M., 2005, MNRAS, 362, 25

Best P. N., von der Linden A., Kauffmann G., Heckman T. M., Kaiser C. R., 2007, MNRAS, 379, 894

Bicknell G. V., 1995, ApJs, 101, 29

Bicknell G. V., Dopita M. A., O'Dea C. P. O., 1997, ApJ, 485, 112

Birkinshaw M., Hughes J. P., 1994, ApJ, 420, 33

Bîrzan L., McNamara B. R., Nulsen P. E. J., Carilli C. L., Wise M. W., 2008, ApJ, 686, 859

Blandford R. D., Königl A., 1979, ApJ, 232, 34

Blandford R. D., Levinson A., 1995, ApJ, 441, 79

Blandford R. D., Payne D. G., 1982, MNRAS, 199, 883

Blandford R. D., Rees M. J., 1974, MNRAS, 169, 395

Blandford R. D., Znajek R. L., 1977, MNRAS, 179, 433

Blundell K. M., Rawlings S., 2000, AJ, 119, 1111

Blundell K. M., Rawlings S., Willott C. J., 1999, AJ, 117, 677

Bonchi A., La Franca F., Melini G., Bongiorno A., Fiore F., 2013, MNRAS, 429, 1970

Bondi H., 1952, MNRAS, 112, 195B

Bourne M. A., Sijacki D., 2017, MNRAS, 472, 4707

Bower R. G., Benson A. J., Malbon R., Helly J. C., Frenk C. S., Baugh C. M., Cole S., Lacey C. G., 2006, MNRAS, 370, 645

Bryan G. L., Norman M. L., 1998, ApJ, 495, 80

Burn B. J., 1966, MNRAS, 133, 67

Burns J. O., 1990, AJ, 99, 14

Buttiglione S., Capetti A., Celotti A., Axon D. J., Chiaberge M., Macchetto F. D., Sparks W. B., 2010, A&A, 509, A6

Capaccioli M., Mancini D., Sedmak G., 2005, The Messenger, 120, 10

Carilli C. L., Harris D. E., 1996, Cygnus A - Study of a Radio Galaxy. Cambridge University Press

Carilli C. L., Taylor G. B., 2002, ARA&A, 40, 319

Cattaneo A., Best P. N., 2009, MNRAS, 395, 518

Cavaliere A., Fusco-Femiano R., 1976, A&A, 49, 137

Churazov E., Brüggen M., Kaiser C. R., Böhringer H., Forman W., 2001, ApJ, 554, 261

Cielo S., Bieri R., Volonteri M., Wagner A. Y., Dubois Y., 2018, MNRAS, 477, 1336

Clarke T. E., Kronberg P. P., Böhringer H., 2001, ApJ, 547, L111

Collmar W., 2002, Mem. Soc. Astron. Ital., 73, 99

Condon J. J., Cotton W. D., Greisen E. W., Yin Q. F., Perley R. A., Taylor G. B., Broderick J. J., 1998, AJ, 115, 1693

Contigiani O., et al., 2017, MNRAS, 472, 636

Corbel S., Nowak M. A., Fender R. P., Tzioumis A. K., Markoff S., 2003, A&A, 400, 1007

Croston J. H., Hardcastle M. J., 2014, MNRAS, 438, 3310

Croton D. J., et al., 2006, MNRAS, 365, 11

Daly R. A., 2011, MNRAS, 414, 1253

Daly R. A., 2016, MNRAS, 458, L24

Daly R. A., Sprinkle T. B., O'Dea C. P., Kharb P., Baum S. A., 2012, MNRAS, 423, 2498

Daly R. A., Stout D. A., Mysliwiec J. N., 2016, preprint, (arXiv:1606.01399)

Driver S. P., et al., 2011, MNRAS, 413, 971

Dubois Y., Devriendt J., Slyz A., Teyssier R., 2012, MNRAS, 420, 2662

Eilek J. A., Melrose D. B., Walker M. A., 1997, ApJ, 483, 282

Ellison S. L., Patton D. R., Hickox R. C., 2015, MNRAS, 451, L35

Emerson J. P., Sutherland W. J., McPherson A. M., Craig S. C., Dalton G. B., Ward A. K., 2004, The Messenger, 117, 27

Fabian A. C., 1994, ARA&A, 32, 277

Fabian A. C., 2012, ARA&A, 50, 455

Falcke H., Biermann P. L., 1995, A&A, 293, 665

Falcke H., Körding E., Markoff S., 2004, A&A, 414, 895

Falle S. A. E. G., 1991, MNRAS, 250, 581

Fanaroff B. L., Riley J. M., 1974, MNRAS, 167, 31P

Farnes J. S., et al., 2018, MNRAS, 474, 3280

Felten J. E., Gould R. J., Stein W. A., Woolf N. J., 1966, ApJ, 146, 955

Feretti L., Dallacasa D., Giovannini G., Tagliani A., 1995, A&A, 302, 680

Ferrarese L., Merritt D., 2000, ApJ, 539, L9

Frank K., 2013, PhD thesis, Purdue University

Gallo E., Fender R. P., Pooley G. G., 2003, MNRAS, 344, 60

Gallo E., et al., 2014, MNRAS, 445, 290

Garrington S., Conway R. G., 1991, MNRAS, 250, 198

Garrington S., Leahy J. P., Conway R. G., Laing R. A., 1988, Nature Letters, 331, 147

Gaspari M., Brighenti F., Temi P., 2015, A&A, 579, A62

Gawroński M. P., Marecki A., Kunert-Bajraszewska M., Kus A. J., 2006, A&A, 447, 63

Gebhardt K., et al., 2000, ApJ, 539, L13

Gerke B. F., et al., 2005, ApJ, 625, 6

Godfrey L. E. H., Shabala S. S., 2013, ApJ, 767, 12

Godfrey L. E. H., et al., 2012, PASA, 29, 42

Gonçalves D. R., Friaça A. C. S., 1999, MNRAS, 309, 651

Gopal-Krishna Wiita P. J., 2000, A&A, 363, 507

Gültekin K., Cackett E. M., Miller J. M., Di Matteo T., Markoff S., Richstone D. O., 2009, ApJ, 706, 404

Gunn J. E., Gott III J. R., 1972, ApJ, 176, 1

Hales C., 2013, arXiv eprint,

Hardcastle M. J., 2013, MNRAS, 433, 3364

Hardcastle M. J., 2018, MNRAS, 475, 2768

Hardcastle M. J., Krause M. G. H., 2013, MNRAS, 430, 174

Hardcastle M. J., Krause M. G. H., 2014, MNRAS, 443, 1482

Hardcastle M. J., Alexander P., Pooley G. G., Riley J. M., 1998, MNRAS, 296, 445

Hardcastle M. J., Evans D. A., Croston J. H., 2007, MNRAS, 376, 1849

Häring N., Rix H.-W., 2004, ApJ, 604, L89

Harrison C. M., 2017, Nature Astron., 1, 165

Harrison C. M., Costa T., Tadhunter C. N., Flütsch A., Kakkad D., Perna M., Vietri G., 2018, Nature Astron., 2, 198

Heckman T. M., Best P. N., 2014, ARA&A, 52, 589

Heesen V., et al., 2018, MNRAS, 474, 5049

Heinz S., Sunyaev R. A., 2003, MNRAS, 343, L59

Hill G. J., Lilly S. J., 1991, ApJ, 367, 1

Hirotani K., 2005, ApJ, 619, 73

Hirotani K., Iguchi S., Kimura M., Wajima K., 2000, ApJ, 545, 100

Hocuk S., Barthel P. D., 2010, A&A, 523, A9

Huarte-Espinosa M., Krause M., Alexander P., 2011a, MNRAS, 417, 382

Huarte-Espinosa M., Krause M., Alexander P., 2011b, MNRAS, 418, 1621

Hurley-Walker N., et al., 2017, MNRAS, 464, 1146

Ineson J., Croston J. H., Hardcastle M. J., Mingo B., 2017, MNRAS, 467, 1586

Ishwara-Chandra C. H., Saikia D. J., 1999, MNRAS, 309, 100

Jenkins A., Frenk C. S., White S. D. M., Colberg J. M., Cole S., Evrard A. E., Couchman H. M. P., Yoshida N., 2001, MNRAS, 321, 372

Johnston-Hollitt M., Dehghan S., Pratley L., 2014, in Advancing Astrophysics with the Square Kilometre Array. PoS, doi:10.22323/1.215.0101, https://doi.org/10.22323/1.215.0101

Johnston S., et al., 2008, Exp Astron, 22, 151âĂŞ273

Jones M., 1995, ApJL&C, 32, 347

Jones T. W., Ryu D., Engel A., 1999, ApJ, 512, 105

Kaiser C. R., Alexander P., 1997, MNRAS, 286, 215

Kaiser C. R., Best P. N., 2007, MNRAS, 381, 1548

Kaiser C. R., Dennett-Thorpe J., Alexander P., 1997, MNRAS, 292, 723

Kapińska A. D., et al., 2017, AJ, 154, 253

Kardashev N. S., 1962, SovAstt, 6, 317

Kaviraj S., et al., 2012, MNRAS, 423, 49

Kaviraj S., et al., 2017, MNRAS, 467, 4739

Kimball A. E., Ivezić vZ., 2008, AJ, 136, 684

King I. R., 1972, ApJ, 174, L123

King A., 2003, ApJ, 596, L27

Komissarov S. S., 1994, MNRAS, 269, 394

Komissarov S. S., Falle S. A. E. G., 1998, MNRAS, 297, 1087

Körding E., Falcke H., Corbel S., 2006, A&A, 456, 439

Kormendy J., Ho L. C., 2013, ARA&A, 51, 511

Krause M., 2003, A&A, 398, 113

Krause M., 2005, A&A, 431, 45

Krause M., Alexander P., Riley J., Hopton D., 2012, MNRAS, 427, 3196

Kravchenko E. V., Kovalev Y. Y., Sokolovsky K. V., 2017, MNRAS, 467, 83

Kunert-Bajraszewska M., Gawroński M. P., Labiano A., Siemiginowska A., 2010, MNRAS, 408, 2261

Kuźmicz A., Jamrozy M., Bronarska K., Janda-Boczar K., Saikia D. J., 2018, ApJS, 238, 9

Laing R. A., 1988, Nature Letters, 331, 149

Laing R. A., Bridle A. H., 2014, MNRAS, 437, 3405

Laing R. A., Riley J. M., Longair M. S., 1983, MNRAS, 204, 151

Lakhchaura K., et al., 2018, Thermodynamic properties, multiphase gas and AGN feedback in a large sample of giant ellipticals

Lamastra A., Bianchi S., Matt G., Perola G. C., Barcons X., Carrera F. J., 2009, A&A, 504, 73

Lang D., Hogg D. W., Schlegel D. J., 2016, AJ, 151, 12

Liske J., et al., 2015, MNRAS, 452, 2087

Lobanov A. P., 1998, A&A, 330, 79

Longair M. S., Ryle M., Scheuer P. A. G., 1973, MNRAS, 164, 243

Lonsdale C. J., et al., 2003, PASP, 115, 897

Lovelace R. V. E., 1976, Nature, 262, 649

Lukic V., Brüggen M., Banfield J. K., Wong O. I., Rudnick L., Norris R. P., Simmons B., 2018, MNRAS, 476, 246

Manolakou K., Kirk J. G., 2002, A&A, 391, 127

Mao S. A., et al., 2014, arXiv eprint,

Marinoni C., 2010, Tessellations in the Sciences; Virtues, Techniques and Applications of Geometric Tilings. Springer Verlag

Marinoni C., Davis M., Newman J. A., Coil A. L., 2002, ApJ, 580, 122

Markoff S., 2010, in Belloni T., ed., Lecture Notes in Physics, Berlin Springer Verlag Vol. 794, Lecture Notes in Physics, Berlin Springer Verlag. p. 143 (arXiv:0909.2574), doi:10.1007/978-3-540-76937-8_6

Martín-Navarro I., Mezcua M., 2018, ApJL, 855, L20

Massaglia S., Bodo G., Rossi P., Capetti S., Mignone A., 2016, A&A, 596, A12

Mathews W. G., Brighenti F., 2003, ARA&A, 41, 191

Mathiesen B. F., Evrard A. E., 2001, ApJ, 546, 100

McConnell N. J., Ma C.-P., 2013, ApJ, 764, 184

McHardy I. M., Stewart G. C., Edge A. C., Cooke B., Yamashita K., Hatsukade I., 1990, MNRAS, 242, 215

McNamara B. R., Nulsen P. E. J., 2007, ARA&A, 45, 117

Mehta K. T., Georganopoulos M., Perlman E. S., Padgett C. A., Chartas G., 2009, ApJ, 690, 1706

Meier D. L., 2001, ApJl, 548, L9

Merloni A., Heinz S., di Matteo T., 2003, MNRAS, 345, 1057

Middelberg E., et al., 2008, AJ, 135, 1276

Miraghaei H., Best P. N., 2017, MNRAS, 466, 4346

Mittal R., Hudson D. S., Reiprich T. H., Clarke T., 2009, A&A, 501, 835

Murgia M., 2003, PASA, 20, 19

Murgia M., Govoni F., Feretti L., Giovannini G., Dallacasa D., Fanti R., Taylor G. B., Dolag K., 2004, A&A, 424, 429

Nakwacki M. S., Kowal G., Santos-Lima R., de Gouveia Dal Pino E. M., Falceta-Golçalves D. A., 2016, MNRAS, 455, 3702

Narayan R., Yi I., 1995, ApJ, 452, 710

Nisbet D. M., Best P. N., 2016, MNRAS, 455, 2551

Norris R. P., et al., 2006, AJ, 132, 2409

Norris R. P., et al., 2011, PASA, 28, 215

Norris R. P., Lenc E., Roy A. L., Spoon H., 2012, MNRAS, 422, 1453

Norris R. P., et al., 2013, PASA, 30, e020

Nyland K., et al., 2018, ApJ, 859, 23

O'Sullivan S. P., Lenc E., Anderson C. S., Gaensler B. M., Murphy T., 2018, MNRAS, 475, 4263

Oppermann N., et al., 2015, A&A, 575, A118

Owen F. N., Ledlow M. J., 1994, in Bicknell G. V., Dopita M. A., Quinn P. J., eds, Astronomical Society of the Pacific Conference Series Vol. 54, The Physics of Active Galaxies. p. 319

Pasetto A., Carrasco-González C., O'Sullivan S., Basu A., Bruni G., Kraus A., Curiel S., Mack K.-H., 2018, Galaxies, 6, 40

Pellegrini S., Ciotti L., Negri A., Ostriker J. P., 2018, ApJ, 856, 115

Perucho M., Martí J. M., Laing R. A., Hardee P. E., 2014, MNRAS, 441, 1488

Pilbratt G. L., et al., 2010, A&A, 518, 6

Planck Collaboration et al., 2014, A&A, 571, A16

Pope E. C. D., Mendel J. T., Shabala S. S., 2012, MNRAS, 419, 50

Pshirkov M. S., Tinyakov P. G., Kronberg P. P., Newton-McGee K. J., 2017, ApJ, 738, 192

Punsly B., 2005, ApJl, 623, L9

Punsly B., Coroniti F. V., 1990, ApJ, 354, 583

Raouf M., Shabala S. S., Croton D. J., Khosroshahi H. G., Bernyk M., 2017, MNRAS, 471, 658

Rasia E., et al., 2006, MNRAS, 369, 2013

Rawlings S., Jarvis M. J., 2004, MNRAS, 355, L9

Rawlings S., Abdalla F. B., Bridle S. L., Blake C. A., Baugh C. M., Greenhill L. J., van der Hulst J. M.,
2004, New Astronomy Reviews, 48, 1013

Rephaeli Y., 1995, ARA&A, 33, 541

Riess A. G., et al., 2018, ApJ accepted

Robotham A. S. G., Obreschkow D., 2015, PASA, 32, e033

Robotham A. S. G., et al., 2011, MNRAS, 416, 2640

Rood H. J., Page T. L., Kintner E. C., King I. R., 1972, ApJ, 175, 627

Rubin D., Loeb A., 2013, JCAP, 12, 019

Russell H. R., Fabian A. C., McNamara B. R., Broderick A. E., 2015, MNRAS, 451, 588

Rybiki G. B., Lightman A. P., 1979, Radiative Processes in Astrophysics. Vol. 1, Wiley-VCH

Sabater J., Best P. N., Argudo-Fernández M., 2013, MNRAS, 430, 638

Sadler E. M., Jenkins C. R., Kotanyi C. G., 1989, MNRAS, 240, 591

Sadler E. M., Ekers R. D., Mahony E. K., Mauch T., Murphy T., 2014, MNRAS, 438, 796

Saikia P., Körding E., Falcke H., 2015, MNRAS, 450, 2317

Sarazin C. L., 1988, X-ray Emission from Clusters of Galaxies. Vol. 1, Press Syndicate of the University
of Cambridge

Saripalli L., Hunstead R. W., Subrahmanyan R., Boyce E., 2005, AJ, 130, 896

Sbarrato T., Padovani P., Ghisellini G., 2014, MNRAS, 445, 81

Scheuer P. A. G., 1974, MNRAS, 166, 513

Scheuer P. A. G., Readhead A. C. S., 1979, Nature, 277, 182

Shabala S. S., 2018, MNRAS, 478, 5074

Shabala S., Alexander P., 2009, ApJ, 699, 525

Shabala S. S., Godfrey L. E. H., 2013, ApJ, 769, 129

Shabala S. S., Ash S., Alexander P., Riley J. M., 2008, MNRAS, 388, 625

Shabala S. S., Kaviraj S., Silk J., 2011, MNRAS, 413, 2815

Shabala S. S., Santoso J. S., Godfrey L. E. H., 2012, ApJ, 756, 161

Shabala S. S., Deller A., Kaviraj S., Middelberg E., Turner R. J., Ting Y. S., Allison J. R., Davis T. A., 2017, MNRAS, 464, 4706

Shakura N. I., Sunyaev R. A., 1973, A&A, 24, 337

Shimwell T. W., et al., 2016, MNRAS, 459, 277

Silk J., Rees M. J., 1998, A&A, 331, L1

Singh V., Ishwara-Chandra C. H., Wadadekar Y., Beelen A., Kharb P., 2015, MNRAS, 446, 599

Sokolovsky K. V., Kovalev Y. Y., Pushkarev A. B., Lobanov A. P., 2011, A&A, 532, A38

Sotomayor-Beltran C., et al., 2013, A&A, 552, A58

Spacek A., Richardson M., Scannapieco E., 2017, arXiv eprint

Stanek R., Evrard A. E., Böhringer H., Schuecker P., Nord B., 2006, ApJ, 648, 956

Sunyaev R. A., Zel'dovich Y. B., 1972, CASP, 4, 173

Tadhunter C., 2016, Astron. Astrophys. Rev., 24, 10

Tadhunter C., Dicken D., Morganti R., Konyves V., Ysard N., Nesvadba N., Ramos Almeida C., 2014, MNRAS, 445, L51

Tetarenko A. J., et al., 2016, MNRAS, 460, 345

Tingay S. J., et al., 2013, PASA, 30, 21

Tremaine S., et al., 2002, ApJ, 574, 740

Tribble P. C., 1991, MNRAS, 253, 147T

Turner R. J., 2018, MNRAS, 476, 2522

Turner R., 2019, Submitted

Turner R. J., Shabala S. S., 2015, ApJ, 806, 59

Turner R. J., Rogers J. G., Shabala S. S., Krause M. G. H., 2018a, MNRAS, 473, 4179

Turner R. J., Shabala S. S., Krause M. G. H., 2018b, MNRAS, 474, 3361

Urry C. M., Padovani P., 1995, PASP, 107, 803

Vacca V., et al., 2016, A&A, 591, A13

Vikhlinin A., Markevitch M., Murray S. S., 2001a, ApJ, 549, L47

Vikhlinin A., Markevitch M., Forman W., Jones C., 2001b, ApJ, 555, L87

Vikhlinin A., Kravtsov A., Forman W., Jones C., Markevitch M., Murray S. S., Van Speybroeck L., 2006, ApJ, 640, 691

Wagner A. Y., Bicknell G. V., Umemura M., 2012, ApJ, 757, 136

Wagner A. Y., Bicknell G. V., Umemura M., Sutherland R. S., Silk J., 2016, Astron. Nachr., 337, 167

Wang Y., Kaiser C. R., Laing R., Alexander P., Pavlovski G., Knigge C., 2009, MNRAS, 397, 1113

Wayth R. B., et al., 2015, PASA, 32, e025

Weston S. D., Seymour N., Gulyaev S., Norris R. P., Banfield J., Vaccari M., Hopkins A. M., Franzen T. M. O., 2018, MNRAS, 473, 4523

White M., 2001, A&A, 367, 27

Whittam I. H., Jarvis M. J., Green D. A., Heywood I., Riley J. M., 2017, MNRAS, 471, 908

Willott C. J., Rawlings S., Blundell K. M., Lacy M., 1999, MNRAS, 309, 1017

Wong O. I., 2018, In preparation

Wright E. L., 2011, in American Astronomical Society Meeting Abstracts #217. p. 301.01

Wright E. L., et al., 2010, AJ, 140, 1868

Wu C., et al. 2018, Submitted to MNRAS

Yang X., Mo H. J., van den Bosch F. C., Pasquali A., Li C., Barden M., 2007, ApJ, 671, 153

Yang X., Mo H. J., van den Bosch F. C., 2008, ApJ, 676, 248

Yates P., et al. 2018, Submitted to MNRAS

van Haarlem M. P., et al., 2013, A&A, 556, A2